



저작자표시-비영리-변경금지 2.0 대한민국

이용자는 아래의 조건을 따르는 경우에 한하여 자유롭게

- 이 저작물을 복제, 배포, 전송, 전시, 공연 및 방송할 수 있습니다.

다음과 같은 조건을 따라야 합니다:



저작자표시. 귀하는 원저작자를 표시하여야 합니다.



비영리. 귀하는 이 저작물을 영리 목적으로 이용할 수 없습니다.



변경금지. 귀하는 이 저작물을 개작, 변형 또는 가공할 수 없습니다.

- 귀하는, 이 저작물의 재이용이나 배포의 경우, 이 저작물에 적용된 이용허락조건을 명확하게 나타내어야 합니다.
- 저작권자로부터 별도의 허가를 받으면 이러한 조건들은 적용되지 않습니다.

저작권법에 따른 이용자의 권리는 위의 내용에 의하여 영향을 받지 않습니다.

이것은 [이용허락규약\(Legal Code\)](#)을 이해하기 쉽게 요약한 것입니다.

[Disclaimer](#)

공학박사 학위논문

**Numerical Studies on the Smelting
Furnace in Mitsubishi Process for Cu
Refining**

미쯔비시 동 제련 공법 중 제련 로에 대한
수치 해석 연구

2016년 2월

서울대학교 대학원
재료공학부
박종하

Abstract

Numerical Studies on the Smelting Furnace in Mitsubishi Process for Cu Refining

Park Jong-ha

Department of Materials Science and Engineering

The Graduate School

Seoul National University

The Smelting furnace (S-furnace) used for Cu concentrate refining in the Mitsubishi process, a type of Cu refining method, undergoes violent internal reactions and temperatures in excess of 1300°C, method, making a direct experimental approach difficult.

A major issue in current processing conditions is the irregular fracture of lances used to inject Cu concentrate and saturated oxygen. Costs are rising for the replacement of high-priced, high chrome-content steel used for the lances, and interruption of processing to adjust the height of the irregularly fractured lances results in significant processing loss.

In the present study, we present a way to identify transport phenomena and reaction heat within the S-furnace, the movement of particles and the cause of lance fracture through

the development of a comprehensive 3-D numerical analysis model using ANSYS FLUENT. Flow phenomena in the S-furnace is dependent mainly on gas and particle injection conditions. Melt velocities increase when gas and particles are injected together, especially below the lance. Splashing of large amounts of matte and slag due to high injection rates can have detrimental effects on the lances and furnace interior.

Presently, the lance tip temperature increases when only gas is injected during processing, and decreases when gas and Cu concentrate are injected simultaneously. The temperature increase is caused by reaction heat and radiation, while the decrease is caused by the absorption of heat by the Cu concentrate, as found in the calculations. FFT analysis revealed that splashed matte and slag results in lance temperature changes. The inner-outer and upper-lower temperature discrepancies and overall temperature changes imposed on the lances can result in thermal stress and fatigue. Stress analysis revealed that most of the lances undergo stress greater than the yield strength.

The microstructure of before-using lance and fractured lance were analyzed by SEM, EDS, EBSD and AES. The lance is a high-Cr and a duplex stainless steel. But it was confirmed that Cr depleted at the lance surface, while substances composed of S, Si and O penetrated the grain boundaries. This leads us to believe that Cr depletion and penetration of S, Si and O into the grain boundaries weakens the lance surface, while low cycle thermal fatigue and external factors such as splashed melt during processing leads to quicker crack propagation and eventual fracture.

Raising the lance tip can reduce lance fracture, but raises the concern of less melt mixing. Therefore, setting the lance tip height and flow velocities for the present processing

conditions as a standard, we compared and analyzed numerical experiment results for a variety of different conditions. Results show that lower lance tip height and higher lance tip flow velocities result in less stable flow phenomena within the furnace. We also confirmed that even when the lance tip is raised, and increased flow velocity can maintain an equivalent degree of melt mixing, while stabilizing flow phenomena. In particular, it was found that raising the lance tip lowers its temperature and thermal stress, so that optimized conditions improve stability and prevent lance fracture.

Through the present study, we were able to develop a comprehensive 3-D numerical model within the S-furnace which are not easily accessible by direct experimentation. We were able to recreate lance temperature changes through calculations taking into account heat and confirmed the thermal stresses under the lance. Through microstructure analysis of lance, we predicted the mechanism by which lance fracture occurs, and confirmed that raising the lance tip can result in stable conditions for the furnace interior and lance stability.

Keywords: Mitsubishi continuous process, Smelting furnace, Copper refining, Numerical analysis, ANSYS FLUENT, Lance fracture

Student number: 2012-30159

Contents

Abstract.....	I
Contents	IV
List of Figures.....	VIII
List of Tables.....	XIV
Chapter 1. Introduction.....	1
1. 1. Mitsubishi continuous process	1
1. 2. Smelting furnace	4
1. 3. Problems in smelting furnace.....	11
1. 3. 1. Hearth wearing	11
1. 3. 2. Splashed matte and slag in uptake outlet	11
1. 3. 3. Lance fracture.....	12
1. 4. Previous studies for the Mitsubishi process	14
1. 5. Goals of the research.....	19
Chapter 2. Numerical modeling	21
2. 1. Global modeling of smelting furnace.....	21
2. 2 Simulation model	23
2. 2. 1. Flow	23
2. 2. 2. Turbulence Model	24

2. 2. 3. Volume of Fluid (VOF)	26
2. 2. 4. Discrete Phase Model (DPM)	26
2. 2. 5. Heat Transfer	28
2. 2. 6. Radiation	29
2. 3 Initial & Boundary Condition	31
2. 4 Physical properties used in numerical model	33
Chapter 3. Fluid flow in the smelting furnace.....	35
3. 1. Calculation conditions.....	35
3. 1. 1 Injection condition & heat zone	35
3. 1. 2 Measurement location	37
3. 1. 3 The calculation initial stage.....	40
3. 2. Result and discussion	42
3. 2. 1. Fluid distribution	42
3. 3. 2. Phase change	46
3. 3. 3. Temperature distribution	50
3. 3 Summary	54
Chapter 4. Temperature behavior in the lance.....	55
4. 1. Calculation conditions.....	55
4. 1. 1 Lance fracture phenomenon	55
4. 1. 2 Experimental measurement	57
4. 2. Result and discussion	59

4. 2. 1. Temperature change	59
4. 2. 2. Temperature fluctuations behavior.....	69
4. 2. 3. Thermal stress of the lance.....	77
4. 3. Summary	83
Chapter 5. Lance fracture surface analysis	84
5. 1. Introduction.....	84
5. 2. Experimental method	93
5. 3. Result and discussion	97
5.3.1 Analysis of the before-using lance	97
5.3.2 Analysis of the fractured lance.....	104
5. 4. Summary	124
Chapter 6. Optimization of lance tip height & velocity.....	126
6. 1. Introduction.....	126
6. 2. Calculation conditions.....	127
6. 3. Results and discussion.....	132
6. 3. 1. Comparison of flow change according to lance tip height and velocity	132
6. 2. 2. Comparison of matte mixing according to lance tip height and velocity	142
6. 2. 3. Changes of other factors according to lance tip height and velocity...	148
6. 3. Additional test result and discussion	156

6. 4. Summary	163
Chapter 7. Conclusions.....	164
References.....	167
초 록.....	177

List of Figures

Fig. 1- 1 Global copper production share [2].....	2
Fig. 1- 2 Mitsubishi process flow sheet and vertical layout at Gresik, Indonesia (Ajima <i>et al.</i> , 1999) [3].....	2
Fig. 1- 3 Mitsubishi process flow sheet [2].....	3
Fig. 1- 4 Details of Mitsubishi smelting furnace [3].....	5
Fig. 1- 5 Simplified partial phase diagram for the Fe-O-S-SiO ₂ system showing liquid-liquid (slag-matte) immiscibility caused by SiO ₂ (Yazawa and Kameda, 1953) [3].....	8
Fig. 1- 6 Cu ₂ S-FeS(matte) phase diagram [3].....	9
Fig. 1- 7 Liquidus surface in the FeO-Fe ₂ O ₃ -SiO ₂ system at 1200°C and 1250°C (Muan, 1955) [3].....	9
Fig. 1- 8 Fractured lances after actual processing [3].....	13
Fig. 1- 9 Experiment paper of 1-lance system about Mitsubishi smelting furnace written by researcher of LS-Nikko Copper. [23].....	15
Fig. 1- 10 Experiment paper of 1-lance system about Mitsubishi smelting furnace written by researcher of LS-Nikko Copper [23, 24].....	16
Fig. 1- 11 (a) Temperature of gas phase at 1200K (b) SO ₂ content in flash smelting [25].	18
Fig. 2- 1 Grid configuration of smelting furnace.	22

Fig. 3- 1 Gas and particle injection conditions in calculation.....	36
Fig. 3- 2 Heat zone region below lance. (Red area).....	36
Fig. 3- 3 A: Vertical cross-section at center of uptake outlet, B: vertical cross-section of through 6 lances.	38
Fig. 3- 4 Lance temperature measurement regions.	39
Fig. 3- 5 (a) Change of melt velocities at the six points from static initial state.....	41
Fig. 3- 6 Velocity vector distributions with different injection conditions at the plane A and B.	43
Fig. 3- 7 Change of gas average velocity. (Calculation result)	44
Fig. 3- 8 Change of melt average velocity. (Calculation result)	45
Fig. 3- 9 Distribution of matte and slag volume fraction with different injection conditions at the plane A and B.....	48
Fig. 3- 10 Average melt volume fraction variation of the gas region from 0 to 60 seconds. (Calculation result).....	49
Fig. 3- 11 Temperature distribution with different injection conditions around the lances.	51
Fig. 3- 12 Distribution of temperature different injection conditions at the plane A and B.	53
Fig. 4- 1 Process of lance wearing.	56
Fig. 4- 2 Thermocouple location in the processing.....	58
Fig. 4- 3 Temperature variation of the lance. (In processing)	59
Fig. 4- 4 Temperature profile in processing.....	61

Fig. 4- 5 Temperature variation of the lance from 0 to 30 seconds.....	62
Fig. 4- 6 Temperature variation of the lance from 0 to 30 seconds.....	65
Fig. 4- 7 Temperature variation of the lance from 0 to 30 seconds.....	66
Fig. 4- 8 Temperature variation of the lance from 0 to 30 seconds.....	67
Fig. 4- 9 Temperature variation of the lance from 0 to 30 seconds.....	68
Fig. 4- 10 FFT analysis result of calculation and experimental results at stage 1.	69
Fig. 4- 11 Temperature fluctuation comparison at inner surface, body and outer surface of the lance. (Calculation result)	71
Fig. 4- 12 (a) Matte and slag volume fraction variation 0.1m distance away from the outer surface of the lance. (Calculation result).....	74
Fig. 4- 13 Temperature difference between outer wall of the lance and inner point of the lance from 0 to 30 seconds.....	76
Fig. 4- 14 Lance temperature distribution. (a) Outside, stage 1 (gas injection), (b) Outside, stage 2 (gas and particle injection), (c) Central, stage 1 (gas injection), (d) Central, stage 2 (gas and particle injection).....	78
Fig. 4- 15 Lance normal stress. (MPa).....	79
Fig. 4- 16 Stress direction of the lance.	80
Fig. 4- 17 Comparison of calculated equivalent stress and literature yield strength (MPa) [49].....	81
Fig. 4- 18 Schematic diagram of temperature and yield strength by lance region.....	82
Fig. 5- 1 Oxidation resistance of several stainless steels as a function of temperature [57].	85

Fig. 5- 2 Cyclic oxidation resistance of several ferritic and austenitic stainless steels in still air at (a) 1000°C and (b) 1200°C for up to 400 cycles (30 min. in furnace and 30 min. out of furnace) [58].	86
Fig. 5- 3 (a) Section of a cast HH(25%Cr, 12%Ni) STS (b) Sigma phase (dark) precipitated from excessive ferrite in the cast HH STS [62].	88
Fig. 5- 4 Sigma-phase embrittlement [63].	88
Fig. 5- 5 Iron-Chromium phase diagram [63].	89
Fig. 5- 6 Lance fracture surface.	94
Fig. 5- 7 Electron Beam – Sample interaction.	95
Fig. 5- 8 (a) Sampling area for SEM & AES analysis.	96
Fig. 5- 9 EBSD analysis results of the before-using lance.	99
Fig. 5- 10 (a) SEM image of before-using lance. (b) Images of EDS quantitative mapping. (Before-using lance).	101
Fig. 5- 11 Range of mean thermal expansion coefficient from room temperature to T of austenitic stainless steels, FCC nonmagnetic Ni-base alloys, ferritic and martensitic iron and steels, and FCC ferromagnetic Fe-Ni and Fe-Ni-Co alloys.	103
Fig. 5- 12 Results of EBSD analysis.	106
Fig. 5- 13 SEM image near the exterior surface.	107
Fig. 5- 14 Images of EDS mapping. (O, N, S, P, Fe, Cr, Mn, Ni, Cu, Si).	109
Fig. 5- 15 Quantitative mapping results.	112
Fig. 5- 16 SEM image near the interior surface.	113
Fig. 5- 17 EDS quantitative mapping results.	117

Fig. 5- 18 Cr peaks at the grain boundary in the lance body.....	120
Fig. 5- 19 S peaks with Cr and Mn at the grain boundary in the lance body.	122
Fig. 6- 1 Three lance tip heights.	128
Fig. 6- 2 Gas and particle injection condition at the lance.....	129
Fig. 6- 3 Flow change measuring regions.	130
Fig. 6- 4 Outlet matte volume fraction measuring regions.	131
Fig. 6- 5 Lance tip matte volume fraction and lance temperature difference between inner & outer surface measuring points.	131
Fig. 6- 6 Velocity at the vertical plane at 40 seconds according to lance tip height and velocity.....	134
Fig. 6- 7 Matte volume fraction at the vertical plane at 40 seconds according to lance tip height and velocity.	136
Fig. 6- 8 Particle mass concentration at the vertical plane at 40 seconds according to lance tip height and velocity.	138
Fig. 6- 9 Single particle stream at 40 seconds according to lance tip height and velocity.	141
Fig. 6- 10 Matte average velocity change according to lance tip height and velocity. ...	143
Fig. 6- 11 Matte average velocity according to lance tip height and velocity.....	144
Fig. 6- 12 Matte average velocity according to lance tip height and velocity.....	145
Fig. 6- 13 Matte average turbulence kinetic energy according to lance tip height and velocity.....	146
Fig. 6- 14 Matte average turbulence kinetic energy according to lance tip height and	

velocity.....	147
Fig. 6- 15 Uptake outlet's (2.6m from the initial bath surface) matte average volume fraction according to lance tip height and velocity.	149
Fig. 6- 16 Uptake outlet's (2.6m from the initial bath surface) matte average volume fraction according to lance tip height and velocity.	150
Fig. 6- 17 Maximum depth of cavity (below the initial bath surface) according to lance tip height and velocity.	151
Fig. 6- 18 Lance tip matte volume fraction according to lance tip height and velocity. .	153
Fig. 6- 19 Lance tip matte volume fraction according to lance tip height and velocity. .	154
Fig. 6- 20 Lance tip temperature difference between inner and outer surface according to lance tip height and velocity.....	155
Fig. 6- 21 Lance temperature variations from 0 to 45 seconds.	157
Fig. 6- 22 Lance temperature distribution. (Gas injection, 30s)	159
Fig. 6- 23 Comparison of calculated equivalent stress and literature yield strength (MPa). Up: 1500mm / Low: 700mm.....	161
Fig. 6- 24 Equivalent stress of copper lance (MPa).....	162

List of Tables

Table 1- 1 Compositions of industrial concentrates, fluxes, mattes, slags and dusts for various matte-smelting process, 2001 [3].	7
Table 2- 1 Boundary conditions of gas and particles [47, 48].	32
Table 2- 2 Composition of A297HC [49].	33
Table 2- 3 Physical properties of lance [49].	34
Table 2- 4 Physical properties of matte and gas [3, 47].	34
Table 4- 1 Comparison of the temperature variation of the lance between the experiment and calculation.	63
Table 6- 1 Lance tip velocities.....	129

Chapter 1. Introduction

1. 1. Mitsubishi continuous process

The Mitsubishi continuous process is a method of refining copper from copper ores, consisting of three furnaces: the smelting furnace for making matte (S-furnace), the electric slag cleaning furnace for separating matte and slag (CL-furnace) and the converting furnace for producing copper crude metal (C-furnace). The furnaces are connected by launders, and the melt is continuously transferred from one furnace to the next by gravity. As a continuous smelting process of refining copper, it has many merits such as good throughput per area, high copper refining rate because of low copper loss from the slag and low emissions. In addition, the inevitable SO₂ capture can be carried out effectively, with the captured SO₂ being used for liquid SO₂ production. All of them make the Mitsubishi process an effective and efficient method [1].

The Mitsubishi process is being implemented in Naoshima in Japan, Timmins in Canada, Dahej in India and Onsan in South Korea. And the share of copper production for Mitsubishi process accounts for about 8.4%, as shown in Fig. 1-1 [2]. The Fig. 1-2 shows the overall process of the Mitsubishi process and Fig. 1-3 shows the Mitsubishi process flow sheet. The 99.99% purity of Cu is obtained at the last stage [3].

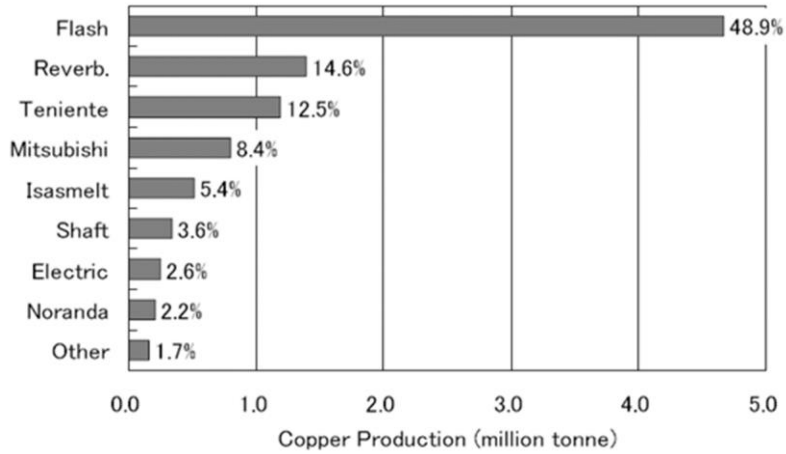


Fig. 1- 1 Global copper production share [2].

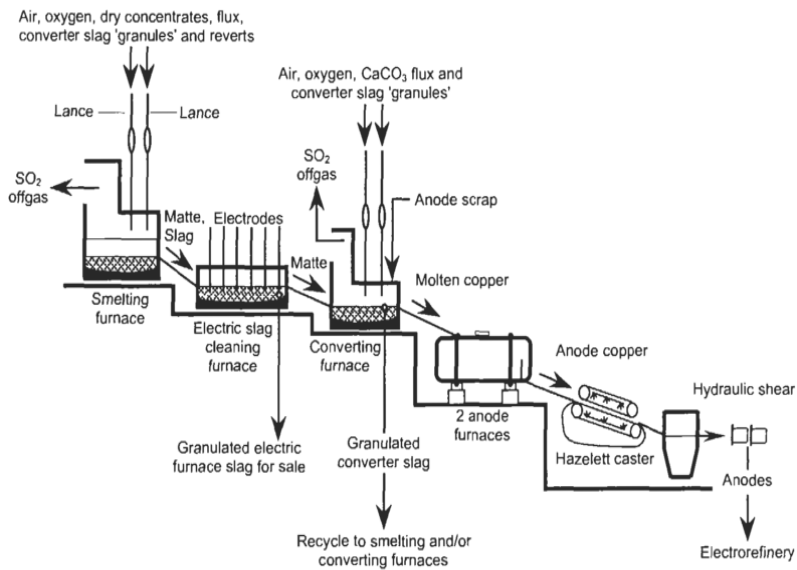


Fig. 1- 2 Mitsubishi process flow sheet and vertical layout at Gresik, Indonesia (Ajima *et al.*, 1999) [3].

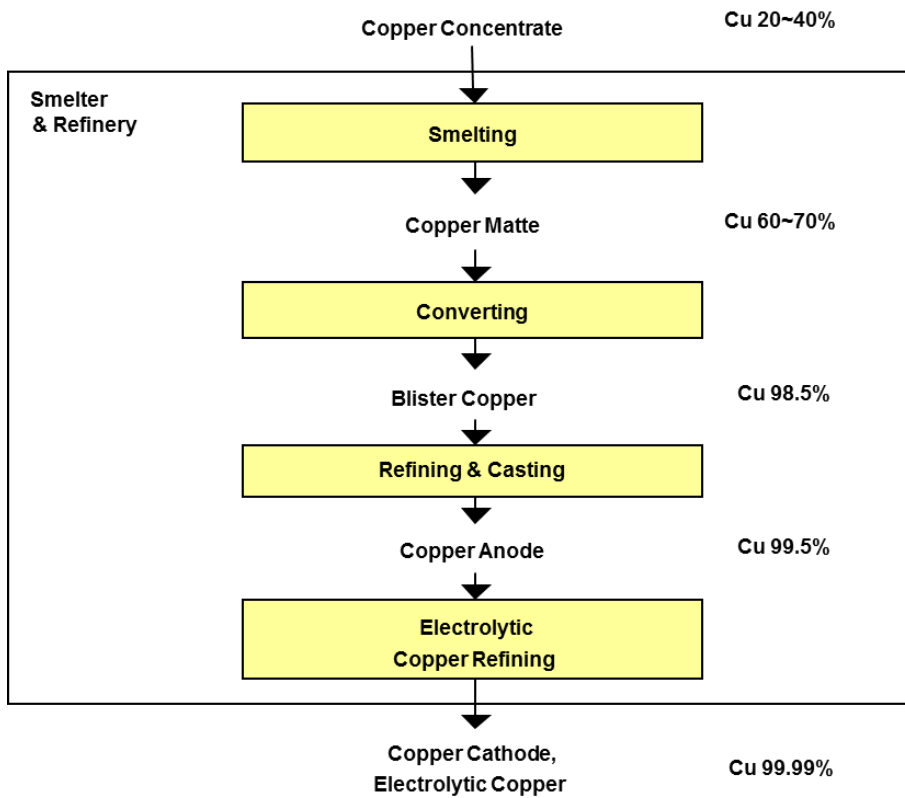


Fig. 1- 3 Mitsubishi process flow sheet [2].

1. 2. Smelting furnace

The Fig. 1-4 shows the smelting furnace of Mitsubishi continuous process [3]. In the smelting furnace, dried concentrates, fluxes and recycled materials are injected with oxygen enriched air into molten bath through vertical lances. In the Mitsubishi process, the nozzle is represented by the lance and copper ore is represented by copper concentrate. The copper concentrates are smelted instantly and produce high grade matte of around 68% copper and Fe-silicate slag [4]. The matte grade usually reaches a level between 65% and 72%, according to the grade of the available copper concentrates. A typical slag contains 0.6 wt.% Cu, 34 wt.% SiO₂ and 6 wt.% CaO [1].

In the smelting furnace, the molten bath is primarily matte with a thin layer of slag on top. The feed materials (copper concentrate, flux, etc.) are injected into the matte with high percentage of oxygen gas via vertical lances at velocities of around 100~200m/s. The lances are made of high-Cr stainless steel without water cooling. Because the distance between lance tip and matte is kept around 700mm, there is no time for the feed materials to be combusted before they reach to the matte. The feed materials quickly melted by the effective heat transfer in the turbulent area of the melt. Oxygen reacts with the iron sulfide in the matte and the oxidized iron combines with flux to form slag [5]. The major smelting reactions are represented by [6]

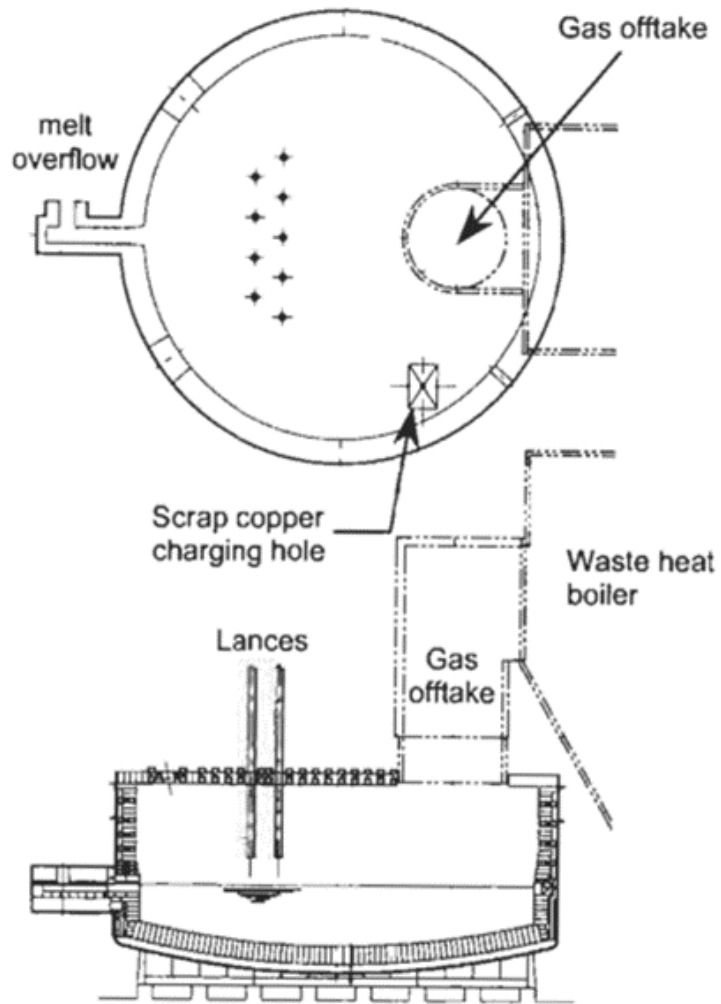
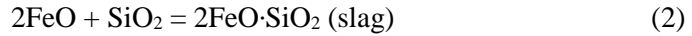
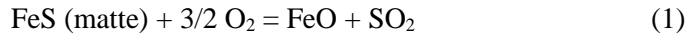


Fig. 1- 4 Details of Mitsubishi smelting furnace [3].



The difference between bath smelting and flash smelting is that all the reactions occur in the bath at a constant oxygen partial pressure. As a result, it is possible to obtain an excellent matte composition. In the flash smelting, the feed materials are melted and oxidized above the bath, leading to the excess magnetite in the furnace causing by some oxidized iron [7].

The slag includes FeO from Fe oxidation, SiO₂ from flux and oxide impurities from copper concentrate. There are usually oxides found in slags including FeO, Fe₂O₃, SiO₂, Al₂O₃, CaO and MgO [3]. As Fig. 1-5 shows, immiscibility of matte and slag increases with increasing silica content. The typical industrial matte contains only about one percent of oxygen, which is shown in the Table 1-1. The matte's specific gravity is higher than that of slag and so it forms the bottom layer in the furnace. As Fig. 1-6 shows, matte's melting points are lower than 1200°C, which is the melting point of most slags in Fig. 1-7. The matte viscosity is lower as well ~0.003 kg/ms and typical slag viscosity is about 0.2 to 1 kg/m·s. Thus, smelting furnace are operated at about 1250°C, to ensure a molten slag and overheated matte. In the processing,

the matte and slag stay molten state during tapping and transfer. The surface tension of Cu₂S-FeS mattes ranges from 0.33-0.45 N/m. Specific gravity ranges linearly from 3.9 for pure FeS to 5.2 for pure Cu₂S. Interfacial tension increases from near zero in low copper matte to about 0.3 N/m for high copper matte. (~70 mass% Cu₂S) [8] Matte specific electrical conductance is from 200 to 1000 ohm-1cm-1 [3].

Table 1- 1 Compositions of industrial concentrates, fluxes, mattes, slags and dusts for various matte-smelting process, 2001 [3].

Smelter & process	Concentrate					Flux			Matte			Slag						Dust						
	Cu	Fe	S	SiO ₂	other	SiO ₂	Al ₂ O ₃	other	Cu	Fe	S	O	Cu	SiO ₂	total Fe	Fe ₂ O ₃	S	Al ₂ O ₃	other	Cu	Fe	S	SiO ₂	other
Carais Outokumpu flash	32	23	28	9	Al ₂ O ₃ 2 CaO 1 MgO 1	98		2	62	12	22		1.8	31	42	16	0.5		MgO 2	29			7	Al ₂ O ₃ 2 CaO 1
Norddeutsche Outokumpu flash	33	24	31	5	Al ₂ O ₃ 2 CaO 1 Zn 1	85-95	5	CaO 2	65	12	22	1	1.5	32	39	5	0.6	4	CaO 3 MgO 1	26	15	12	3	Al ₂ O ₃ 2 CaO 1
Toyo Outokumpu flash	32	25	30	6		73	10	Fe ₂ O ₃ 4	63	10	22		1.3	33	37	13	0.6	5	CaO 1 MgO 2	20	15	9	7	
Chino Inco flash	29	25	32	7	Al ₂ O ₃ 1	90	4	Fe 2 Cu 2	59	16	23	Fe ₂ O ₃ 4	0.8	34	43	4	1	3		30	17	12	7	CaO 2
Calsones Teniente	32	25	30	6	Al ₂ O ₃ 2 CaO 1 other 4	95	2	3	74	4	20	other 1	6	27	38	16	2.7	4	CaO 1 other 3	34	6	11	4	Al ₂ O ₃ 1
Port Kembla Noranda	31	28	31	5	Al ₂ O ₃ 1 CaO 1 MgO 1	96			72	6	20		2	30	46	15	0.8	2	CaO 3	34	23	23	7	Al ₂ O ₃ 2
Sterlitc, India Isasmelt	30	28	31	9	CaO 2	85	1	4	63	13			0.7	29	44	3	0.7	4.9	CaO 3	33	32		10	
Olympic Dam OK flash direct-to-copper	41	16	25	3	Al ₂ O ₃ 1	95	1	Fe ₂ O ₃ 2	99	0.8	0.4		20	15	30		0.1	3	CaO 0.1	36	14		3	SO ₂ 30
Gresik Mitsubishi	56	23	30			90	3	1	68	8	22		0.7	33	39	2	0.5	5	CaO 6	63	9	19	1	
Osan Mitsubishi	32	23	29	8	Al ₂ O ₃ 2 CaO 0.4	82	4	Fe 5	69	8	22		0.9	34	38	3	0.4	5	CaO 5	17	5	9	1	0.3
Onahams Reverberatory	33	23	28	7	Al ₂ O ₃ 2 CaO 1 MgO 0.4	88	4	Fe 1.3 CaO 0.7	44	26	26		0.7	32	37	3	1	5	CaO 4	13	13	5	24	CaO 3

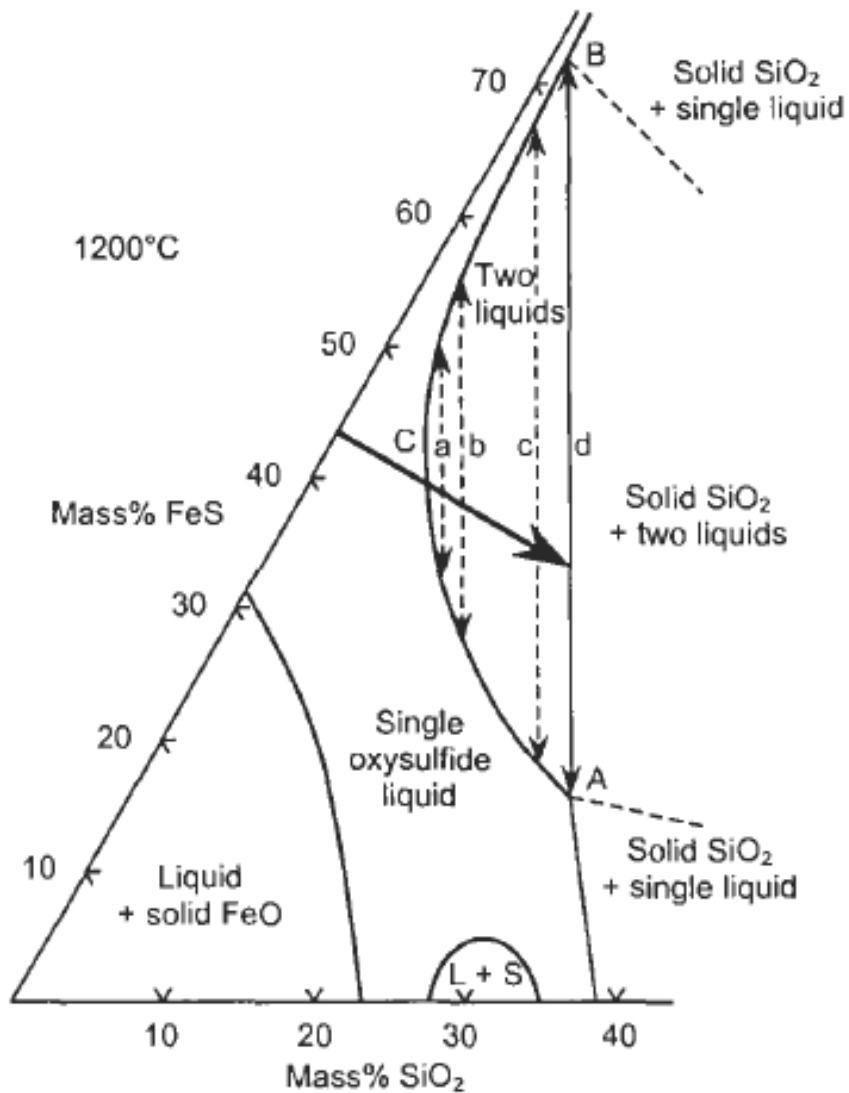


Fig. 1- 5 Simplified partial phase diagram for the Fe-O-S-SiO₂ system showing liquid-liquid (slag-matte) immiscibility caused by SiO₂ (Yazawa and Kameda, 1953) [3].

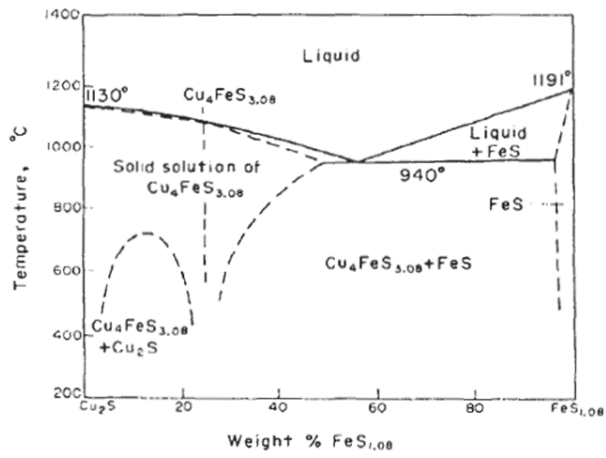


Fig. 1- 6 Cu₂S-FeS(matte) phase diagram [3].

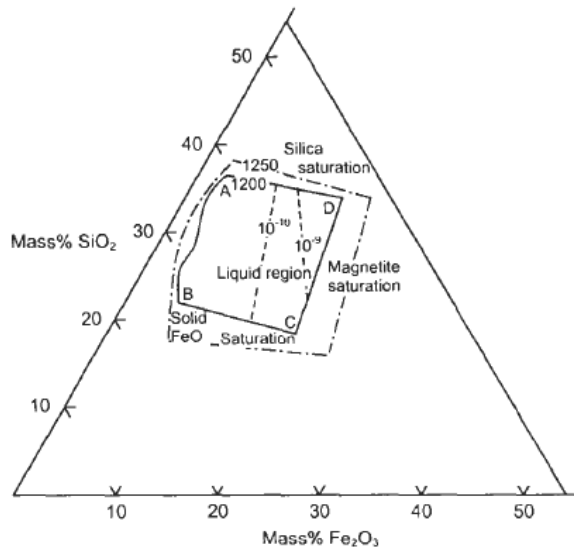
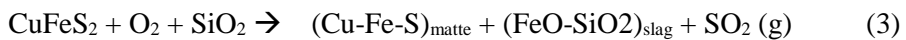


Fig. 1- 7 Liquidus surface in the FeO-Fe₂O₃-SiO₂ system at 1200°C and

1250°C (Muan, 1955) [3].

The primary purpose of smelting furnace is to transfer the sulfide minerals in copper concentrate into three components: matte, slag and off-gas. It is achieved by reacting them with oxygen. The initial reaction takes the form of the following equation,



The off-gas containing SO_2 is generated by the smelting reaction. The strength of the off-gas is usually 10 ~ 60 vol% SO_2 . The strength depends on the type of gas containing O_2 used for smelting, the amount of air allowed to leak into the furnace and the grade of matte produced. The off-gas contain substantial level of dust up to 0.3 kg/Nm³. This dust comes from small particles of unreacted copper concentrate of flux, droplets of matte and slag that didn't settle into matte layer and volatilized elements in the copper concentrate such as As, Sb, Bi and Pb. The dust normally contains 20-40% Cu. So it is very important to recycle dust to maintain a constant level [3].

1. 3. Problems in smelting furnace

1. 3. 1. Hearth wearing

Currently, three major problems exist in smelting furnace. One of them is bottom hearth wearing. During the processing, severe reactions occur in the furnace and temperature in the furnace keeps very high. In particular, the problem is that replacement period of the hearth is every two years whereas the flash smelting furnace hearth is every nine years. All three refining processes must be stopped in order to proceed the replace the hearth. The replacement operating time is about one month. Therefore the processing cost increases due to the processing stop. This problems becomes more serious after the number of lance is increased from nine to eleven and the input of copper concentrate is increased.

1. 3. 2. Splashed matte and slag in uptake outlet

Because a large amount of oxygen and concentrates are injected and melted very rapidly, matte and slag are strongly agitated. Moreover, the large amount of matte and slag drops are splashed up and floated in the furnace. These matte and slag may be piled up in the outlet boiler and may induce many negative effects.

1. 3. 3. Lance fracture

One of the troubles which impede smelting processing is the irregular wearing down of lances through which copper concentrate, oxygen and fluxes are injected into the top of the melt. Even though lances are made of a high Cr steel A297HC, for its good resistance to corrosion and oxidation, as well as its excellent weld-ability, the life time of lances is short [5]. However irregular fracture of the lances frequently occurred during processing as shown in Fig. 1-8. During the process, the lance tip is suggested to be kept at a constant height. So lance top was welded and lance tip was aligned through visual inspection after processing stop. Irregular lance fracture causes increasing lance consumption (the lance replacement cost is more than 10 billion a year), inspection frequency and lance replacement cost. Because of processing breaks (3x daily, 1x weekly), processing cost increased and affect negative impact on furnace efficiency and also impact on CL furnace and C furnace. The exact cause for this has not yet been clearly revealed. In the present study, temperature profiles and history of the lance were also investigated to understand lance's thermal behavior during processing.



Fig. 1- 8 Fractured lances after actual processing [3].

1. 4. Previous studies for the Mitsubishi process

As the history of the adoption of Mitsubishi process was relatively short, studies regarding the process have been scarce. Though many traditional papers are reviewing paper analyzing the Mitsubishi process [9-12], yet previous investigations have been focused not on analysis of an entire full-size system representative of processing, but rather on specific local regions with simple dimension [13-18].

Moreover, the previous simulation papers studies on not on analysis of an entire nozzle system, but just on one or two nozzle system [19-22]. And previous researchers focused on the lancing system of the Mitsubishi process to solve the refractory erosion problem [4, 23-24]. E. Kimura et al investigated the lancing mechanism in a Mitsubishi smelting furnace. They examined the characteristics of a jet of gas-solid mixture using a cold model and an equation which is able to estimate the penetration depth of the solid [4]. Also, among the reported papers by LS-Nikko Copper's researchers, S. S. Park and J. S. Jang investigated the penetration behavior of the annular gas-solid jet into a liquid bath by measuring the penetration depth and compared it with the behavior of a circular jet and the effects of the physical properties of solid particles on the penetration behavior of a gas-solid jet injected into the liquid bath for both circular and the annular lances [23, 24]. (Fig.1-9 & Fig.1-10) However, previous investigations have been focused not on analysis of an entire full-size

system representative of processing, but rather on limited local regions with simple dimensions and considering the effects of gas and particles injection.

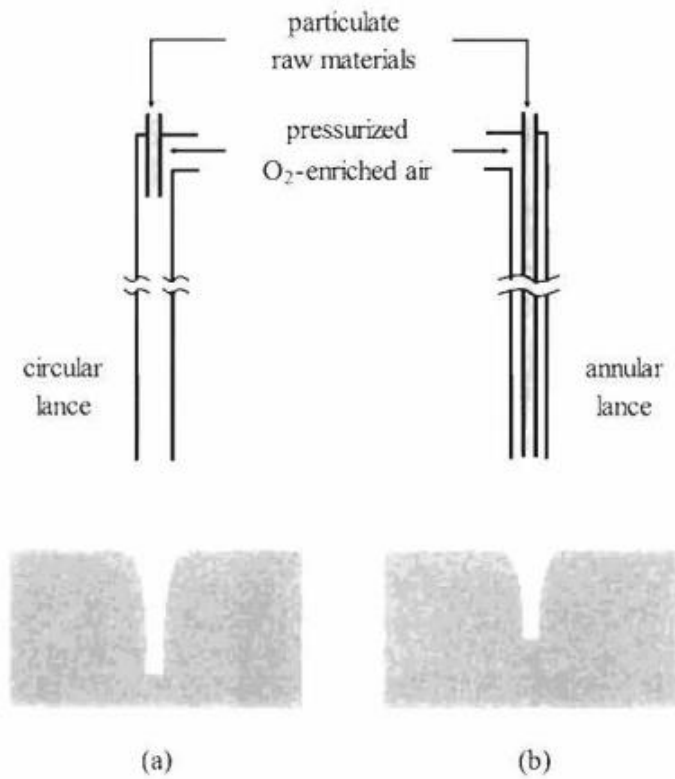


Fig. 1- 9 Experiment paper of 1-lance system about Mitsubishi smelting furnace written by researcher of LS-Nikko Copper. [23].

This picture shows schematically the proposed lance configuration (b, annular lance) compared to the existing lance (a, circular lance).

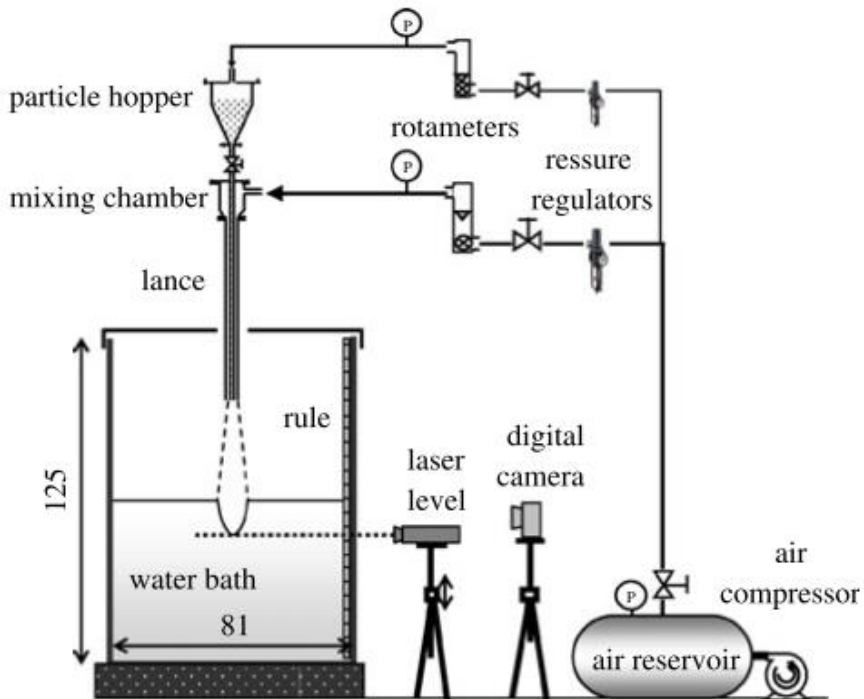


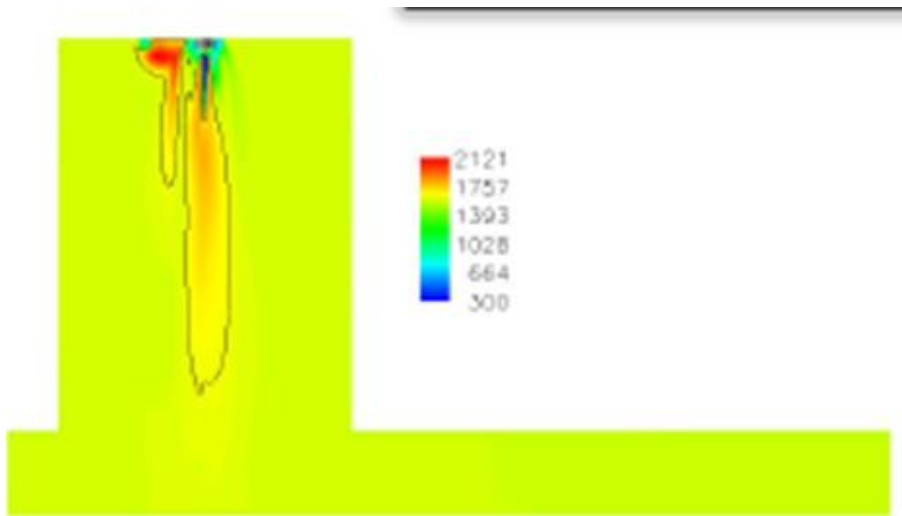
Fig. 1- 10 Experiment paper of 1-lance system about Mitsubishi smelting furnace written by researcher of LS-Nikko Copper [23, 24].

This picture shows the illustration of the experimental apparatus consisting of a liquid bath, a lance, a mixing chamber, a particle hopper and an air-supplying unit.

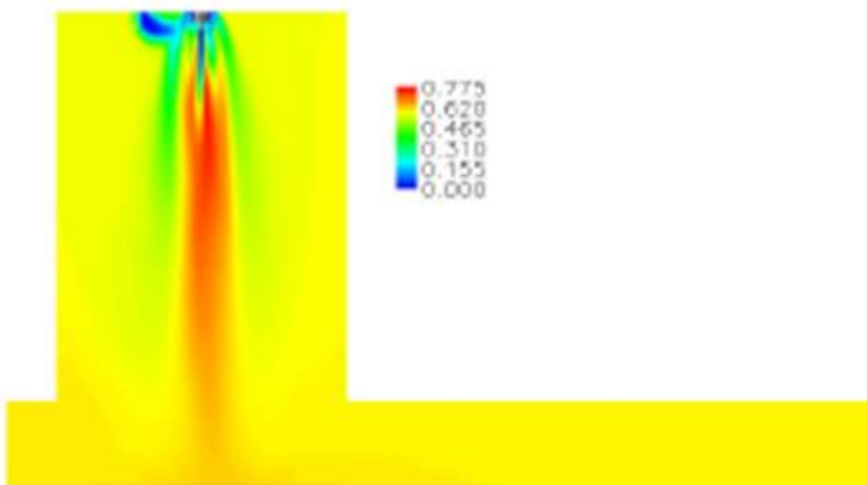
Some studies using simulation aimed at analyzing entire systems of the furnaces for other copper smelting processes [25-31]. In 1990, Y. B. Hahn

and H. Y. Sohn developed a mathematical model for the flash smelting process using TEACH code, SIMPLER algorithm and PSI-CELL technique [25]. The model was verified to adequately describe various important aspects for the phenomena occurring in the flash smelting furnace. M. Nagamori et al developed a comprehensive thermodynamic simulation model for the Isasmelt process by combining the heat balance of 48 constituent species and the equilibrium mass balance regarding Aksoy's reaction in 1994 [26]. The model permits a systematic evaluation of an operating condition, and provides a diagnosis of commercial furnace performance. Xin-feng and T. Xiao employed numerical simulation in order to optimize the product in a flash smelting furnace in 2003 [27]. (Fig.1-11) Jussi Vaarno et al developed the flash smelting/converting model, FLASH in 2003 [28]. This model could estimate gas mixture emissivity, particle absorption and scattering coefficient. However, there has been no simulation research focusing on fluid flow and heat transfer of the lance for the Mitsubishi smelting process.

Therefore, a comprehensive 3-D numerical analysis model of a smelting furnace, which can analyze transport phenomena, heat transfer and the movement of particles within a full size furnace, should be developed.



(a)



(b)

Fig. 1- 11 (a) Temperature of gas phase at 1200K (b) SO₂ content in flash smelting [25].

1. 5. Goals of the research

The purpose of this study can be divided into three parts.

At first, a comprehensive 3-D numerical analysis model of a Mitsubishi smelting furnace using in LS-Nikko Copper Ins. has been developed which has never been tried before. Because of the severe environment (high temperature, high SO₂ atmosphere, etc.) of the furnace, direct experiment on the behavior of the furnace is nearly impossible. A good alternative approach is to use numerical simulation. However, developing a comprehensive numerical model of Mitsubishi smelting furnace is very difficult because many phenomena: fluid flow, turbulence, multi-phase, heat transfer, particle tracking, radiation and reaction, etc. should be considered simultaneously to make the real system reappear with in a full size furnace. In this study, we developed a comprehensive numerical model considering many complicated phenomena. This numerical model is more valuable because this model could be applied in CL furnace and C furnace.

The second purpose of this study is to analyze the complicated phenomena during the processing of the smelting furnace using developed numerical model. We calculated many phenomena: fluid flow of the matte, slag and gas, temperature change of the lance according to injection condition, splashing of the matte and slag, temperature distribution of each phases,

movement of the particle and so on in the furnace, which has never been tried before. And we figure out what each phenomenon means in theory and analyze each of the interconnectedness. And we also obtain a lot of reliable scholarly data, utilized for improving the furnace.

Third, we solve the problems occurring in the smelting furnace to use an obtained data. Especially, we focused on the lance fracture in this study. We performed the microanalysis for lance material and compared lance temperature measurement in the experimental result with that in the calculation result. We presented the lance fracture cause, and finally proposed a solution to reduce the lance fracture using many numerical test results.

Chapter 2. Numerical modeling

2. 1. Global modeling of smelting furnace

The investigation of heat transfer and flow field using experimental measurements in Mitsubishi smelting furnace is very difficult because of the high temperature severe reaction in the furnace. So, the numerical simulation has become quite popular since it could obtain more detailed data. At the same time, the development of computers has been able to perform complicated problems in a sufficiently short time.

Numerical model was developed using a commercial package, ANSYS-FLUENT 15.0 and 1,472,575 hexagonal grids are adopted. Prototype of the model is the smelting furnace operated by LS-Nikko Copper. The grid system is shown in the Fig. 2-1. The diameter of the furnace is 10,110mm, the height is 4,000mm and the initial matte height is 1,350mm with a slag height of 150mm. The total melt height is 1,500mm.

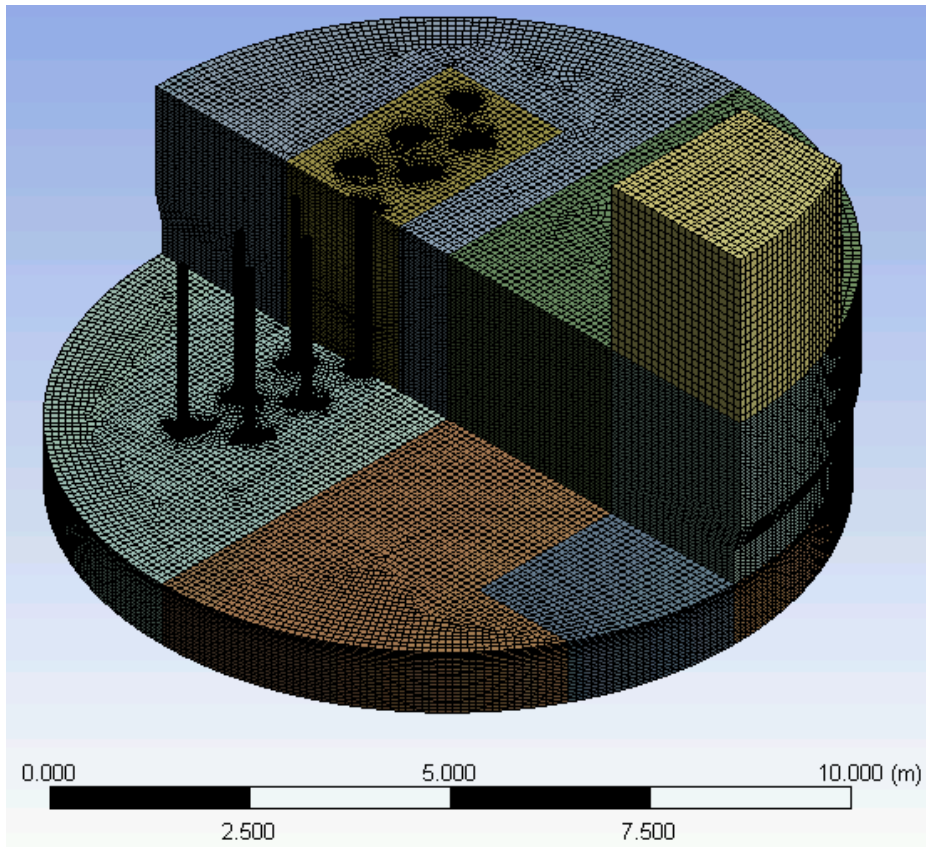


Fig. 2- 1 Grid configuration of smelting furnace.

2. 2 Simulation model

2. 2. 1. Flow

The governing equations of the mass and momentum conservation used in the model as well as the shear stress and Reynolds stress are given as follows.

Mass conservation equation is

$$\nabla \cdot U = 0 \quad (4)$$

where U is the velocity field (m/s).

Momentum conservation equation is

$$\frac{\partial \rho_m U}{\partial t} + \nabla \cdot (\rho_m U U) = -\nabla P + \nabla \cdot (\tau + T^t) + \rho_m g + f_\sigma \quad (5)$$

where ρ_m is the density (kg/m³), P is pressure (Pa), g is the gravity (m/s²)

and f_σ is the force per unit volume.

Shear stress, τ is given by

$$\tau = \mu_m \left[(\nabla U + \nabla U^T) - \frac{2}{3} \nabla \cdot U \right] \quad (6)$$

where μ_m is the dynamic viscosity (kg/m·s).

Reynolds stress, T^t is given by

$$T^t = \mu_t \left[(\nabla U + \nabla U^T) - \frac{2}{3} \nabla \cdot U \delta_{ij} \right] - \frac{2}{3} \rho_m k \delta_{ij} \quad (7)$$

where μ_t is the turbulent viscosity (kg/m·s), k is the turbulent kinetic energy (m²/s²), and δ_{ij} is the Kronecker delta.

2. 2. 2. Turbulence Model

Turbulence is calculated by the realizable k- ϵ turbulence model that has an advantage of modelling strong streamline curvature [32]. The governing equations of turbulence parameter are given as follows.

Turbulence kinetic energy (k) equation is

$$\frac{\partial}{\partial t}(\rho_m k) + \nabla \cdot (\rho k u) = \nabla \cdot \left[\left(\mu + \frac{\mu_t}{\sigma_k} \right) \nabla \cdot k \right] + G_k + G_b - \rho_m \varepsilon - Y_M \quad (8)$$

where G_k is the generation of turbulence kinetic energy (m^2/s^2) due to the mean velocity gradients and G_b is the generation of turbulence kinetic energy (m^2/s^2) due to buoyancy. Y_M represents the contribution of the fluctuating expansion in compressible turbulence to the overall dissipation rate (m^3/s^3).

Turbulence dissipation (ε) equation is

$$\frac{\partial}{\partial t}(\rho_m \varepsilon) + \nabla \cdot (\rho_m \varepsilon u_j) = \nabla \cdot \left[\left(\mu + \frac{\mu_t}{\sigma_\varepsilon} \right) \nabla \cdot \varepsilon \right] + \rho C_1 - \rho C_2 \frac{\varepsilon^2}{k + \sqrt{\nu \varepsilon}} + C_{1\varepsilon} \frac{\varepsilon}{k} C_{3\varepsilon} G_b \quad (9)$$

Turbulent viscosity (μ_t) is

$$\mu_t = \rho_m C_\mu \frac{k^2}{\varepsilon} \quad (10)$$

$C_{1\varepsilon}$, C_2 , σ_k , σ_ε are 1.44, 1.9, 1.0, 1.2 respectively [32].

2. 2. 3. Volume of Fluid (VOF)

Molten matte, liquid slag and gas phase co-exist in the furnace. The volume fractions of each phased were calculated using VOF (Volume of Fluid) model [33-37]. We assumed that matte, slag and gas phase exist in the furnace. The interface between gas and liquid in the VOF model are discontinuous at the interface, and can be calculated by the scalar transport equation of the phase indicator field. For the case of non-compressed flow, the volume fraction of the phase i in question can be obtained by the following equation [33].

$$\frac{\partial \alpha_i}{\partial t} + \nabla \cdot \alpha_i U = 0 \quad (11)$$

α_i refers to the liquid phase volume fraction.

2. 2. 4. Discrete Phase Model (DPM)

Behavior of injected particles were modelled by DPM (Discrete Phase Model) methods [38-43]. The path of a particle in a discrete phase is calculated by the particle's force balance in a Lagrangian frame. This is described mathematically as follows.

$$\frac{du_p}{dt} = F_D(u - u_p) + \frac{g_x(\rho_p - \rho)}{\rho_p} + \frac{\rho}{\rho_p} u_p \frac{\partial u}{\partial x_i} \quad (12)$$

$$F_D = \frac{18u}{\rho_p d_p^2} \frac{C_D Re}{24} \quad (13)$$

$$Re = \frac{d_p \rho |u_p - u|}{\mu} \quad (14)$$

$$C_D = a_1 + \frac{a_2}{Re} + \frac{a_3}{Re^2} \quad (15)$$

where u_p is the particle velocity (kg/m·s), u is the fluid phase velocity (m/s), μ is the molecular viscosity of the fluid (kg/m·s), ρ is the fluid density (kg/m³), ρ_p is the density of the particle (kg/m³), d_p is the particle diameter (m), F_D is the drag force (N), and C_D is the drag coefficient. During the course of calculation, particle phases and continuous phases are coupled, and exchange of mass, heat and momentum between two phases occurs.

$$S_m = \frac{\Delta m_p \dot{m}_{p,0}}{m_{p,0}} \quad (16)$$

$$F_i = \sum \left[\frac{18u}{\rho_p d_p^2} \frac{C_D Re}{24} (u - u_p) + \frac{g_x(\rho_p - \rho)}{\rho_p} + \frac{\rho}{\rho_p} u_p \frac{\partial u}{\partial x_i} \right] \dot{m}_p \Delta t \quad (17)$$

here, S_m is the mass exchange(kg) from the discrete phase to the continuous phase, Δm_p is the particle mass change in each control volume(kg), m_p is the mass flow rate of the particles(kg/s), $m_{p,0}$ is the initial mass flow rate of the particles(kg/s), and F_i is the momentum transfer. Additionally, we applied effective heat capacity for considering latent heat of the particles. The value of heat capacity was set according to piecewise-linear profile taken from previous studies [44].

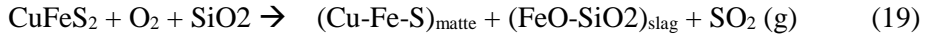
2. 2. 5. Heat Transfer

The heat transfer in the furnace is defined by solving the governing equation.

$$\rho C_p \nabla \cdot (\mathbf{v}T) = k_{eff} \nabla^2 \cdot T + S + q_{rad} \quad (18)$$

where ρ is the mass density (kg/m^3), T is the temperature (K), k_{eff} is the effective thermal conductivity of the fluid flow ($\text{W}/\text{m}\cdot\text{K}$), S is heat source generated by reactions. In the present study, we assumed that the following

reaction occurs in the smelting furnace [3].



The value of generated heat was calculated using a thermodynamic calculation program FACTSAGE [45]. The reaction did not combine with the present 3-D simulation. Instead, the calculated values of heat generation were given at the area (heat zone) where gas jet touched the melt. The amount of heat generation were assumed to be proportional to the supplied oxygen value obtained by LS-Nikko Copper. Calculated heat flux at the heat zone is about 7,250 kJ/kg·s when only gas was injected.

2. 2. 6. Radiation

The P-1 radiation model is applied, the heat flux, q_{rad} can be written as

$$-\nabla \cdot q_{rad} = \alpha G - 4\alpha\sigma T^4 \quad (20)$$

$$q_{rad} = -\Gamma \nabla G \quad (21)$$

where G is the incident radiation, α is the absorption coefficient, σ is the Stefan-Boltzmann constant and T is the temperature. Γ is the parameter defined as following equation.

$$\Gamma = \frac{1}{3(\alpha + \sigma_s) - C\sigma_s} \quad (22)$$

where σ_s is the scattering coefficient and C is the linear-anisotropic phase function coefficient. The expression for $-\nabla \cdot q_{rad}$ can be directly replaced into the energy to account for heat sources due to radiation [46].

2. 3 Initial & Boundary Condition

The temperature of the injected gas through the lance is assumed 25°C, with a velocity of 125m/s. The initial temperature of the matte, slag and gas is 1250°C. Nonslip conditions are applied at the wall. The boundary conditions of inlet and outlet are given in the Table 2-1 [47, 48].

Table 2- 1 Boundary conditions of gas and particles [47, 48].

Boundary conditions		
Inlet	Gas temperature	25°C
	Gas injection velocity	125m/s
	Particle material	CuFeS ₂
	Particle size	50 μm (diameter)
	Particle temperature	25°C
	Particle injection velocity	125m/s
	Particle mass flow rate	3.45kg/s
	Injection conditions	Gas (stage 1)
Gas + particles (stage 2)		
Outlet	Constant pressure	1 atm

2. 4 Physical properties used in numerical model

The lance has an outer diameter of 101.56mm and a thickness of 5.6mm, and it is composed of A297 HC, whose compositions and properties are listed in Table 2-1 and Table 2-2 [49]. Eleven lances were placed on top of the melt by two lows. The physical properties of the matte, slag and gas are given in Table 3 [3, 47, 48].

Table 2- 2 Composition of A297HC [49].

	C	Mn	Si	P	S	Mo	Cr	Ni	Fe
wt%	0.5	1	2	0.04	0.04	0.5	26-30	4	Bal.

Table 2- 3 Physical properties of lance [49].

Density(kg/m ³)	7528.9	Young's modulus(MPa)	1.99x10 ⁵
Coefficient thermal expansion (°C ⁻¹ at 21 °C)	1.188x10 ⁻⁵	Poisson's ratio	0.31
Specific heat(J/kg·K)	586.2	Yield strength (0.2% off set, MPa)	448.18
Thermal conductivity(W/m·K)	31.4996	Ultimate tensile strength(MPa)	482.65
Elongation (% at 21°C)	8		

Table 2- 4 Physical properties of matte and gas [3, 47].

	Matte	Slag	Gas
Density(kg/m ³)	4400	3500	1.225
Viscosity(kg/m·s)	0.01	0.6	1.7894x10 ⁻⁵
Specific heat(J/kg·K)	890	1370	1006.43
Thermal conductivity(W/m·K)	17	2.3	0.0242

Chapter 3. Fluid flow in the smelting furnace

3. 1. Calculation conditions

3. 1. 1 Injection condition & heat zone

There are two injection processes: one is gas injection, the other is gas and particle injection. We called the gas injection period as stage 1 and gas and particle injection period as stage 2. During processing gas injections and gas and particle injections appeared alternatively. Most of time in the processing, gas and particles are both injected. But only gas is injected before the processing is started and after the processing is stopped. We investigated changes in the furnace according to gas and particle injection conditions. We have conducted 20 seconds calculation to achieve the initial flow conditions. Based on the initial flow conditions, interior of the furnace is calculated over another 60 seconds. Gas is injected for the first 30 seconds. From 30 to 60 seconds, both gas and particles are injected. We called the gas injection period as stage 1 and gas and particle injection period as stage 2.

The heat zone added to region below lance where reaction mostly occurs and calculated heat flux input.



Fig. 3- 1 Gas and particle injection conditions in calculation.

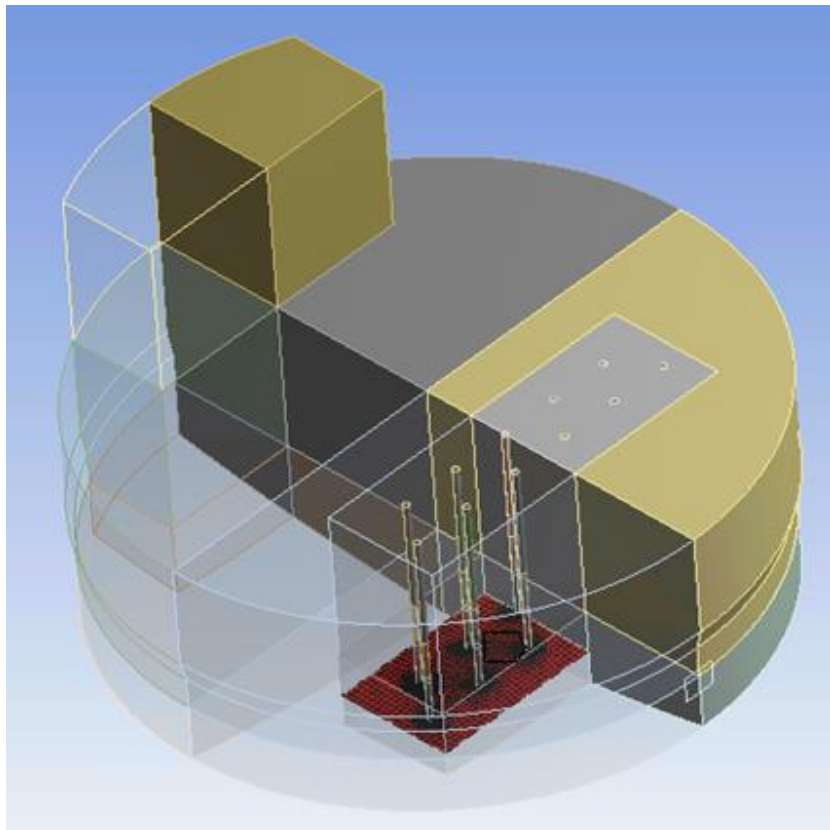


Fig. 3- 2 Heat zone region below lance. (Red area)

3. 1. 2 Measurement location

To represent the flow pattern in the furnace, we selected two cross-sections planes as shown in Fig. 3-3. Plane A is the symmetry plane of the furnace and plane B crosses the 6 lances. We investigated fluid dynamics in the furnace including uptake outlet and lances. Matte and slag velocity change and matte and slag volume fraction change depending on gas and particle injection conditions are showed at the planes. We also observed flow variations in the matte and slag, average matte and slag velocity change, average gas temperature change and average matte and slag volume fraction of the gas over time. Finally, we measured lance temperature change at the direction of thickness and height. The lance temperature measurement regions are shown in Fig. 3-4.

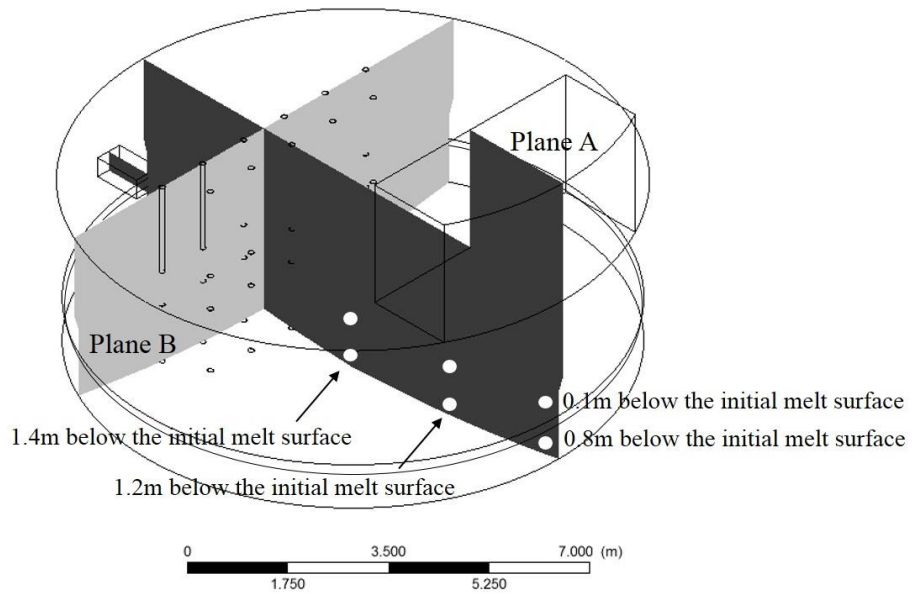


Fig. 3- 3 A: Vertical cross-section at center of uptake outlet, B: vertical cross-section of through 6 lances.

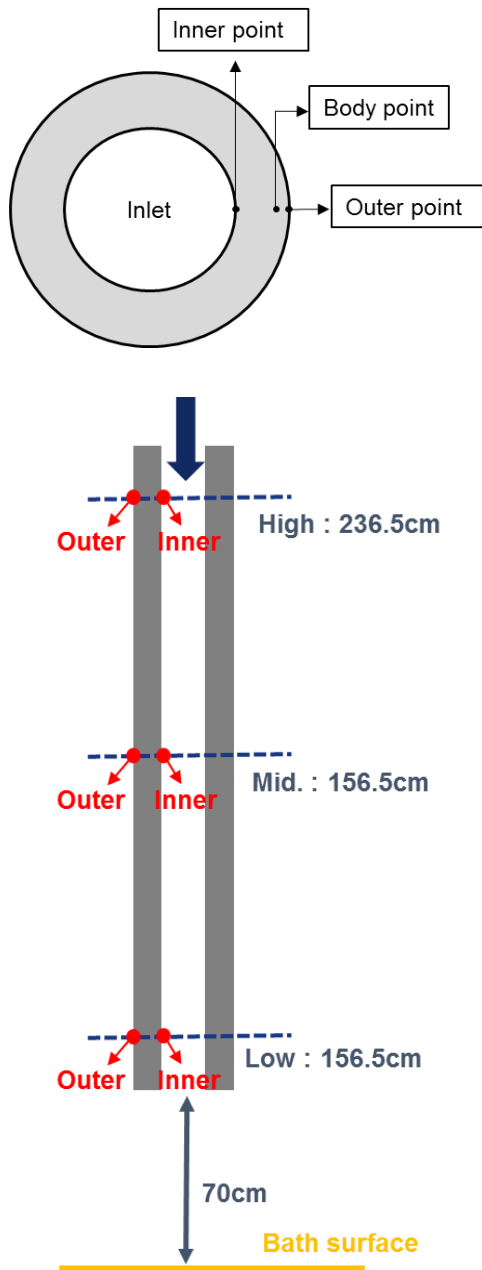
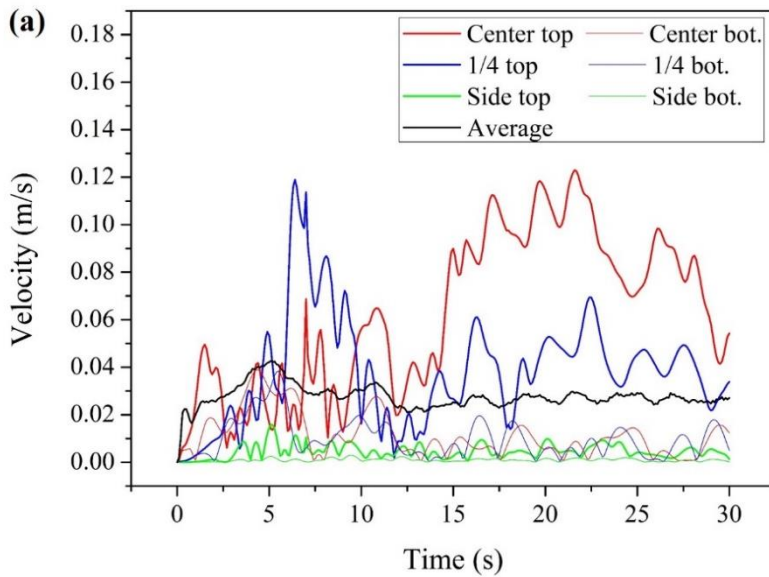


Fig. 3- 4 Lance temperature measurement regions.

3. 1. 3 The calculation initial stage

The calculation started with gas injection under the initial conditions of static state (initial velocities of melt and gas is 0). The velocities calculated from the six probe points indicated in Fig. 3-3 are shown in the Fig. 3-5 (a). The average velocities of the whole melt are increasing as time passed and fluctuating after several seconds. The velocities seemed to be irregularly fluctuating, the average value of melt region regular fluctuated as shown in Fig 3-5 (b). We start the analysis after calculation of 20 seconds.



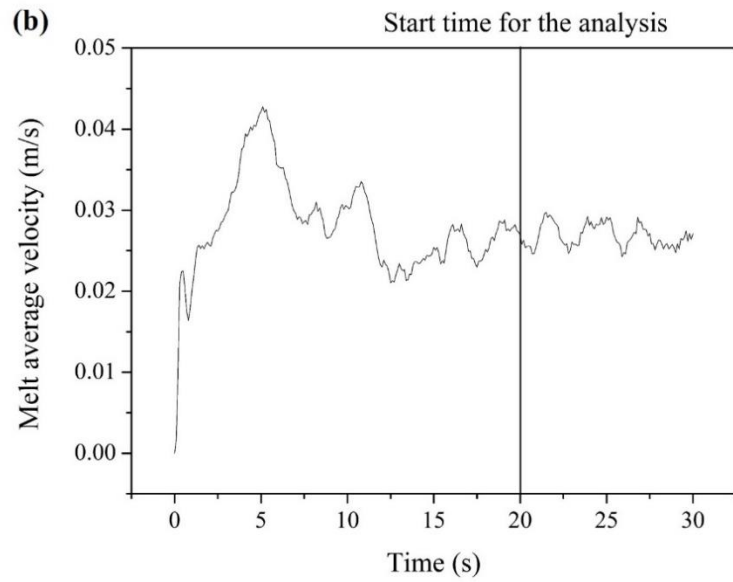


Fig. 3- 5 (a) Change of melt velocities at the six points from static initial state.

(b) Change of average melt velocity from static initial state (gas injection).

3. 2. Result and discussion

3. 2. 1. Fluid distribution

Fig. 3-6 shows velocity profiles at the plane A and plane B at different injection conditions. There is a high speed flow spraying out from the lance and the velocities under the lance are large. So large amount of matte and slag could splash to the lance, and the cavity is formed in the melt below the lance. The splashing of matte and slag will have influence on the lance. The formation of excessively deep cavity could cause severe wear on the refractory below the lance [23, 24]. In the upper part of furnace, injected gas formed a vortex. Due to this flow, splashing matte, slag and injected particles may be floating in the gas region and some amount of them can be flowing out of the furnace through uptake outlet.

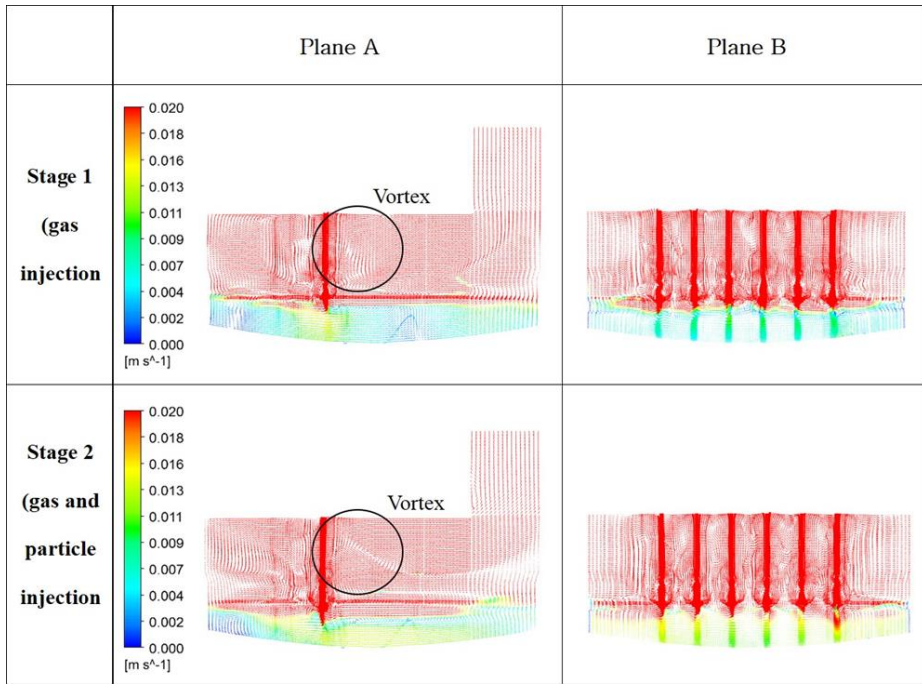


Fig. 3- 6 Velocity vector distributions with different injection conditions at the plane A and B.

Velocity profiles of the gas region during two stages were slightly different. The values of average velocity of the gas region also showed similar value as shown in Fig. 3-7. This means that the effect of particle injection on gas fluid flow is small.

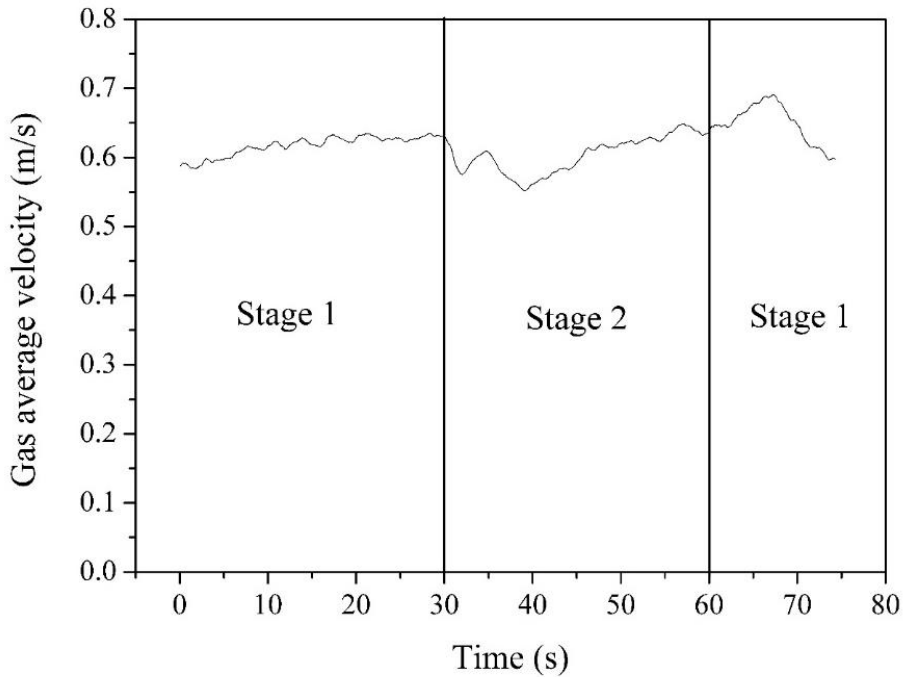


Fig. 3- 7 Change of gas average velocity. (Calculation result)

(Stage 1: gas injection / Stage 2: gas and particle injection)

Fig. 3-8 shows the change of the average melt velocity at the initial matte and slag region during calculation. As shown in the figure, melt flows were largely influenced by injection conditions. The melt average velocity during stage 2 is higher than that during stage 1. In stage 1, melt average velocity is 0.028 m/s. In stage 2, melt average velocity rises to 0.051 m/s. The

reason of this behavior is that larger momentum were transferred to the melt when stage 2 because momentum of particles were added in this stage.

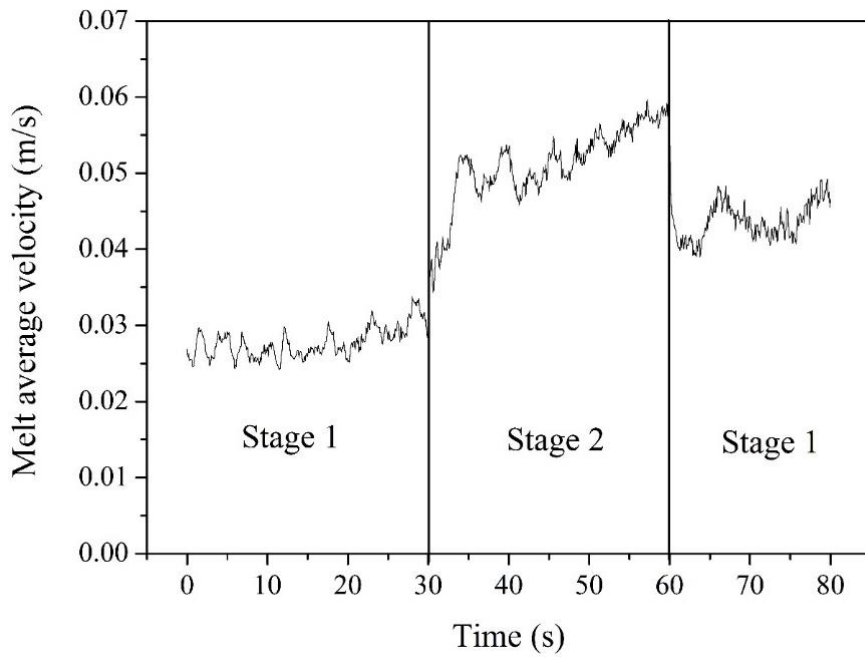
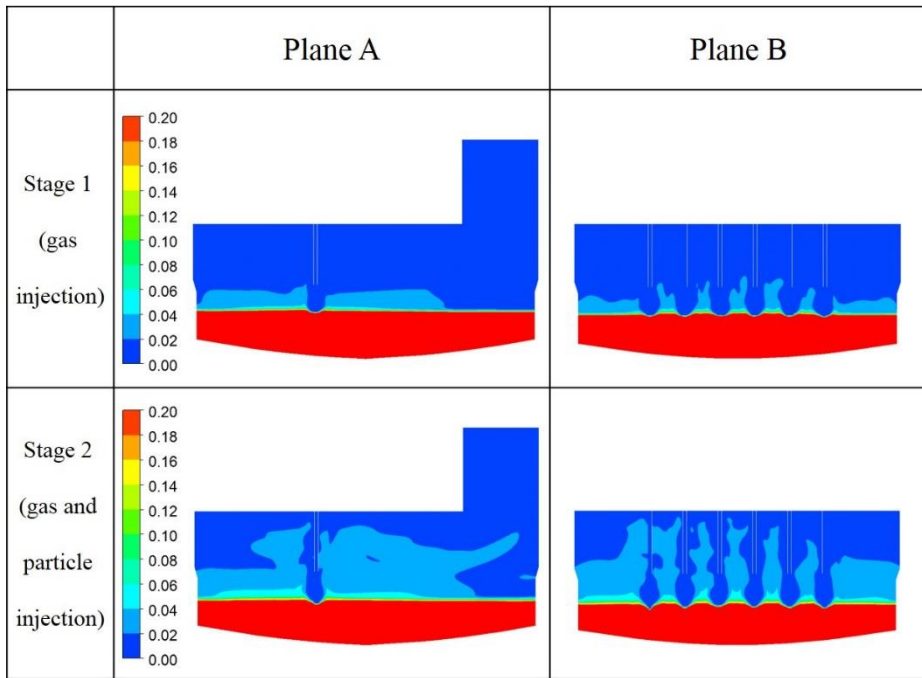


Fig. 3- 8 Change of melt average velocity. (Calculation result)

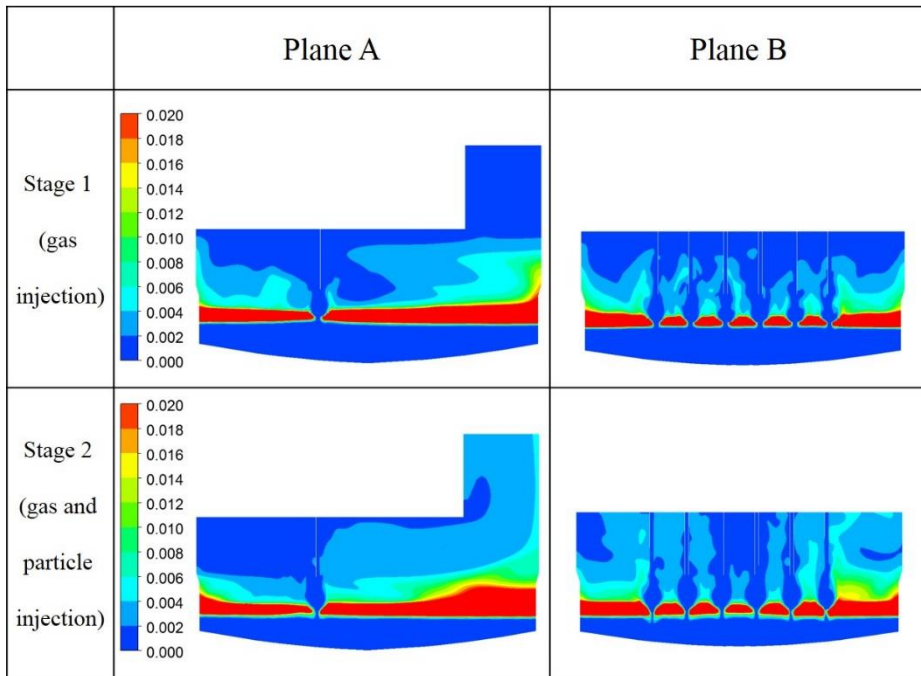
(Stage 1: gas injection / Stage 2: gas and particle injection)

3. 3. 2. Phase change

Fig. 3-9 illustrates that the matte and slag volume fraction distribution in the furnace depends on the injection conditions. As shown in the Fig. 3-9, the amounts of splashed matte and slag in stage 2 are larger than in stage 1. The amount of splashed matte and slag volume fraction are strongly related to cavity formation under the lances. From the initial melt surface, maximum depth of penetration is about -0.28m in stage 1 and about -0.42m in stage 2 if we assume that the cavity surface is located at a matte volume fraction of 0.85 [50]. Therefore deeper penetration occurs in stage 2 when gas and particles are injected together. Prolonged, excessively deep penetration phenomena in the process will have a negative effect on the bottom refractory [23, 24]. Due to the melt splashing in the furnace, the melt with high temperature splashes to the lance and make the temperature fluctuation phenomenon as shown in previous section.



(a)



(b)

Fig. 3- 9 Distribution of matte and slag volume fraction with different injection conditions at the plane A and B.

(a) Matte volume fraction (b) Slag volume fraction

Fig. 3-10 shows change of an average melt volume fraction in gas region. In stage 2, average melt volume fraction increases and reached a steady state value which is about 20% larger than the value of stage 1. From stage 2,

when gas injection condition changes to stage 1, the average melt volume fraction returned to the value of stage 1 within 20 seconds.

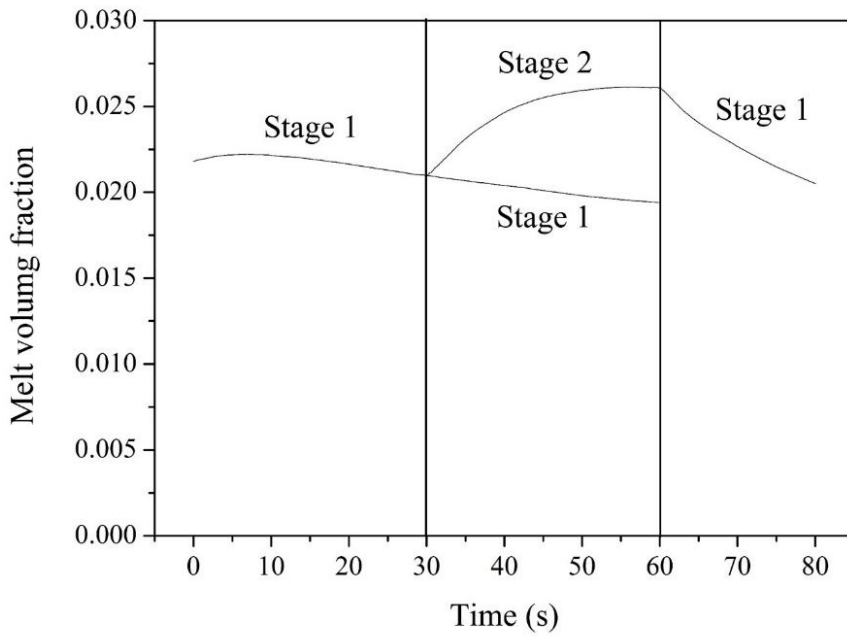
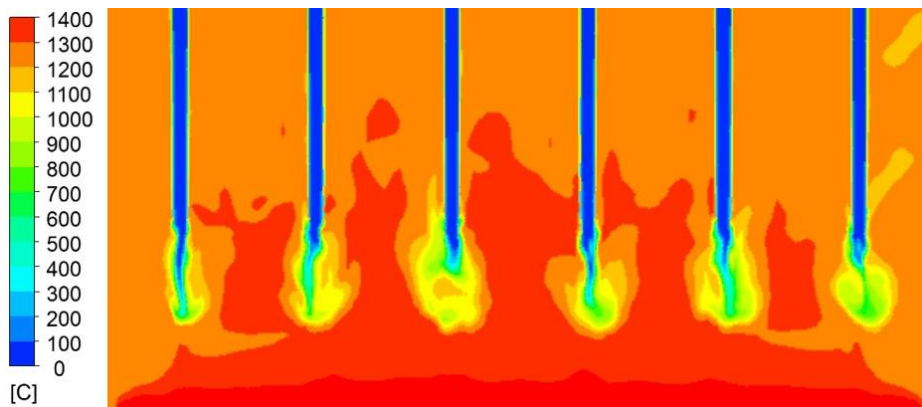


Fig. 3- 10 Average melt volume fraction variation of the gas region from 0 to 60 seconds. (Calculation result)

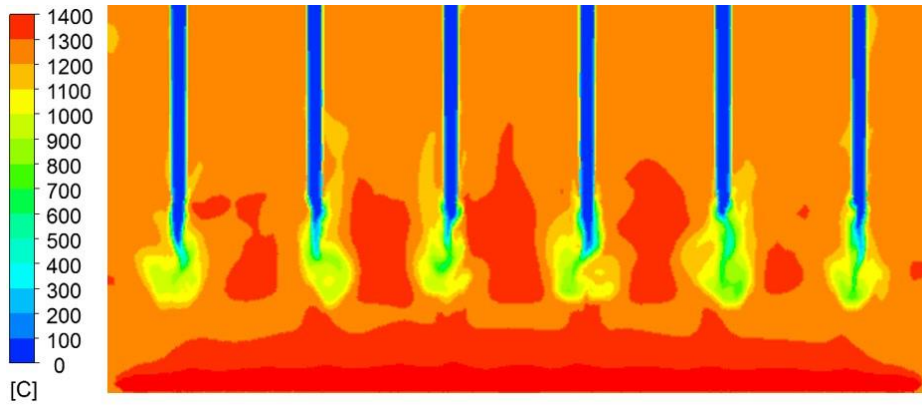
(Stage 1: gas injection / Stage 2: gas + particle injection)

3. 3. 3. Temperature distribution

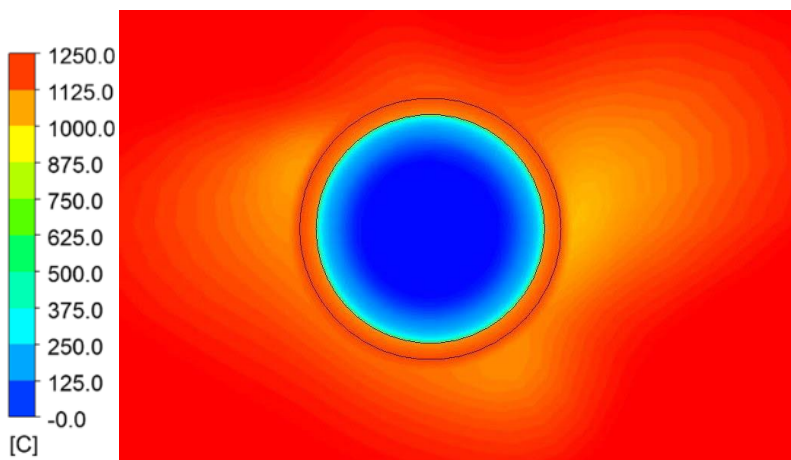
Fig. 3-11 illustrates that the temperature distribution around the lances depends on the injection conditions and cross-section plane at 10cm about lance tip. The generated heat by the input heat flux from the melt spreads out towards the lances. And the temperature near the lances decrease at the stage 2 when the cold concentrates are injected. And lance body affected by temperature between outside and inside.



(a)



(b)



(c)

Fig. 3- 11 Temperature distribution with different injection conditions around the lances.

(a) Stage 1: gas injection (b) Stage 2: gas + particle injection (c) Cross-section plane at 10cm about lance tip.

In the Fig. 3-12, the heat is transferred to the top and melt and gas temperature will be stable after the time. In the stage 2, although injected particles are cooled to melt temperature, the gas temperature gradually increase due to the heat generated in the heat zone. But cold particles considering latent heat are cooled to the melt temperature at the bath surface. This phenomenon will have a significant impact on the temperature change in the lower regions of the lance.

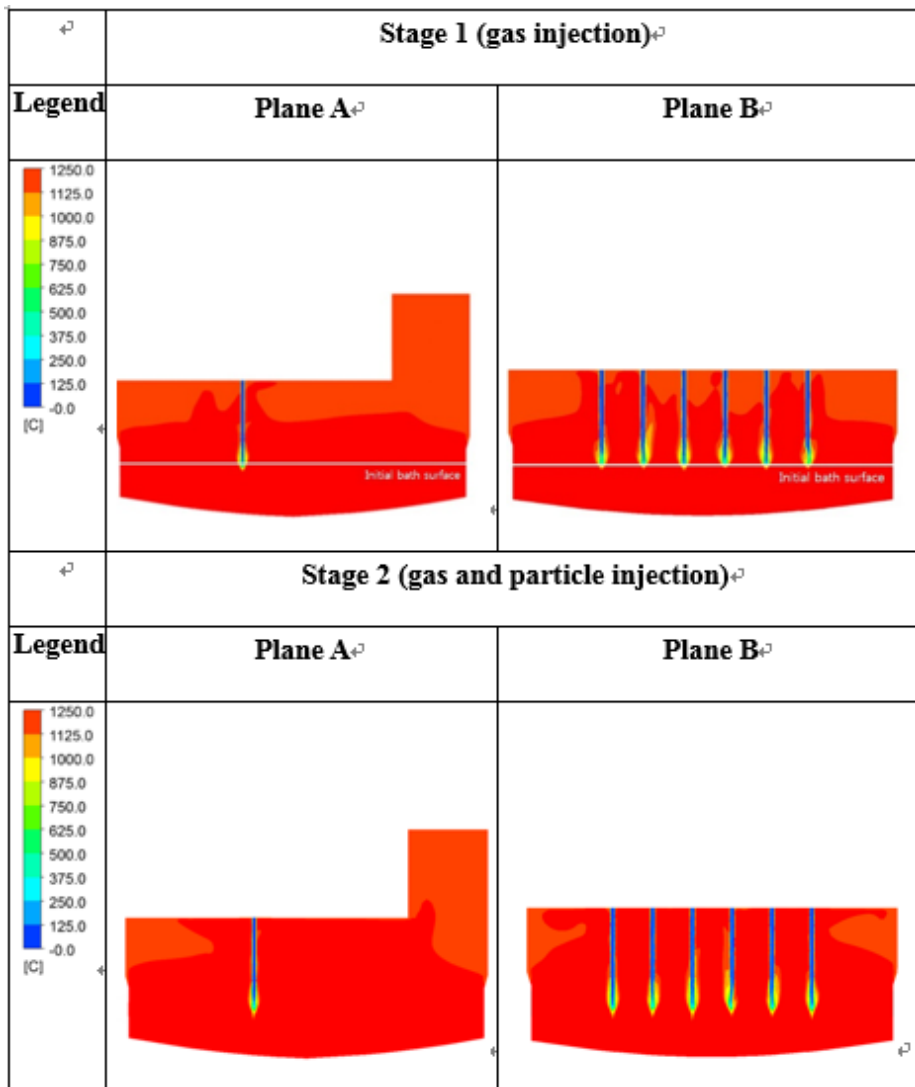


Fig. 3- 12 Distribution of temperature different injection conditions at the plane A and B.

3. 3 Summary

The fluid flow analysis has been carried out through the calculation. The flow velocity in furnace is influenced by gas and particle injection conditions. Flow is strongest below lance. The velocity of the melt layer is influenced by injection conditions. In contrast, velocity of the gas layer remains unchanged regardless of injection conditions. Melt is splashed significantly even when only gas is injected. Splashing becomes stronger when particles are injected as well. Splashed melt can have a negative influence on outlet and bottom hearth. Hot splashed melt can result in temperature change of lance. Heat is generated in the heat zone, and interior temperature rises depending on input heat flux. There is a high likelihood of this having an impact on temperature change in the lower regions of the lance.

Chapter 4. Temperature behavior in the lance

4. 1. Calculation conditions

4. 1. 1 Lance fracture phenomenon

Lance fracture problem has appeared since equipment expansion in 2008. Lance fracture randomly occurred and the exact cause for fracture has not been clearly revealed until now. During the process, the lance tip is suggested to be kept at a constant height for the smelting reaction. So lance top was welded and lance tip was aligned through visual inspection after processing stop. Irregular lance fracture causes increasing lance consumption, inspection frequency and lance replacement cost. Because of processing breaks (3x daily, 1x weekly), processing cost increased and affect negative impact on furnace efficiency. And processing breaks also influence negative impact on CL furnace and C furnace. Fractured lances are shown in Fig 1-1 and process of lance wearing is shown in Fig 4-1.

In the present study, temperature profiles and history of the lance were investigated to understand lance's thermal behavior during processing.

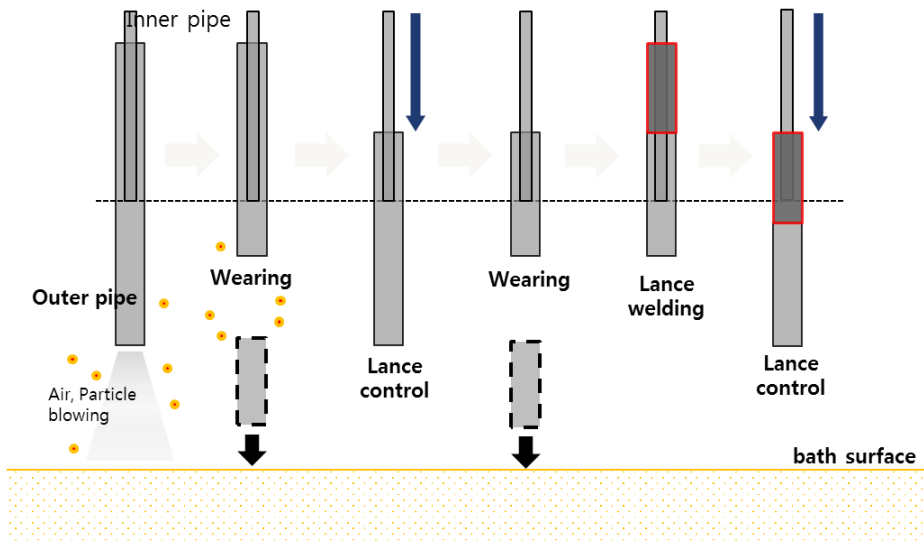


Fig. 4- 1 Process of lance wearing.

4. 1. 2 Experimental measurement

In order to compare the calculation and experiment results, we referred the lance temperature measurement result tested by LS-Nikko Copper on 2008. Temperature changes in the furnace during an operation were measured by a thermo-couple embedded into lance. And the measured data were used to verify the validity of numerical simulation. The position of the thermocouple is shown in the Fig. 4-2. Temperature was measured at a frequency of once every second with copper concentrate fed repeatedly at an interval of 10 minutes.

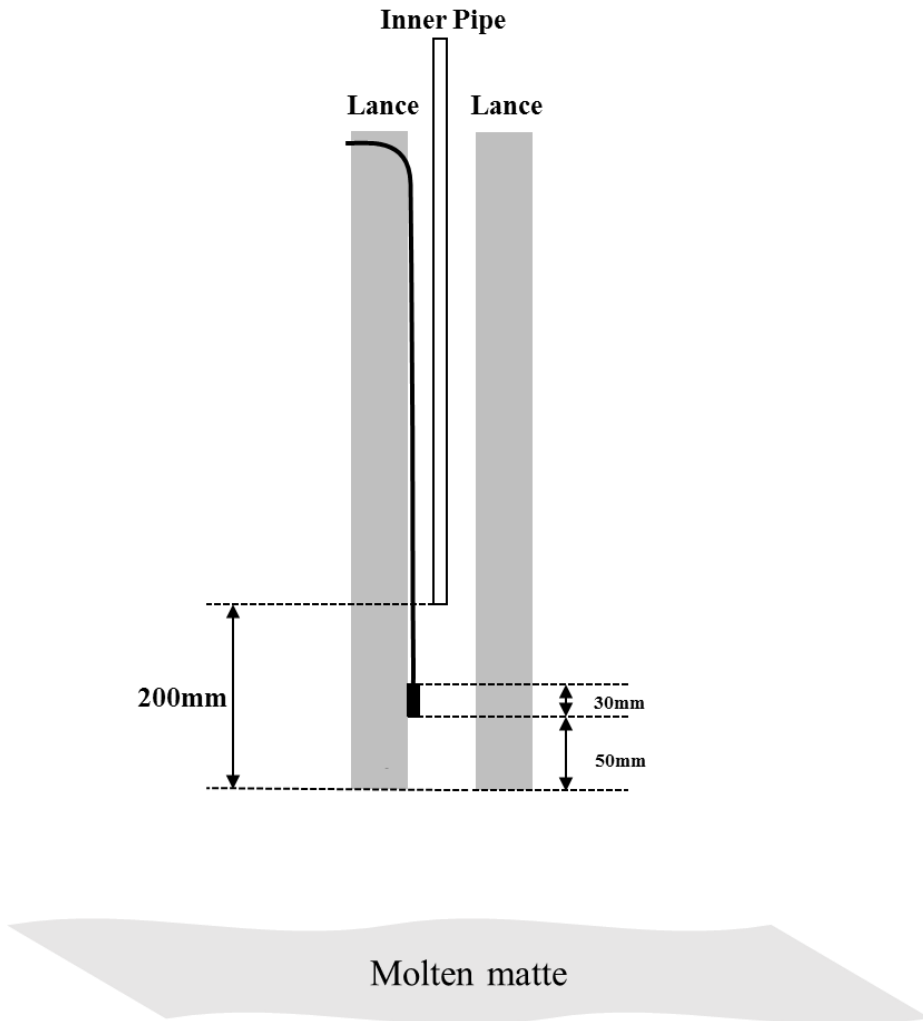


Fig. 4- 2 Thermocouple location in the processing.

4. 2. Result and discussion

4. 2. 1. Temperature change

The measured temperature variations of the lance in the processing are given in the Fig. 4-3.

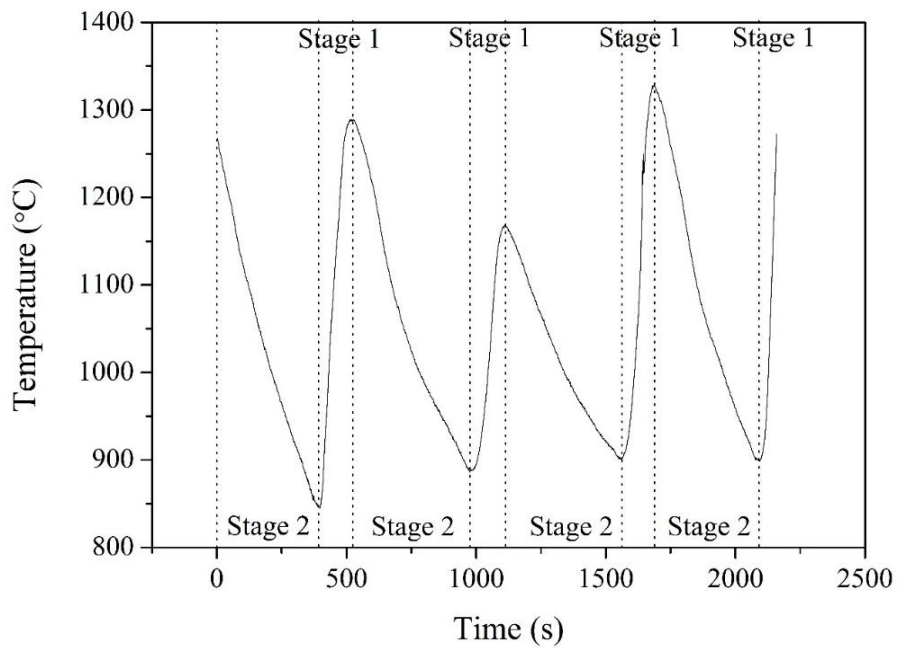
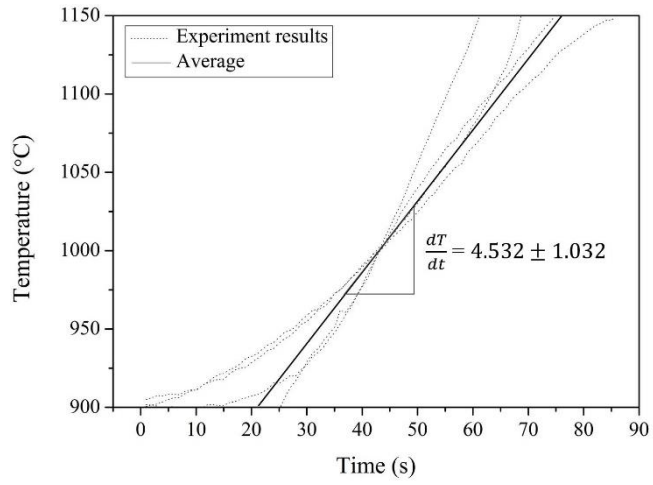


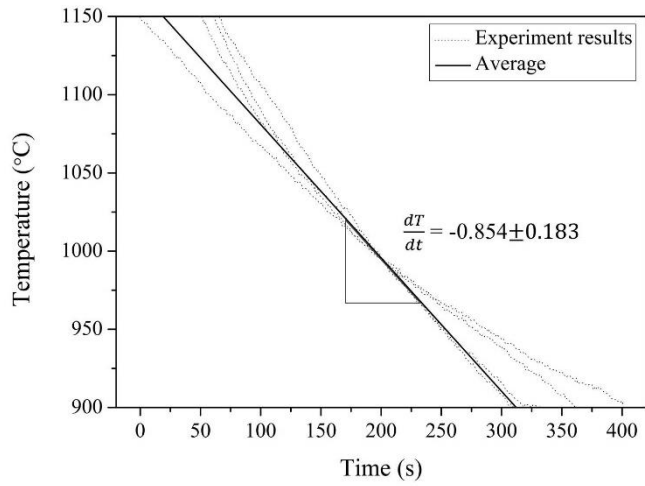
Fig. 4- 3 Temperature variation of the lance. (In processing)

(Stage 1: gas injection / stage 2: gas + particle injection)

In case of feeding from lance tip, temperature drops to 800°C, when no feeding occurs, lance temperature rises to 1300°C. Temperature was increasing at stage 1. The temperature behavior at each stage in the Fig. 4-3 are plotted in Fig. 4-4 (a) and (b). The average value of the lance temperature increasing rate is $4.532(\pm 1.032)^{\circ}\text{C}/\text{second}$ when gas was injected. Numerical simulation also shows similar value of temperature increasing rate ($3.98^{\circ}\text{C}/\text{second}$) as shown in Fig. 4-5. This should be caused by the exothermic reactions in the furnace. On the other hand, temperature was decreasing when gas and particles were injected simultaneously (stage 2). The decreasing rate of measured temperature was $0.854(\pm 0.183)^{\circ}\text{C}/\text{second}$. Numerical simulation was also showed that the temperature was decreasing with similar value of $0.87^{\circ}\text{C}/\text{second}$. The amount of reactions in the stage 2 was same to stage 1 in the calculation because the amount of injected oxygen was same. This temperature decrease may be caused by the heat extraction of cold concentrates from lance.



(a)



(b)

Fig. 4- 4 Temperature profile in processing.

(a) Stage 1: gas injection (b) Stage 2: gas + particle injection.

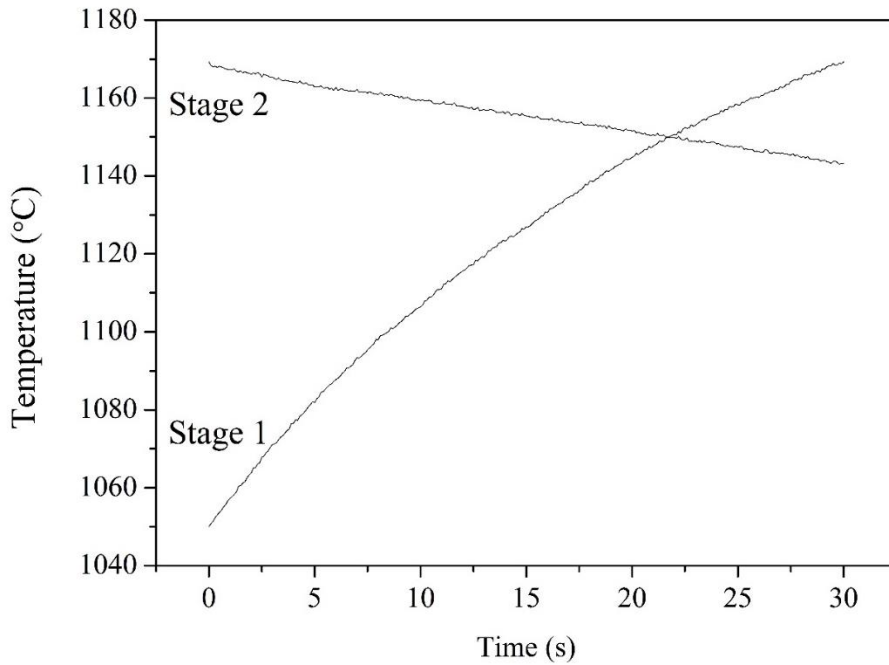


Fig. 4- 5 Temperature variation of the lance from 0 to 30 seconds.

(Calculation result)

(Stage 1: gas injection / stage 2: gas + particle injection)

Lance temperature variation occurs without use of chemical reaction model through reflection of heat flux and heat absorption by particles. Temperature increase at lance tip for gas injection and decrease for gas and particle injection in good agreement with experiments. From this result, comparison between

calculation and experiment regarding trends of heat received by lance made possible. This temperature decrease may be caused by the heat extraction of cold concentrates from lance because the exothermic reaction still occurred.

Table 4- 1 Comparison of the temperature variation of the lance between the experiment and calculation.

	Avg. velocity	Max. velocity	Min. velocity	Stdev.	Temp. range
Increase (experiment)	4.53°C/s	5.36°C/s	2.95°C/s	1.032	900- 1150°C
Decrease (experiment)	0.85°C/s	1.04°C/s	0.62°C/s	0.183	900- 1150°C
Increasing (calculation)	5.48°C/s				1060- 1160°C
Decreasing (calculation)	1.30°C/s				1160- 1190°C

We have measured the lance temperature not only at the lower, upper but also inner, outer regions. Fig. 4-6 and 4-7 show that distinct increase and

decrease of temperature occurred at lower region of the lance. Although the time is short, temperature variation exceeds 100°C. On the other hand, temperature variation trend at middle, upper region are different from lower region. No trends of temperature increase and decrease. The reason is that lance tip is directly influenced by reaction heat, radiation heat of the matte and heat absorption of particles. But middle and upper region are less influenced by the heat. In particular, lance temperature fluctuation phenomenon become obvious toward upper region. And the trends of temperature at central and outer lances are similar.

Fig. 4-6 and 4-7 also show that lance temperatures at the outer wall is higher than inner position. The temperature differences occurs between lance inner and outer surfaces, as 25°C gas and particles are injected through interior while outer temperature is high at above 1250°C. The Fig. 4-8 and 4-9 show that the temperature difference is approximately 60°C at lance lower region, up to 100°C at mid-upper region. This large value of temperature difference should generate thermal stress across the lances.

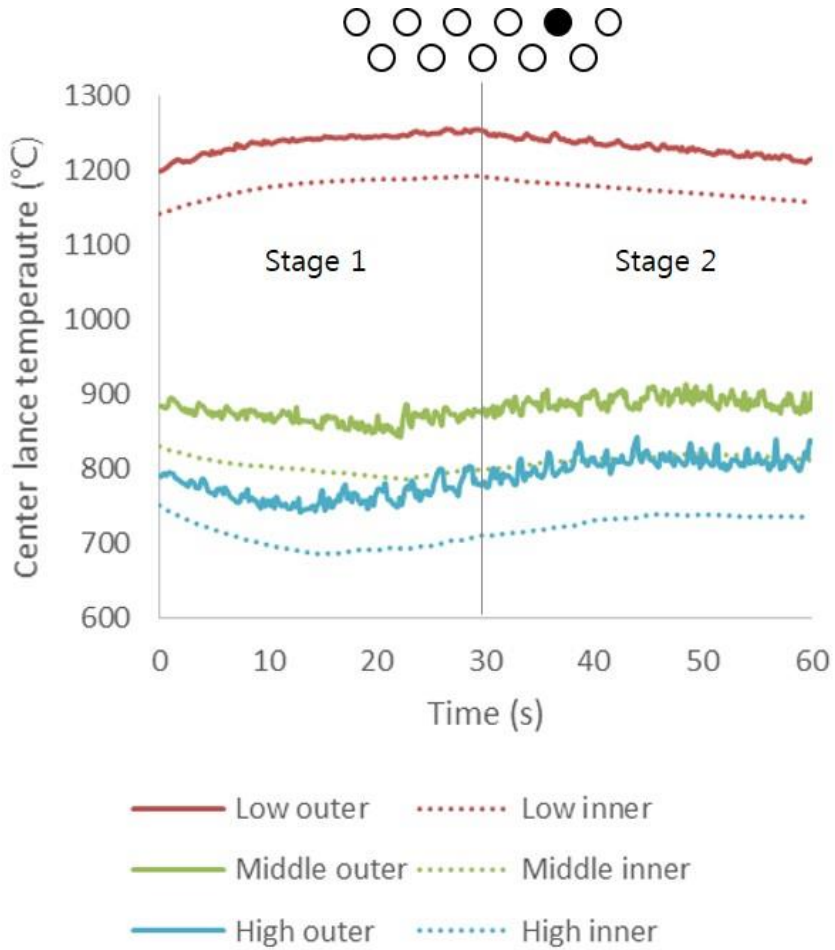


Fig. 4- 6 Temperature variation of the lance from 0 to 30 seconds.

(Calculation result)

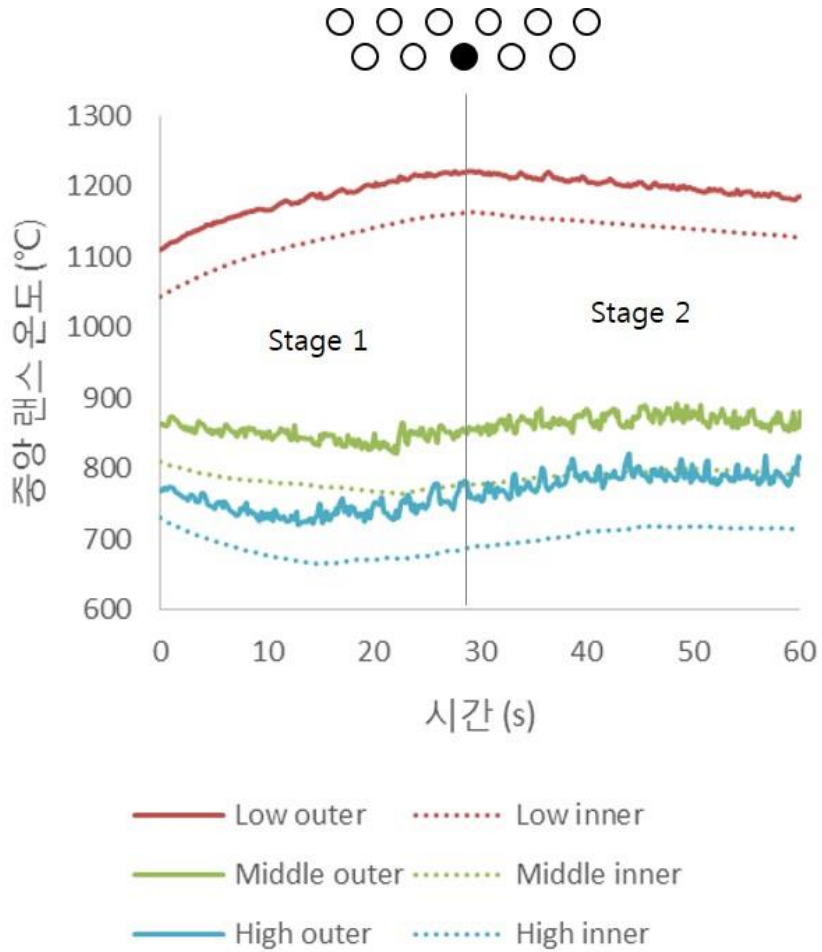


Fig. 4- 7 Temperature variation of the lance from 0 to 30 seconds.

(Calculation result)

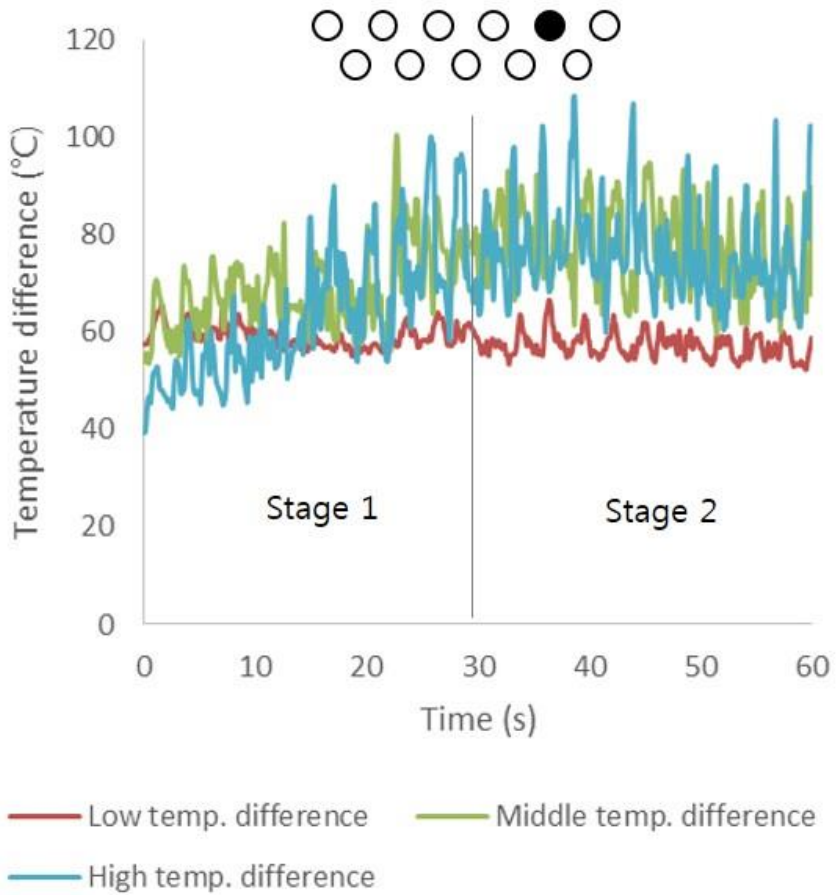


Fig. 4- 8 Temperature variation of the lance from 0 to 30 seconds.

(Calculation result)

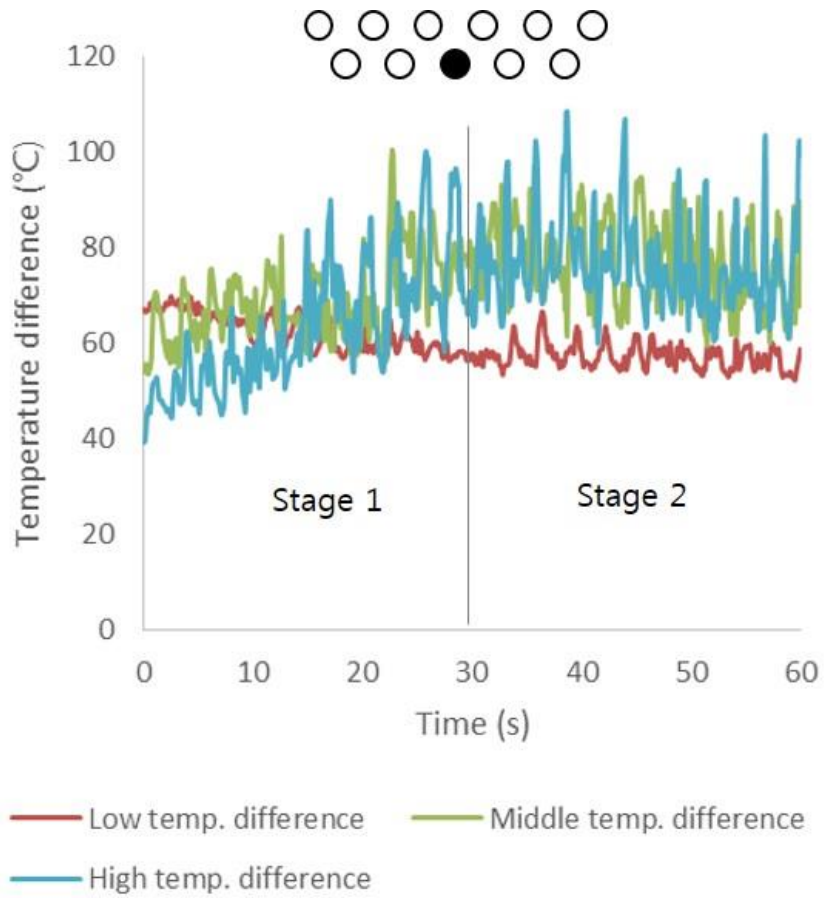


Fig. 4- 9 Temperature variation of the lance from 0 to 30 seconds.

(Calculation result)

4. 2. 2. Temperature fluctuations behavior

Measured temperature values showed small temperature fluctuations with period about 2-3 seconds as shown in Fig. 4-4. This temperature fluctuations phenomenon are also found similarly in the numerical results as shown in the Fig. 4-5. Fast Fourier Transforms of both results of stage 2 show similar peak values as shown in Fig. 4-10. This suggests that both fluctuations have the same origin.

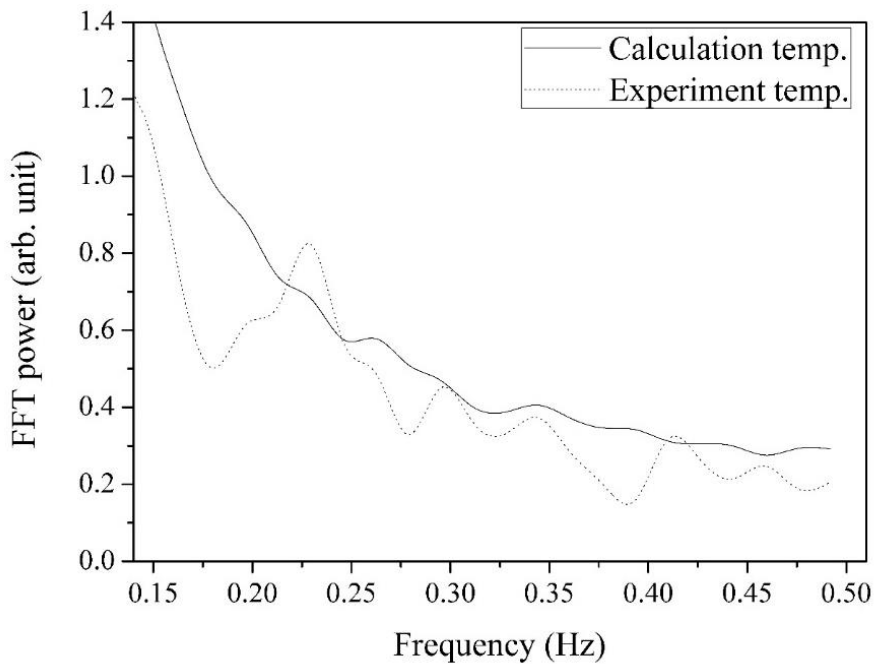
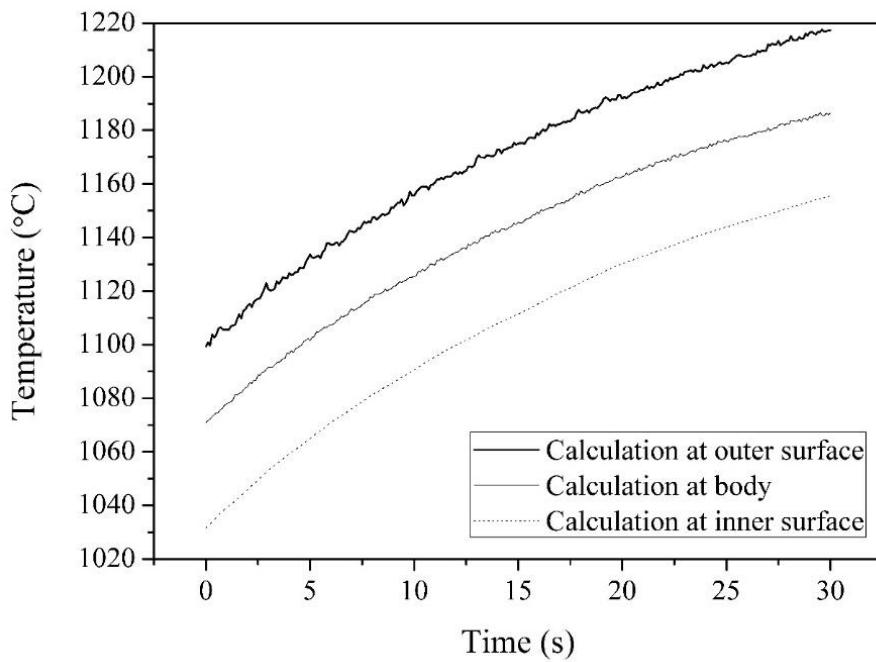
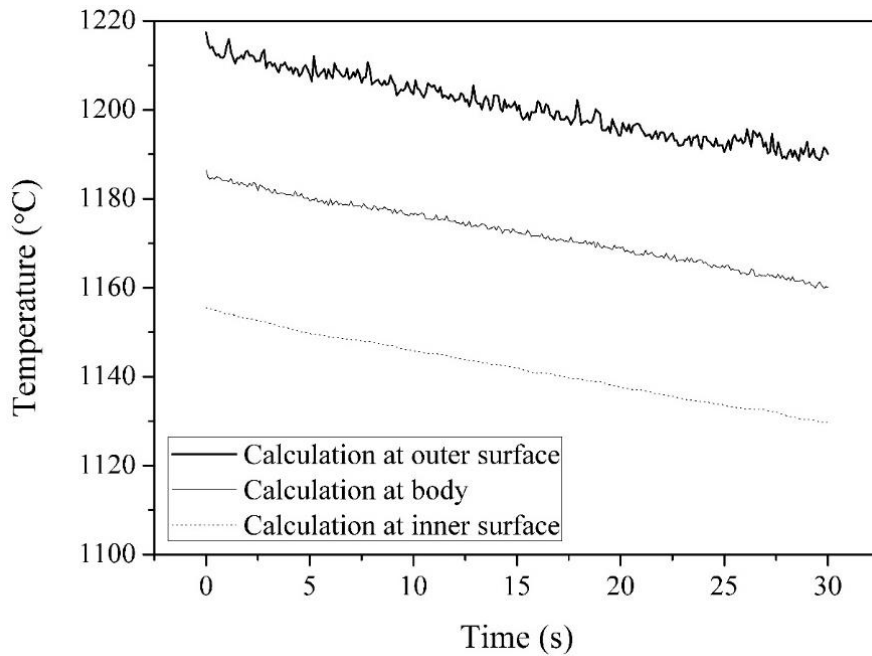


Fig. 4- 10 FFT analysis result of calculation and experimental results at stage

The temperature changes at the inner, middle and outer positions of lance were plotted in Fig. 4-11. Temperature of outer positions showed clear and larger values of fluctuations, and the fluctuation was attenuating at the inner positions. This result shows that these fluctuations were induced from outside of the lance in other words, gas phase of the furnace.



(a)



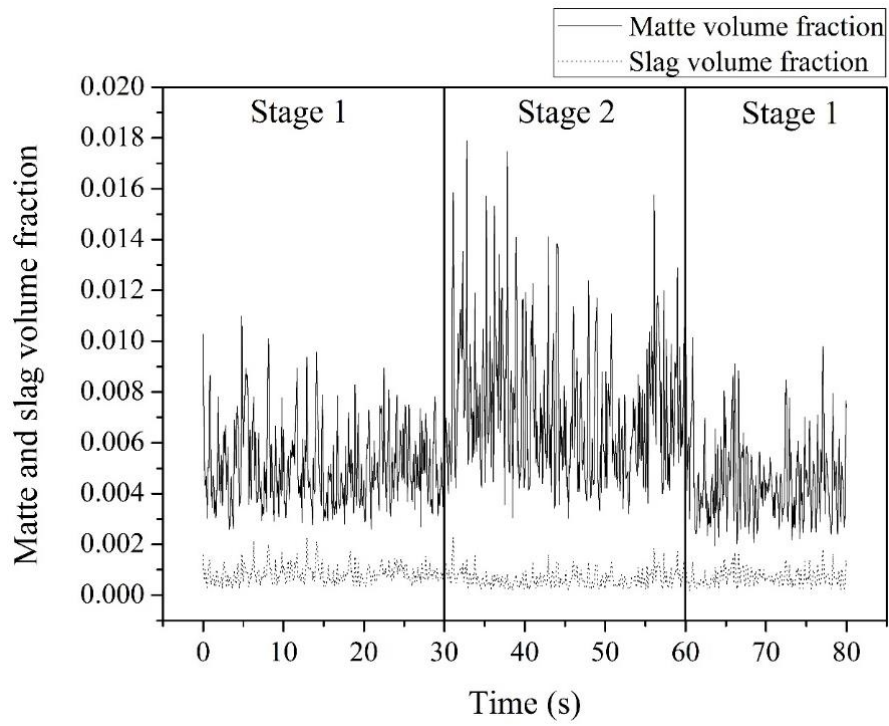
(b)

Fig. 4- 11 Temperature fluctuation comparison at inner surface, body and outer surface of the lance. (Calculation result)

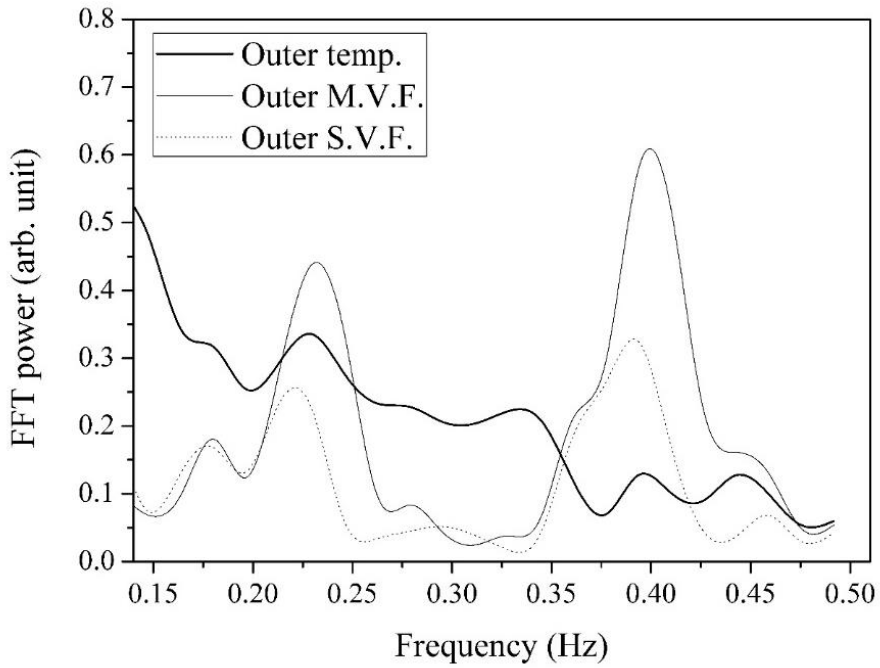
(a) Stage 1: gas injection (b) Stage 2: gas + particle injection.

We assumed that this high frequency temperature fluctuation can be caused by the splashed melt particles, so the changes of matte and slag volume fraction at 0.1mm distance away from the outer surface of the lance are compared to the

temperature changes of the lance. As Fig. 4-12 (a) shows, the matte and slag volume fraction at the lance surface fluctuates in both injection cases. Standard deviations of matte volume fractions in stage 1 and stage 2 are 0.001663 and 0.002847, respectively. This shows that the value of fluctuation at stage 2 is larger than stage 1. Frequencies of Fast Fourier Transform of matte and slag volume fraction and outer temperature show same values as shown in Fig. 4-12 (b). The analysis of splashed matte, slag and temperatures of different positions of the lance shows that fluctuation of matte and slag volume fractions induces thermal fluctuations in the lance. If the high temperature matte and slag with high thermal heat capacity splashes onto the lance, lance temperature will be instantly increased and induce temperature fluctuation in the lance. The reason for the severe temperature fluctuation in stage 2 is increased splashed melt because of particles injection.



(a)



(b)

Fig. 4- 12 (a) Matte and slag volume fraction variation 0.1m distance away from the outer surface of the lance. (Calculation result)

(b) FFT analysis results of lance temperature and matte & slag volume fraction.

(Stage 1: gas injection / stage 2: gas + particle injection)

Fig. 4-11 shows that lance temperature at the outer wall is higher than

at the inner position. The temperature difference across wall of lance is about 60°C as shown in Fig. 4-13. This is because the gas on the outer wall of the lance has a higher temperature, whereas colder gas is injected along the inner wall of the lance. This large value of temperature difference should generate thermal stress across the lances. Furthermore, the temperature difference fluctuated as shown in Fig. 4-13 because the temperature of outer wall of the lance is fluctuated. And the temperature range of fluctuation is different according to the injection conditions. In stage 1, the value of fluctuation is about 5°C and the value of fluctuation reaches 10°C in stage 2. These change of temperature difference and fluctuations of temperature cause fluctuation of thermal stress of the lance. These thermal fluctuation phenomena are well known as thermal stripping, which is that fatigue may occur when the amplitude and number of strain cycles are sufficiently high [51-53]. Because the periods of this fluctuation are less than 4 seconds, the lances are exposed to huge amount of cyclic change of thermal stress during operations.

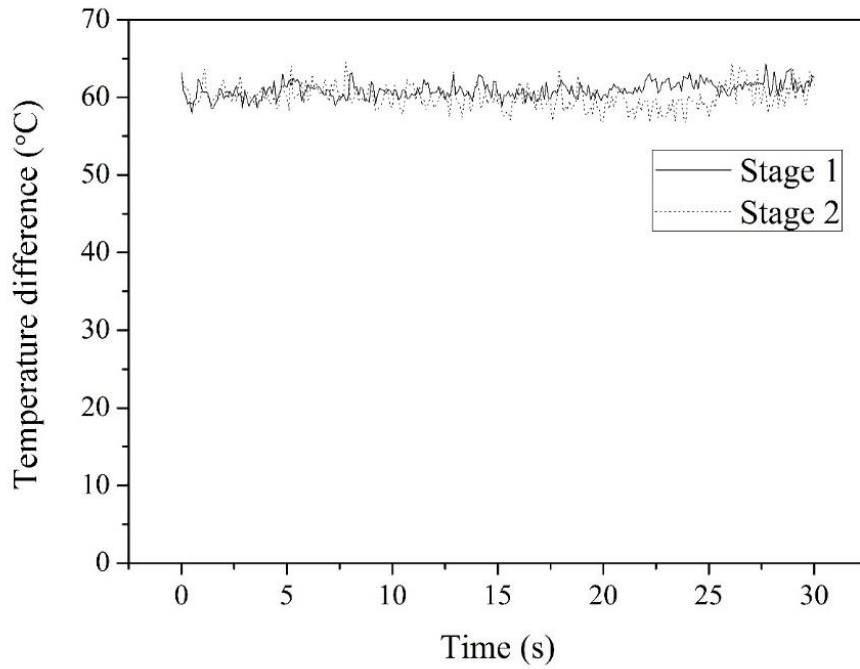
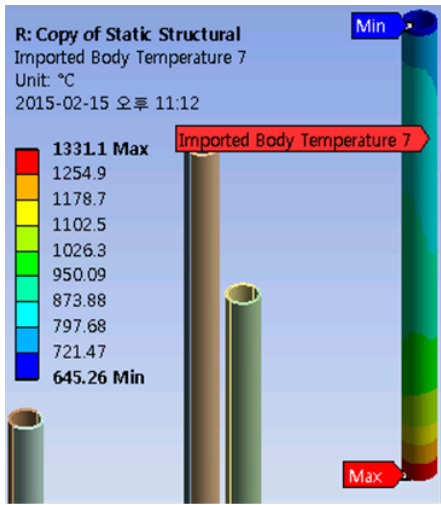


Fig. 4- 13 Temperature difference between outer wall of the lance and inner point of the lance from 0 to 30 seconds.

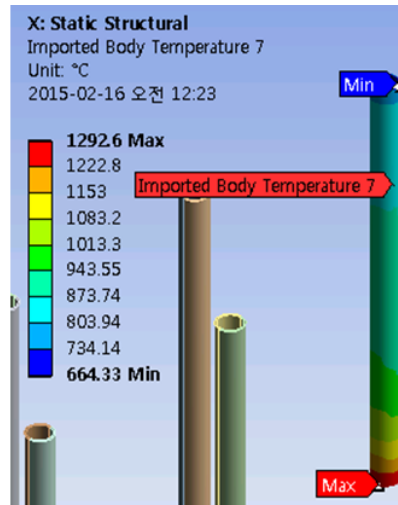
(Dotted line: stage 1 / solid line: stage)

4. 2. 3. Thermal stress of the lance

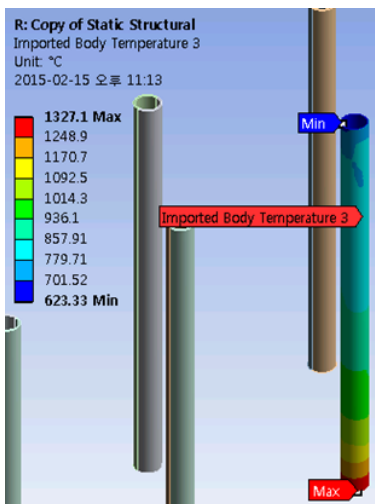
In order to analyze the thermal stress of the lance, we use 1-way FSI (Fluent Structure Interaction) method for calculation [54]. At first, load the temperature of the lance at 60 seconds (stage 2) to the ANSYS Mechanical program. Fig. 4-14 shows the lance temperature distribution depending on injection condition and lance location. The lance temperature is highest at lower region and decrease toward top. Temperature difference between bottom and top is very large, approximately 600°C. And trends of temperature at central and outer lances are similar. Due to the particle injection, maximum temperature at stage 2 is lower than that at stage 1. Then we input the lance mechanical properties into ANSYS Mechanical, calculated the thermal stress of lance. Fig. 4-15 shows lance normal stress depending on injection condition. The maximum legend value was changed to 100 MPa. The stress direction is different between interior and exterior. The reason caused by high temperature at lance exterior, low temperature at lance interior due to injected gas and particles. So I anticipate that tensile stress occurs inside lance and compressive stress occurs outside lance. In the result of the normal stress and principal stress of the lance, it was confirmed qualitatively that the stress direction of outside lance is compressive because of values are all minus, the stress of inside lance is tensile because of values are all plus. (Exact direction vector is not calculated.) Fig. 4-16 shows induced stress along the lance.



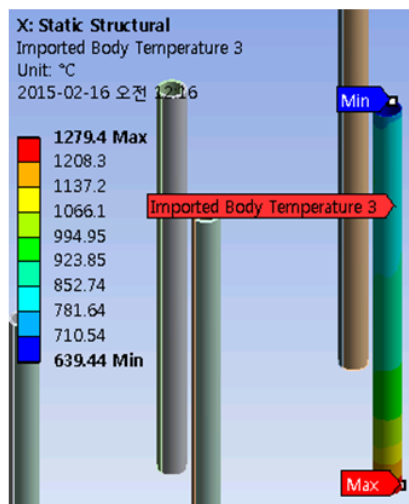
(a)



(b)

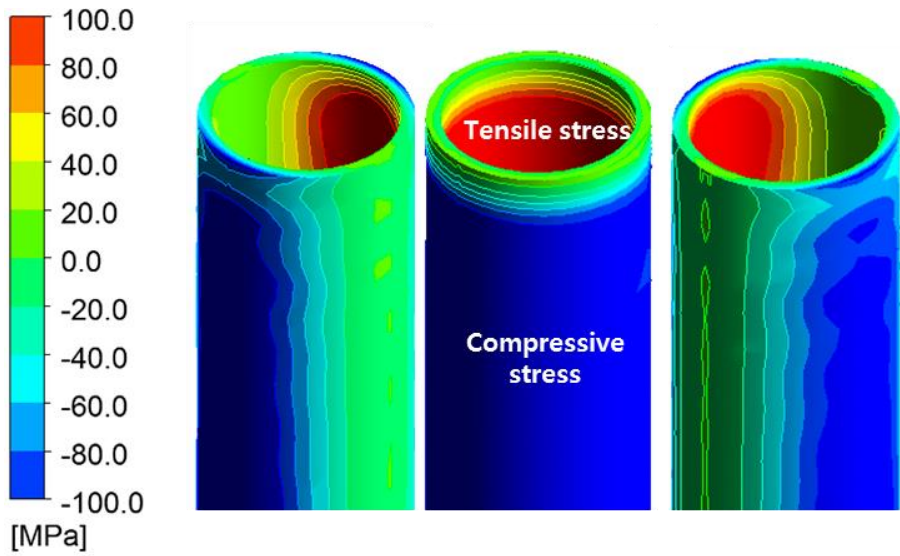


(c)

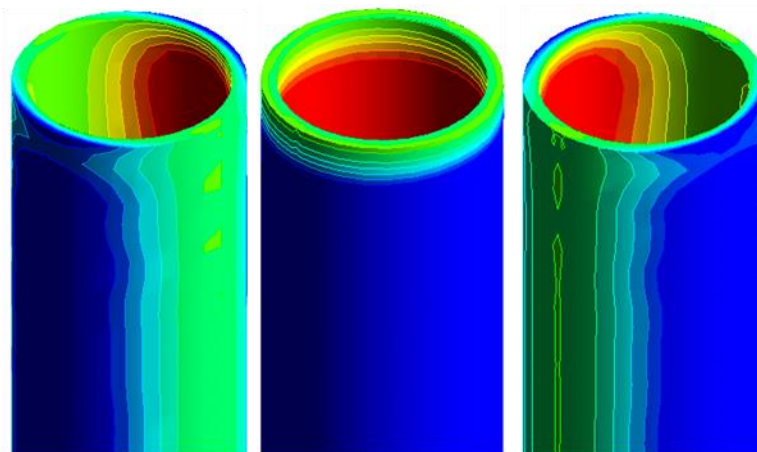


(d)

Fig. 4- 14 Lance temperature distribution. (a) Outside, stage 1 (gas injection), (b) Outside, stage 2 (gas and particle injection), (c) Central, stage 1 (gas injection), (d) Central, stage 2 (gas and particle injection)



(a)



(b)

Fig. 4- 15 Lance normal stress. (MPa)

(a) Stage 1 (b) Stage 2

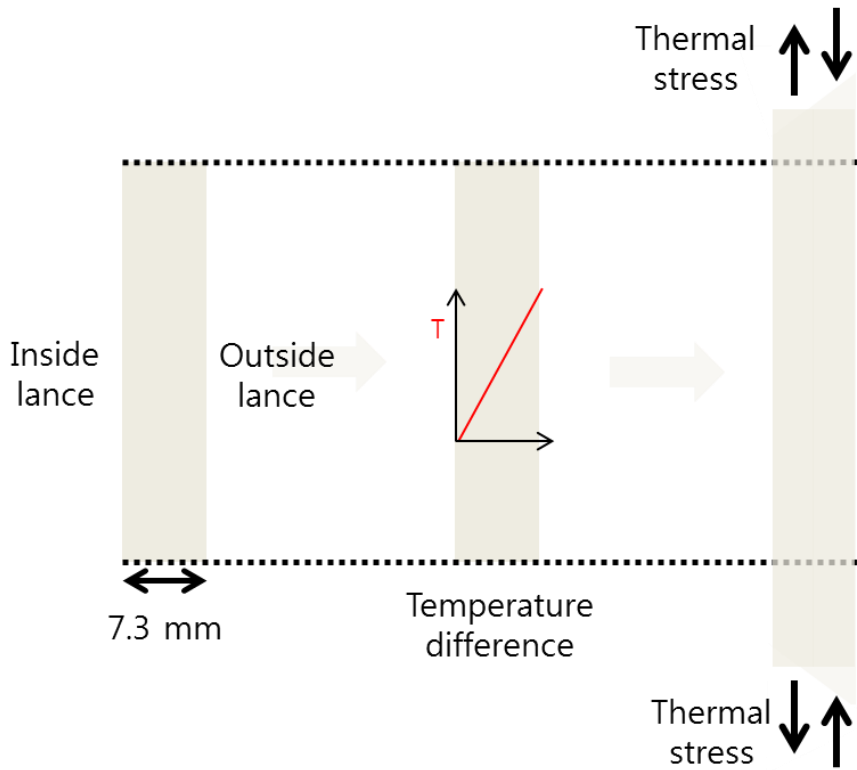


Fig. 4- 16 Stress direction of the lance.

Next, the values of yield strength of the A297HC shown in the literature and calculated equivalent stress of the lance are compared. The Fig. 4-17 shows that the yield strength of A297HC is 96.46 MPa at 760°C [49]. Calculated equivalent stress for most of lance exceeds yield strength of A297HC. This means lance undergoes thermal stress and plastic deformation during

processing. But there is no literature value of fracture strength above 1000°C.

If I could receive the data from supplier supplying the lance to LS-Nikko Copper or experiment of direct fracturing test, good comparison between calculation and experiment would be possible.

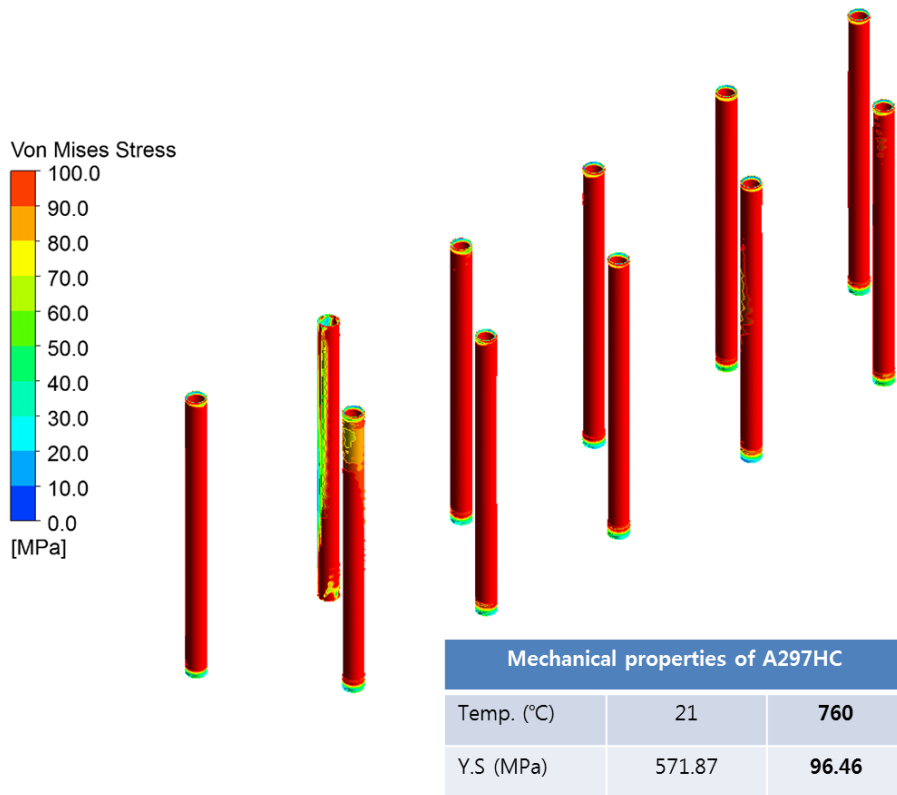


Fig. 4- 17 Comparison of calculated equivalent stress and literature yield strength (MPa) [49].

At last for mechanical analysis, yield strength of A297HC extrapolated to give a corresponding value for average temperature difference at upper, middle and lower region of lance. Fig. 4-18 shows that the yield strength is lowest at lower lance region. (Upper > middle > lower) Therefore, plastic deformation expected to be largest at lower region.

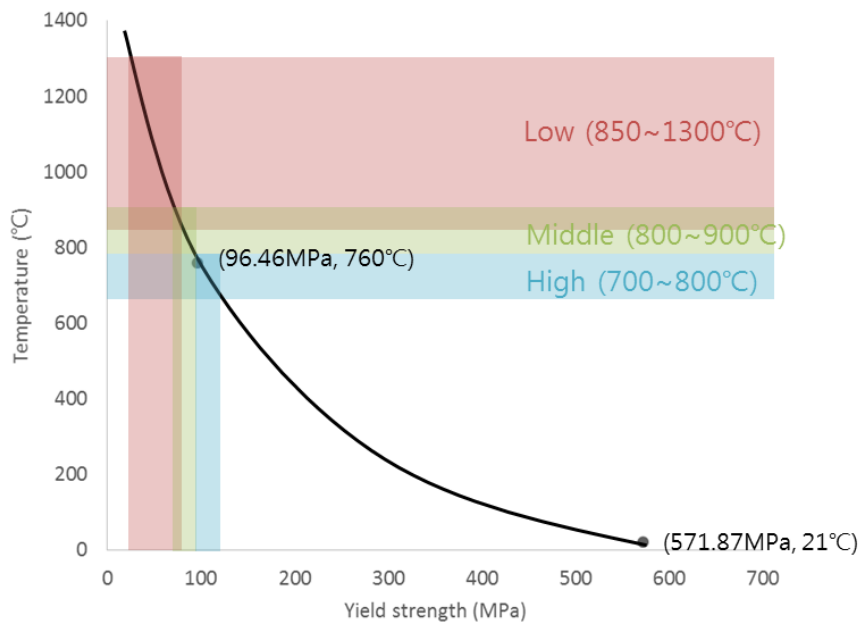


Fig. 4- 18 Schematic diagram of temperature and yield strength by lance region.

4. 3. Summary

Lance fracture occurs during processing. Halting processing results in loss of efficiency. During processing, lances undergo temperature variations between 800-1300 degrees. Temperature decreases during ore injection, and increases when ore injection is completed. Heat flux and ore thermal absorption applied to calculations. Lance temperature increase-decrease trends found to be in good agreement with experiments. FFT analysis revealed matte and slag splashing to lance causes lance temperature variation. Depending on injection conditions, lance experiences temperature differences between inner and outer surfaces, as well as lower, mid and upper regions. This can impose thermal stress on the lance. Also, thermal stripping arises from fluctuation at high temperature. Lance undergoes thermal stress exceeding yield stress during processing. The lower region of the lance is most susceptible.

Chapter 5. Lance fracture surface analysis

5. 1. Introduction

The present study with temperature measurement and numerical simulation revealed that the lances in the smelting furnace of Mitsubishi process are exposed to very severe conditions such as high temperature, repeated large temperature change, large temperature gradient across the radius directions and cyclic change of thermal stress. Especially, the lance may undergoes the properties change because the lance temperature changes from 800°C to 1300°C. Therefore, it needs to understand high-temperature properties of the lance material. Since the composition of lance, which contains at least 26% Cr, is similar with 446 types stainless steel [55], then 446 types stainless steel is referred as follows.

First, the maximum service temperature in air for 446 types stainless steel is 1100°C [56]. Cyclic oxidation studies conducted by Grodner also revealed that Type 446 was the best performer in the 400 series stainless steels, followed by Types 430, 416 and 410 (Fig. 5-1) [57]. In cyclic oxidation tests performed by Kado et al. in still air at 1000°C for 400 cyclic (30min. in the furnace and 30min. out of the furnace), alloys that performed well under these

conditions were Types 446 as illustrated in Fig. 5-2 (a). When cycled to 1200°C, all the alloys tested except F-1 alloy (Fe-15Cr-4Al) suffered severe oxidation attack. (Fig. 5-2 (b)) The data also illustrate that for temperatures as high as 1200°C, Cr₂O₃ oxide scales can no longer provide adequate oxidation resistance [58].

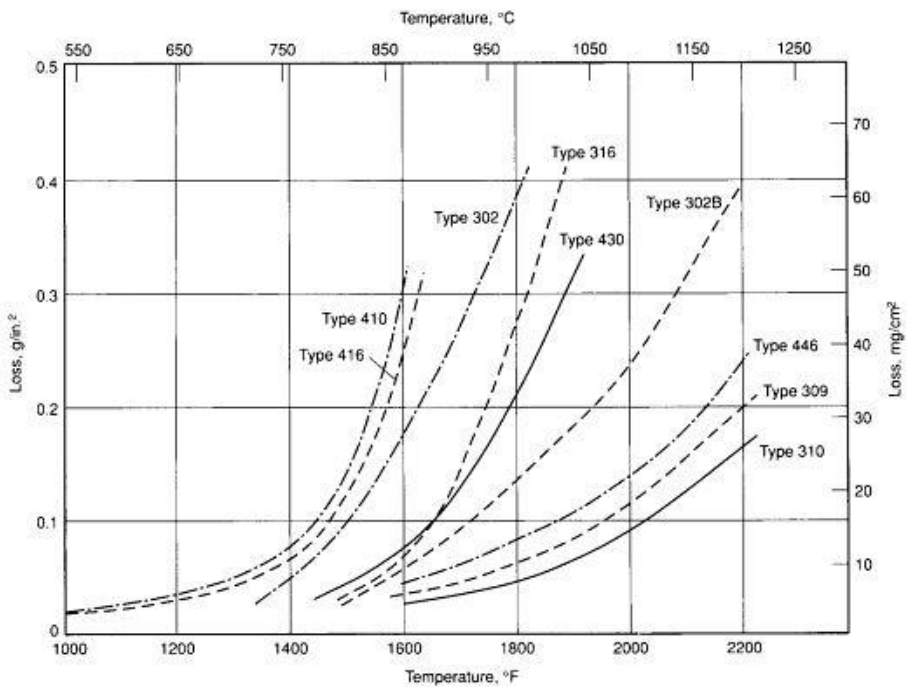
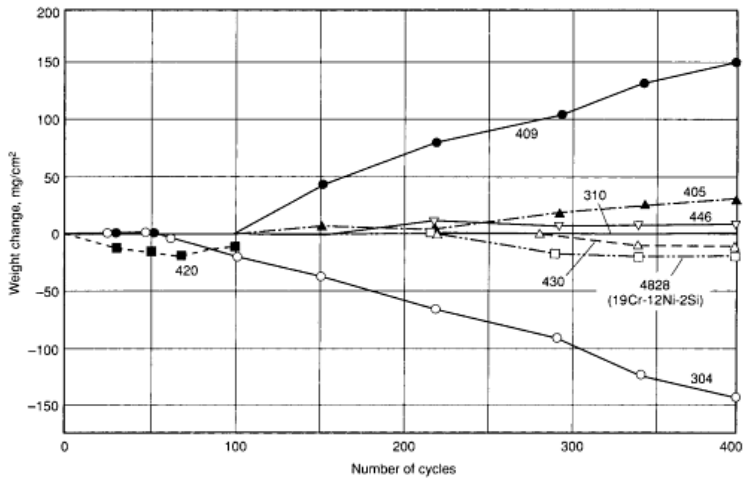
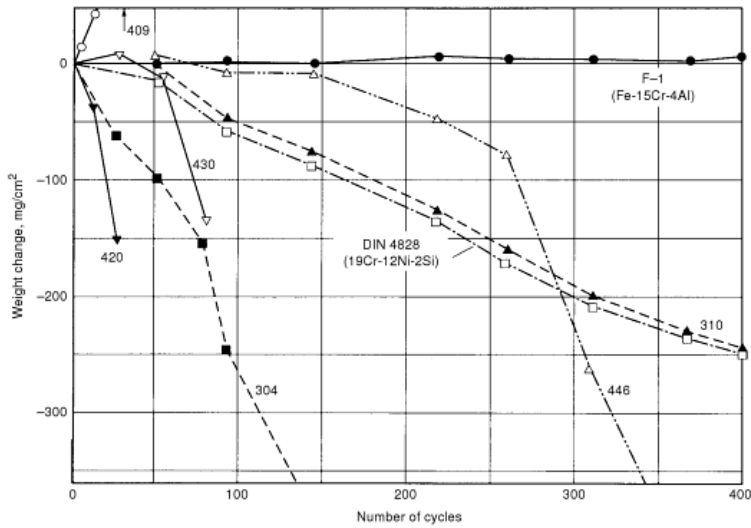


Fig. 5- 1 Oxidation resistance of several stainless steels as a function of temperature [57].



(a)



(b)

Fig. 5- 2 Cyclic oxidation resistance of several ferritic and austenitic stainless steels in still air at (a) 1000°C and (b) 1200°C for up to 400 cycles (30 min.

in furnace and 30 min. out of furnace) [58].

Second, when the service temperature is above 650°C, ferritic stainless steels, which have a body-centered cubic (BCC) crystal structure, drastically lose their elevated-temperature strength (both tensile and creep-rupture strength). As a result, the application of ferritic stainless steels becomes limited at higher temperatures. At these temperatures, alloys with a face-centered cubic (FCC) crystal structure are preferred because of their higher creep-rupture strength. Nickel is added to Fe-Cr steels to stabilize the austenitic structure. The austenitic structure is inherently stronger and more creep resistance than the ferritic structure [59]. Third, the lance temperature during processing is in the sigma-phase embrittlement temperature region that high Cr stainless steels are exposed to temperature between 600°C and 1000°C, chromium nitrides precipitation, chromium carbides precipitation. It leads to loss in both corrosion resistance and fracture toughness resulting in cracking [60-63].

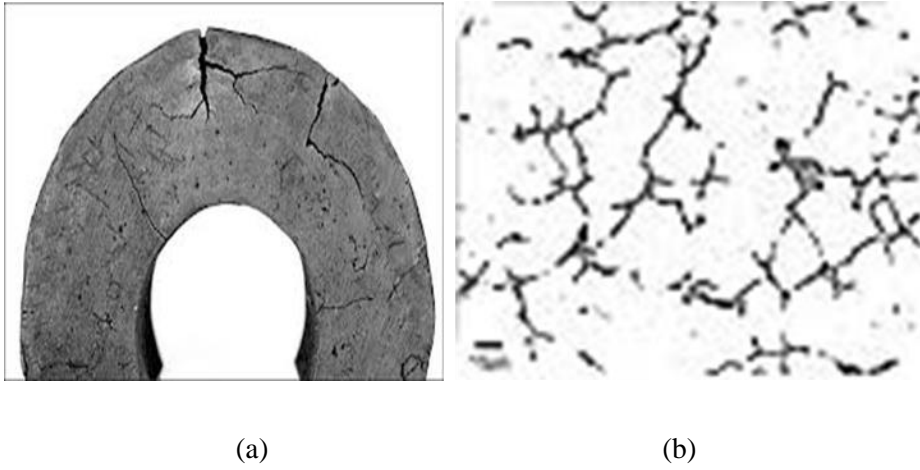


Fig. 5- 3 (a) Section of a cast HH(25%Cr, 12%Ni) STS (b) Sigma phase (dark) precipitated from excessive ferrite in the cast HH STS [62].

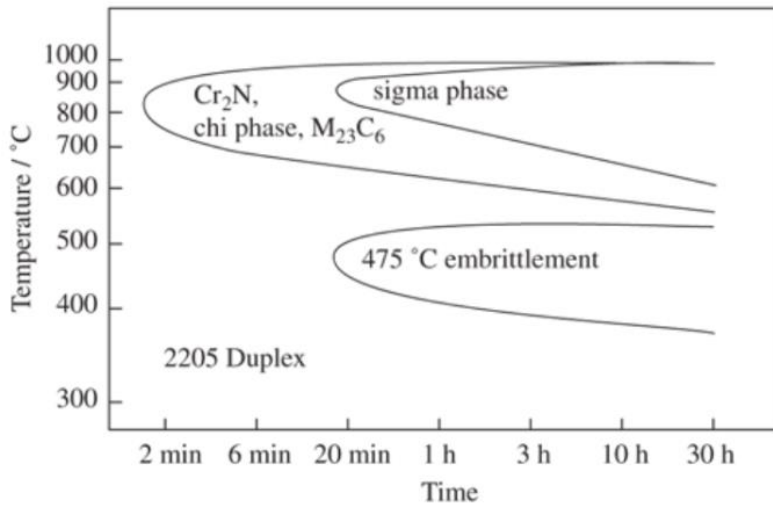


Fig. 5- 4 Sigma-phase embrittlement [63].

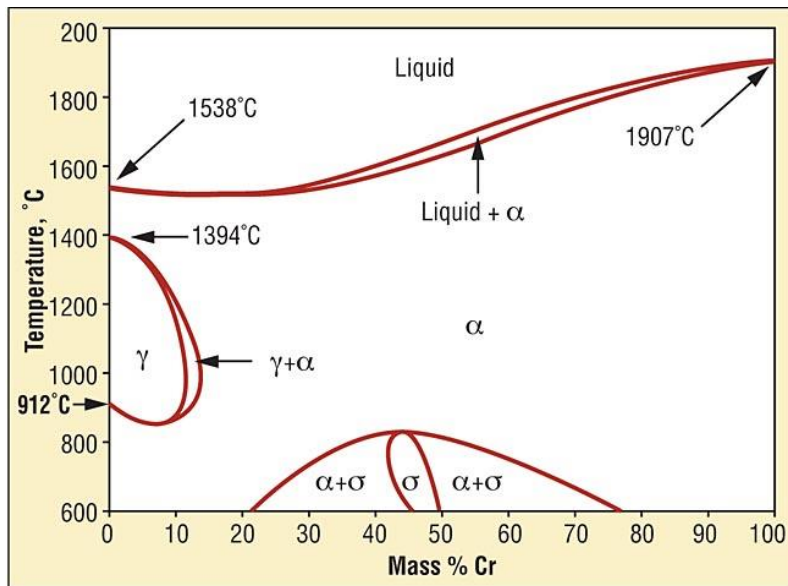


Fig. 5- 5 Iron-Chromium phase diagram [63].

Fourth, the lance temperature during processing is in the grain boundary sensitization region that refers to the precipitation of carbides at grain boundaries in a stainless steel, causing the steel to be susceptible to intergranular corrosion or intergranular stress corrosion cracking. Certain alloys when exposed to a temperature characterized as a sensitizing temperature become particularly susceptible to intergranular corrosion. In a corrosive atmosphere, the grain interfaces of these sensitized alloys become very reactive and intergranular corrosion results. This is characterized by a localized attack

at and adjacent to grain boundaries with relatively little corrosion of the grains themselves. The alloy disintegrates (grains fall out) and/or loses its strength. Cr-Mn and Cr-Mn-Ni steels are also susceptible to intergranular corrosion following sensitization in the temperature range of 420°-850 °C. In the case of the austenitic stainless steels, when these steels are sensitized by being heated in the temperature range of about 520° to 800 °C, depletion of chromium in the grain boundary region occurs, resulting in susceptibility to intergranular corrosion [64-65]. Fifth, the lance is likely to be vulnerable to hot shortness because the S furnace inside is high acid atmosphere. Therefore, the high temperature problem, hot shortness (red-short or sulfur embrittlement) which occurs in above 1100°C will not occur in the lance tip height 1500mm. The hot shortness is a tendency for some alloys to separate along grain boundaries when stressed or deformed at temperatures near the melting point [66]. The sulfur contained in steel alloy generally combined with Mn to form MnS. However, when the S content is large or the Mn content is low in the steel, S will be combined with Fe to form FeS and distributes in the grain boundary. The FeS is susceptible to steel at the high temperature around FeS melting point, 1193°C [67-72].

The lance used in the Mitsubishi smelting furnace requires these properties: corrosion resistance, thermal fatigue resistance, high-temperature

strength, high-temperature wear resistance and good welding property for joining lance after fracture because of severe conditions inside the furnace. When the lance test was conducted by LS-Nikko Copper's research team in 2008, they understood that the process of lance fracture in the following steps: 1) lance temperature increases when feeding is stopped to fill feeding tank with ore 2) lance cooled by ore during feeding 3) thermal stress caused by temperature gradient between inner and outer lance surface 4) lance fracture. Therefore, they concluded that the main mechanism of lance fracture is thermal fatigue fracture due to the thermal stress. So they chose the high-Cr ferritic stainless steel (446 SUS series) which has high thermal fatigue resistance and added N to the lance in order to increase the thermal fatigue life at a high temperature. The results they obtained from the test are as follows. At first, lance thickness measured at the direction of height and thickness and the results shows that difference between high and low height is very small. And the lance surface under the build-up (Build-up is a splashed matte attached on lance surface) was observed. As a result, there is no melting and corrosion evidence and no Cr in the build-up by EDS analysis. From these results, they concluded that melting and corrosion is not the cause of lance wearing. And in the observation of surface of fractured lance, they concluded that lance exterior is typical brittle fracture because of rough surface and lance interior is typical ductile fracture because of smooth surface.

However, there is a limit to predict the reason of lance fracture by only EDS analysis of build-up surface and eye observation. In addition, a detail microstructural analysis of the lance has not be conducted. Despite the lance which has a good thermal fatigue resistance is used now, the fracture of the lance is still taking place. This means that there are other causes affecting the lance fracture. And a lot of time is needed to fracture the material to be thermal fatigue normally. Therefore, the purpose of this test is to figure out other causes of lance fracture through observing microstructure of the lance fracture surface using various analysis tools.

5. 2. Experimental method

Before-using lance and fractured lance were obtained by LS-Nikko Copper. Fractured-lance tip is shown in Fig. 5-6. The dust attached to lance interior is called build-up and removed to analyze. Analysis was conducted by SEM (Scanning Electron Microscope) to observe the cross-section of the lance and EDS (Energy-dispersive X-ray Spectroscopy) to figure out the composition of exterior, body and interior lance. And EBSD (Electron Backscatter Diffraction) analysis was conducted to understand the structure, crystal orientation and phase of fractured lance. Typically EBSD is used to explore microstructures, reveal texture, defects, grain morphology and deformation [73-75]. And AES (Auger electron spectroscopy) is used in order to analyze the composition of the lance fractured surface. AES is an analytical technique that uses a primary electron beam to probe the surface of a solid material [76-78].

Planes near the fractured surface were cut for analysis. The Fig. 5-8 shows the samples for SEM, EDS, EBSD and AES analysis and cut areas. Samples of rectangular shape were cut to see a cross-section for SEM and samples of cylindrical shape were cut for AES. AES samples were grind out for cut easily during analysis.



Fig. 5- 6 Lance fracture surface.

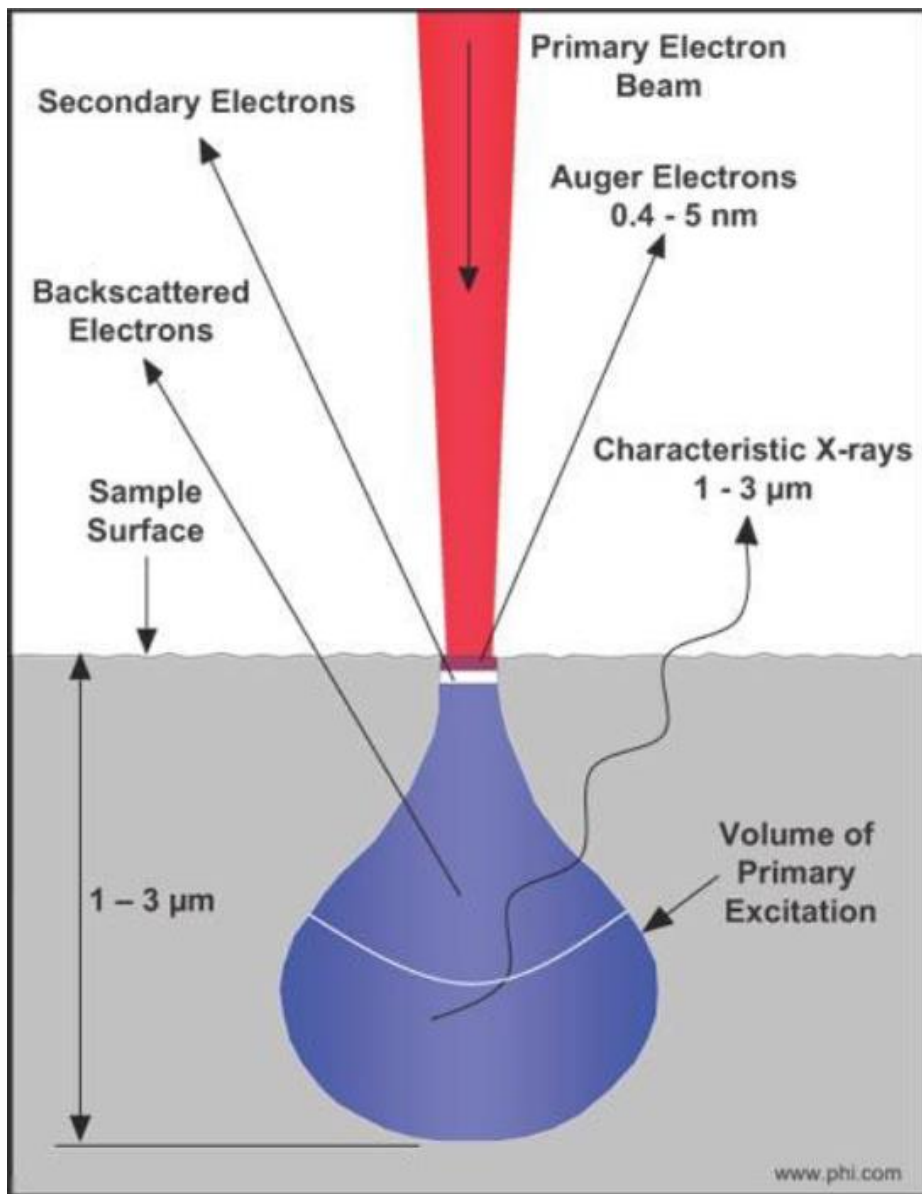
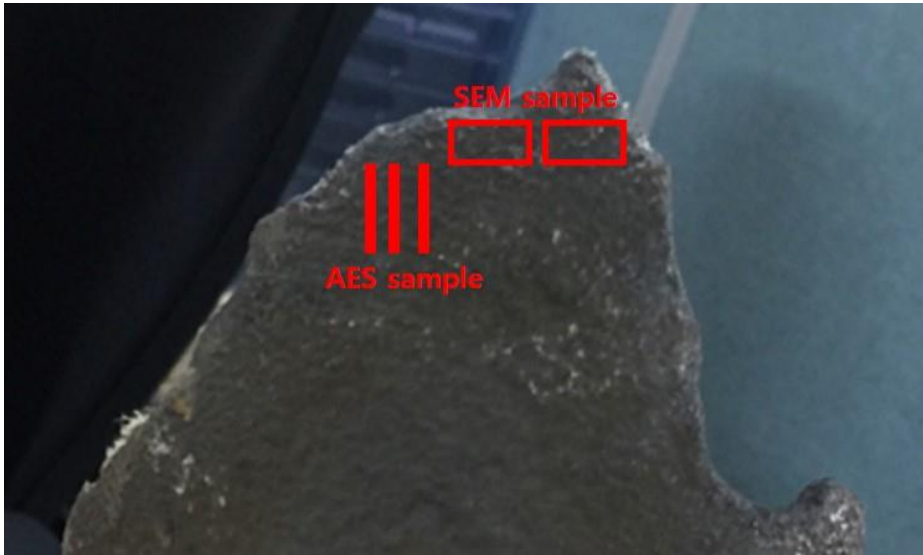
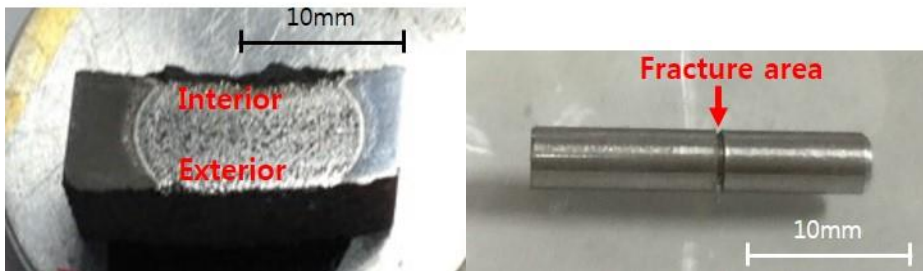


Fig. 5- 7 Electron Beam – Sample interaction.



(a)



(b)

(c)

Fig. 5- 8 (a) Sampling area for SEM & AES analysis.

(b) Sample for SEM, EDS and EBSD analysis.

(c) Sample for AES analysis including fracture area.

5. 3. Result and discussion

5.3.1 Analysis of the before-using lance

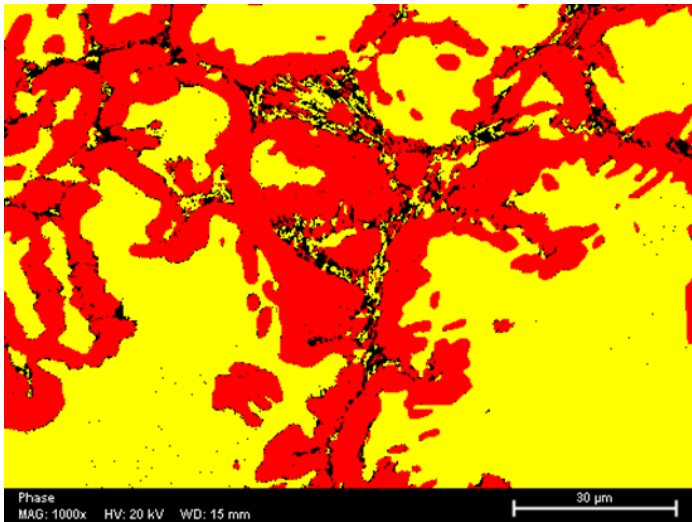
The composition of the before-using lance was analyzed using EDS and C/S analysis (Carbon/Sulphur Analyzer) [79]. The composition of the before-suing lance was compared with the A297HC in Table 2-5. The result shows that Si percentage of the before-using lance is the half of the A297HC and other elements' composition ration is similar.

Table 2- 5 Composition of A297HC [49]

	C	Mn	Si	P	S	Mo	Cr	Ni	Fe
A297HC (wt%)	0. 5	1	2	0.04	0.0 4	0.5	26-30	4	Bal.
Before- using lance (wt%)	0. 45 89	0.91 56	0.86 62	0	0.0 07 4	0.34 49	27.27 65	4.31 17	65.8 189

And next, phase and crystal orientation of the before-using lance are analyzed

using EBSD. The Fig. 5-9 shows that the before-using lance is a duplex stainless steel, in which the BCC ferrite phase and FCC austenite phase are mixed. It can be expected that the material was heat-treated above the austenite transform temperature before delivery.



Red :
Austenite, fcc
Yellow :
Ferrite, bcc

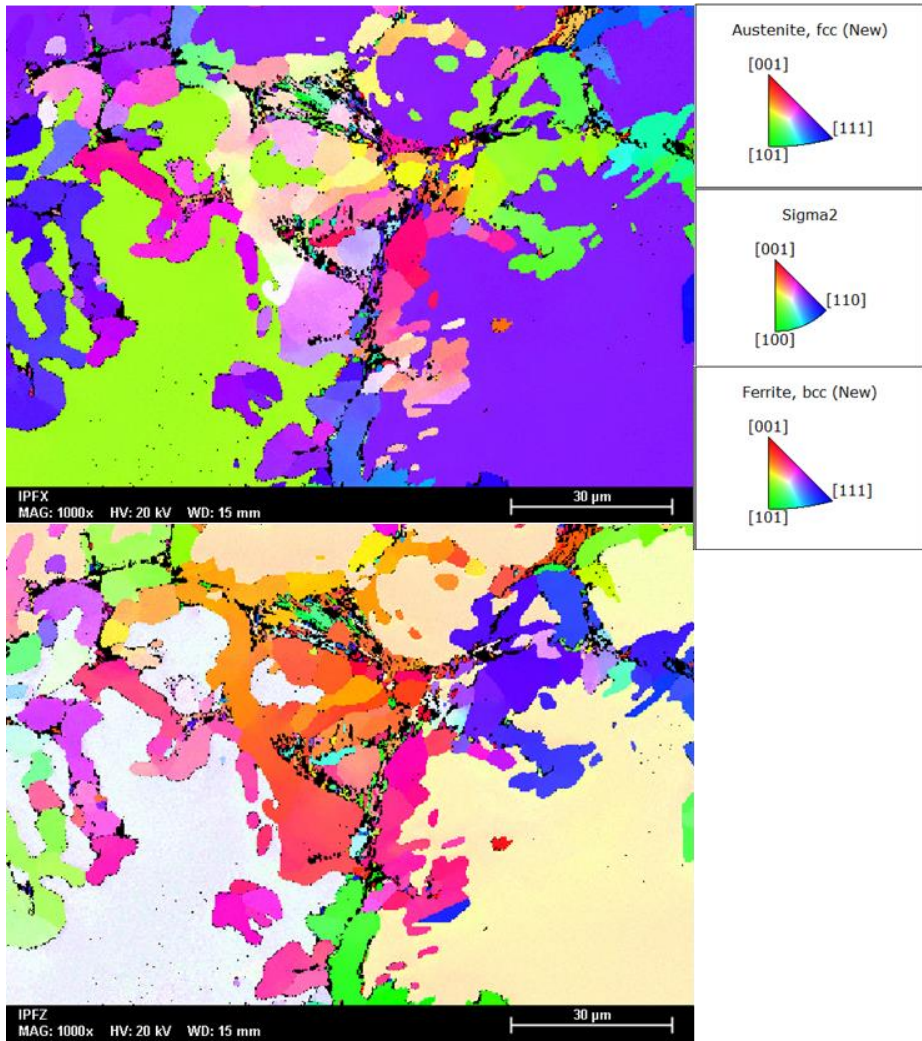
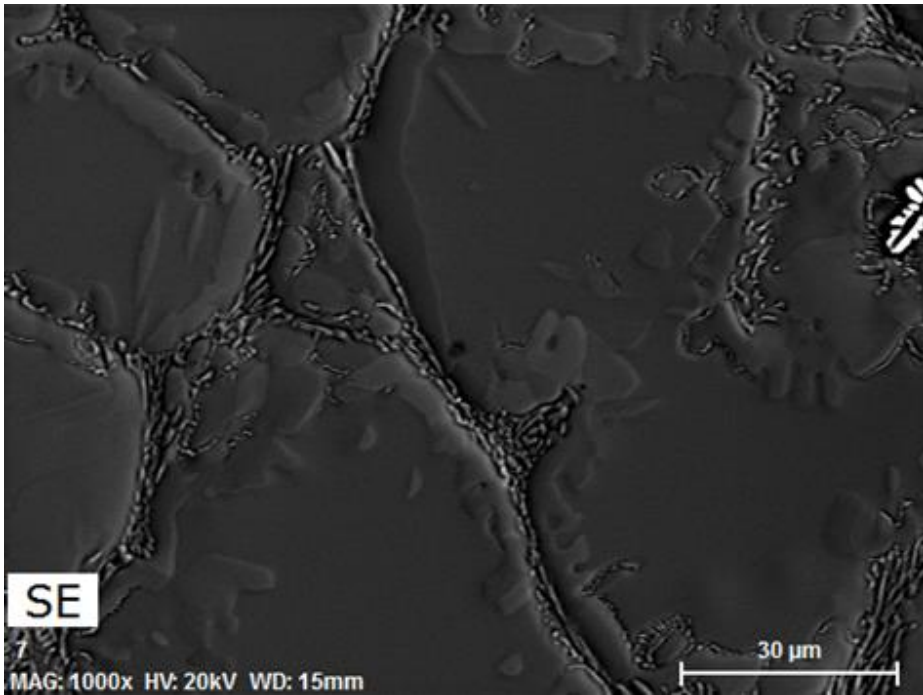


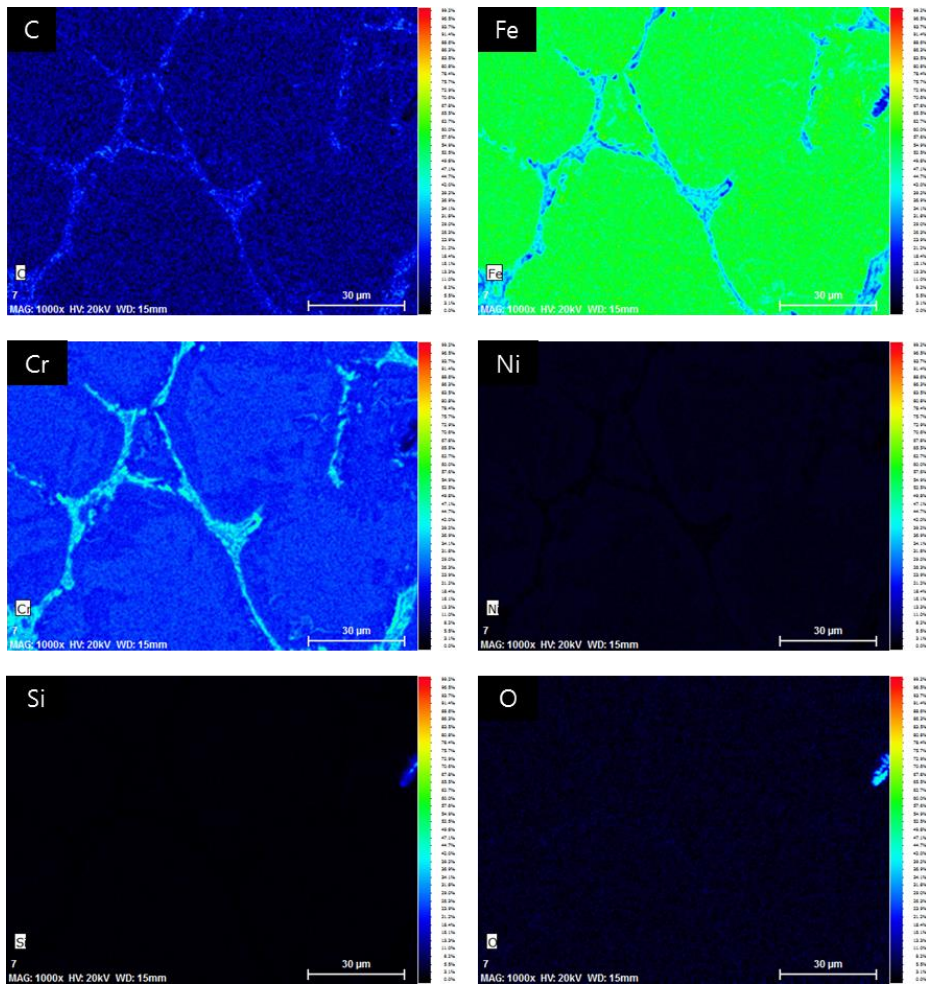
Fig. 5- 9 EBSD analysis results of the before-using lance.

(x1000, electrolytic polished)

The EDS quantitative analysis mapping images of the before-using lance are shown in Fig. 5-10. The Fig. 5-10 shows that the Cr and Fe carbides formed along the grain boundaries. Also, Cr content in the austenite area around the grain boundaries is smaller than the grain interior. Although the quantitative analysis of the carbon of the EDS is not credible, but it can be expected to Cr depleted in the grain boundary according to carbide formed.



(a)



(b)

Fig. 5- 10 (a) SEM image of before-using lance. (b) Images of EDS quantitative mapping. (Before-using lance)

In summary, when the temperature change of the duplex stainless steel lance is high, residual thermal stress in the lance will be accumulated because of the difference of the thermal expansion coefficient between FCC austenite and BCC ferrite. And it was found that carbides formed along the grain boundaries because of the high carbon content in the grain and Cr around grain boundaries depleted. As a result, there are problems to cause phase transformation around grain boundary. The Fig. 5-11 shows the range of mean thermal expansion coefficient of various steel phases [80].

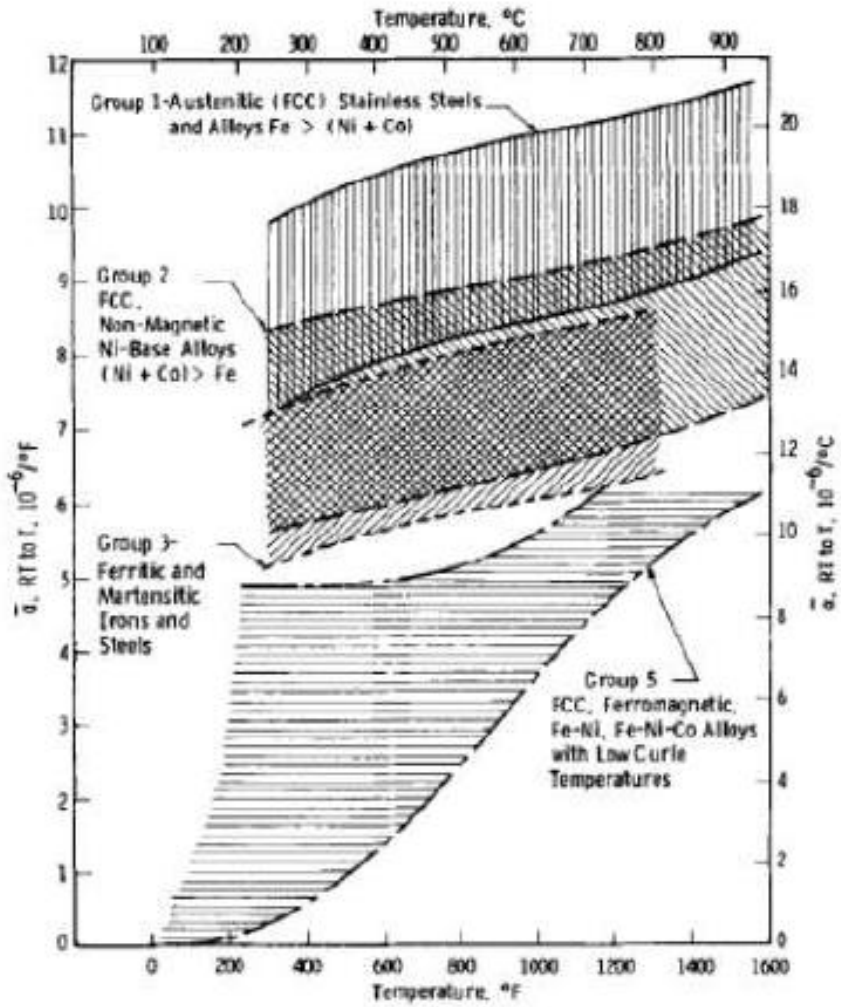
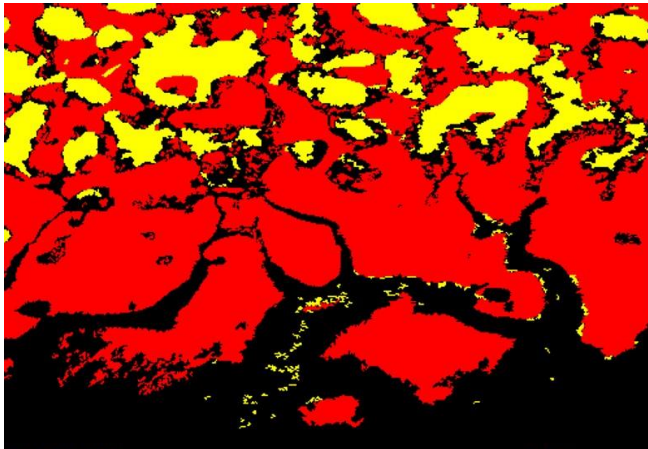


Fig. 5- 11 Range of mean thermal expansion coefficient from room temperature to T of austenitic stainless steels, FCC nonmagnetic Ni-base alloys, ferritic and martensitic iron and steels, and FCC ferromagnetic Fe-Ni and Fe-Ni-Co alloys.

5.3.2 Analysis of the fractured lance

The microstructure analysis was carried out for the fractured lance. EBSD analysis results of the fractured lance are shown in Fig. 5-12. From the EBSD results, the FCC austenite is in the lance exterior and the austenite and ferrite mixture (duplex stainless steel) is in the lance body. The ratio of austenite phase and ferrite phase was changed compared with the result of the before-using lance. Only austenite phase exist in the exterior surface area of the lance. And the reason of the duplex stainless steel formed in the lance body can be expected that the lance temperature changed from 800°C to 1300°C.

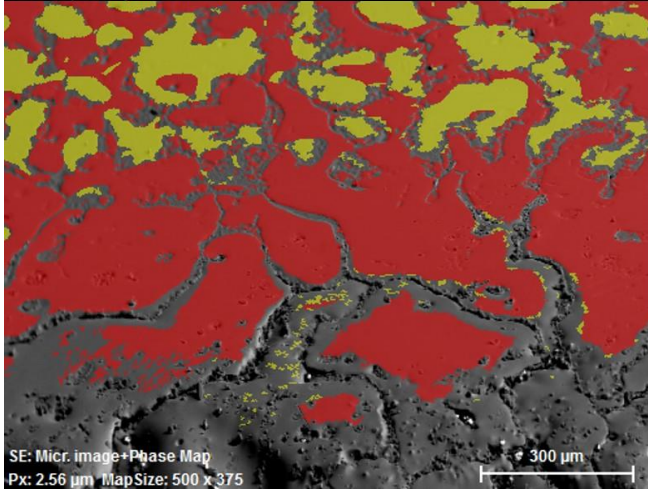


SE: Phase Map
Px: 2.56 μm MapSize: 500 x 375

300 μm

Red : Austenite FCC

Yellow : Ferrite BCC



SE: Micr. image+Phase Map
Px: 2.56 μm MapSize: 500 x 375

300 μm

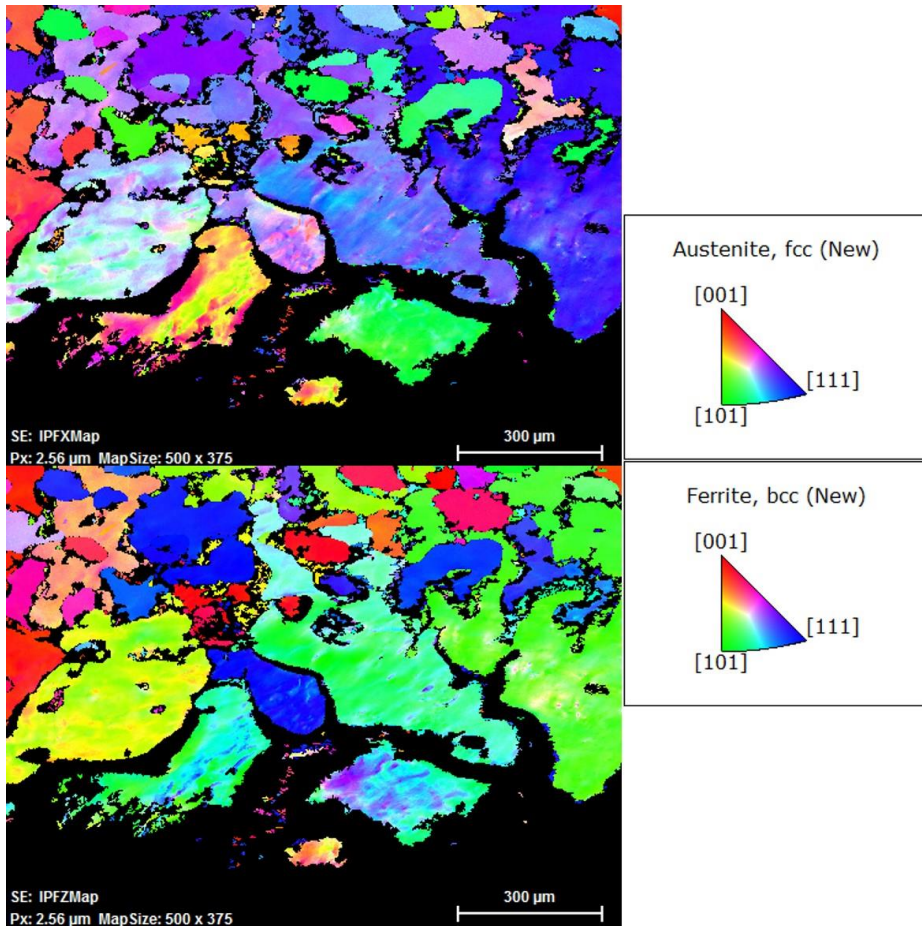


Fig. 5- 12 Results of EBSD analysis.

The EDS mapping analysis for the exterior surface of the fractured lance was conducted. Fig. 5-13 shows a SEM image near the lance exterior surface. (Figure bottom is an exterior surface) The grain boundaries near the

surface are divided. The number of the precipitates are found on the surface and grain boundaries. And the surface shapes of the lance body and lance surface are different. The compositions of both regions are expected to be different.

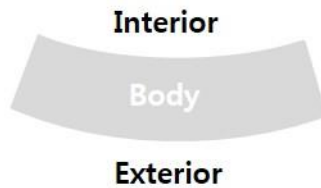
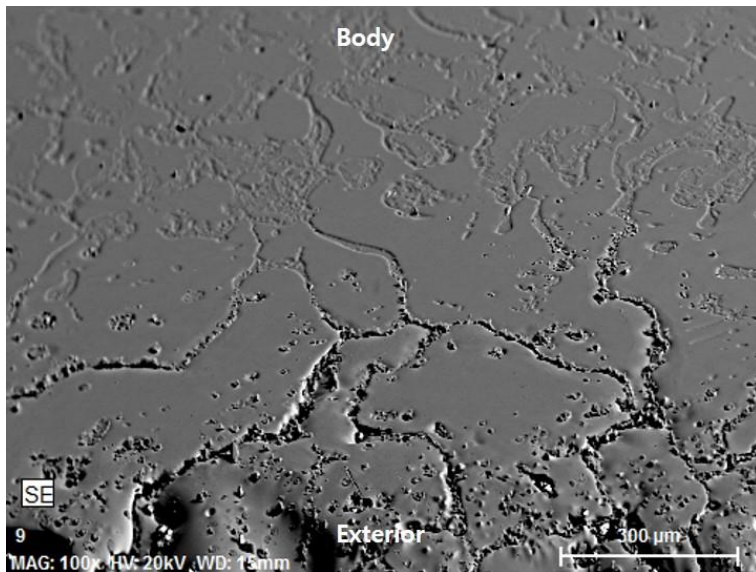


Fig. 5- 13 SEM image near the exterior surface.

(Bottom of the image is lance exterior surface.)

The EDS mapping images of the exterior lance are shown in Fig. 5-14 and the quantitative analysis mapping images of the exterior lance are shown in Fig. 5-15. In the Fig. 5-14 and 5-15, substance consisting of S, Si and O shown comes from the lance surface along the grain boundary. Also S is mainly present in the grain boundary at the lance surface, the body of which seems to be in the form of MnS. A lot of Cr is distributed in the grain boundary in the lance body but there is little at the surface. It can be seen that Cr depleted at the lance surface. In addition, it is expected that only austenite is present at the lance exterior in Fig.5-12 due to the Cr depletion, which is stabilizing element of BCC ferrite. Cr normally volatiles at from 700 to 800 degrees, the Cr depletion may deteriorate corrosion resistance of the lance surface. Therefore, S, Si and O could penetrate into grain boundary at the lance exterior instead of Cr. On the other hand, a lot of Cu and Si are in the deplete part and it can be expected coming from splashed matte and slag.

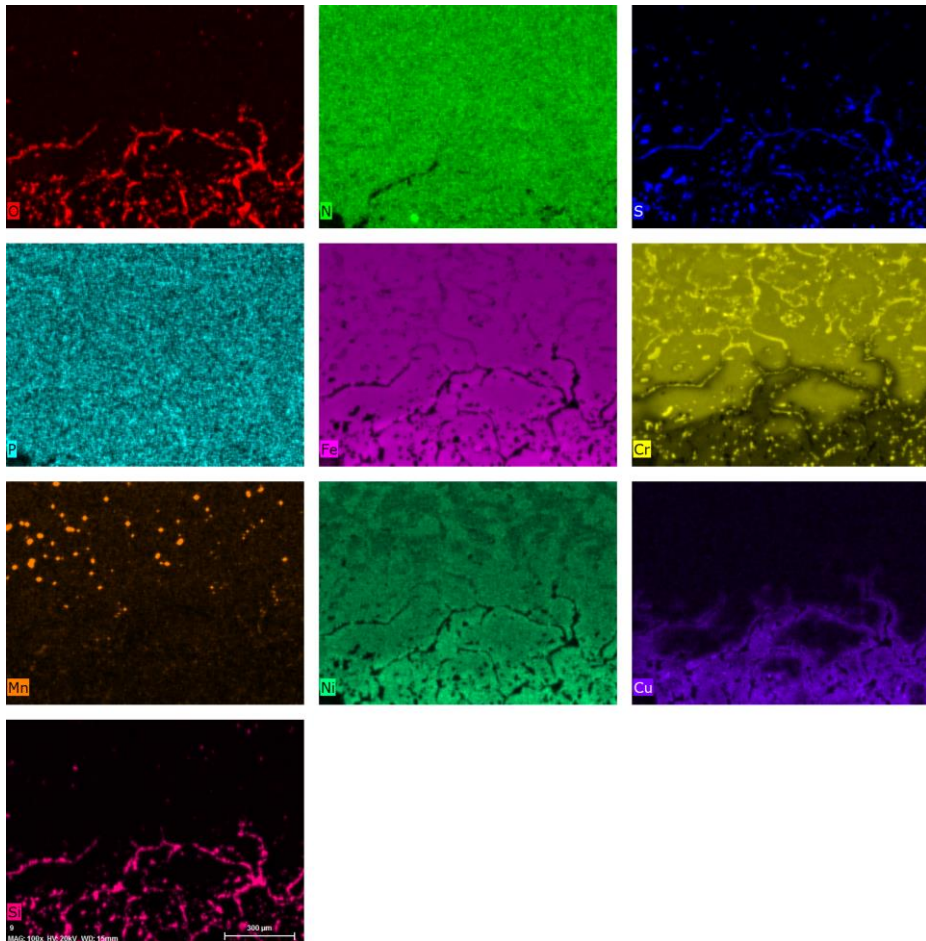
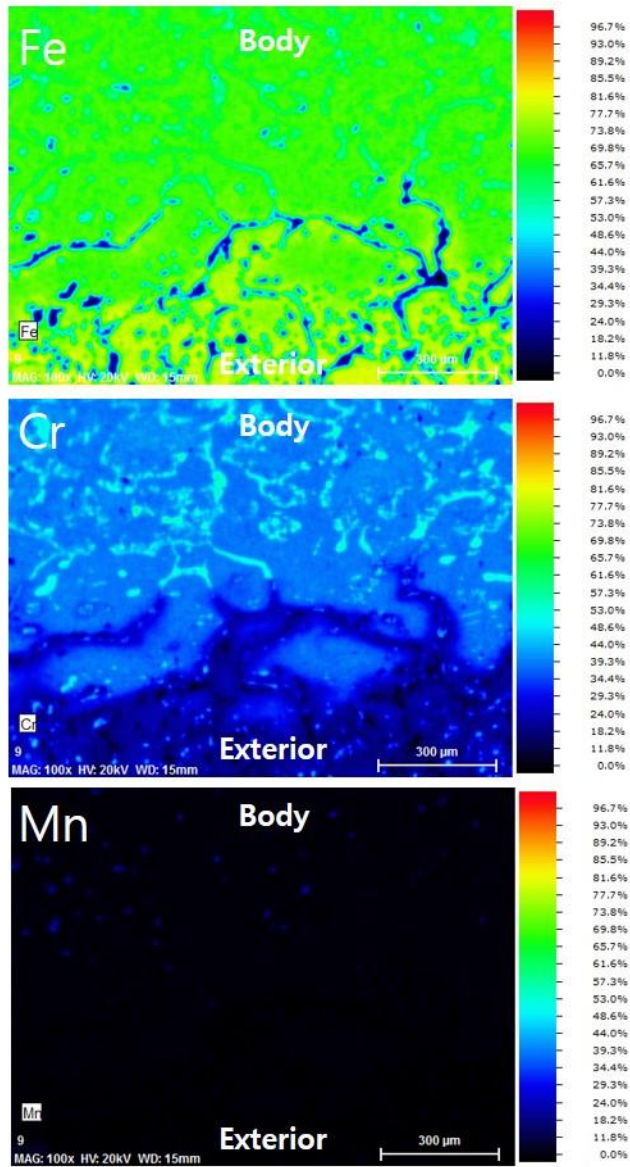
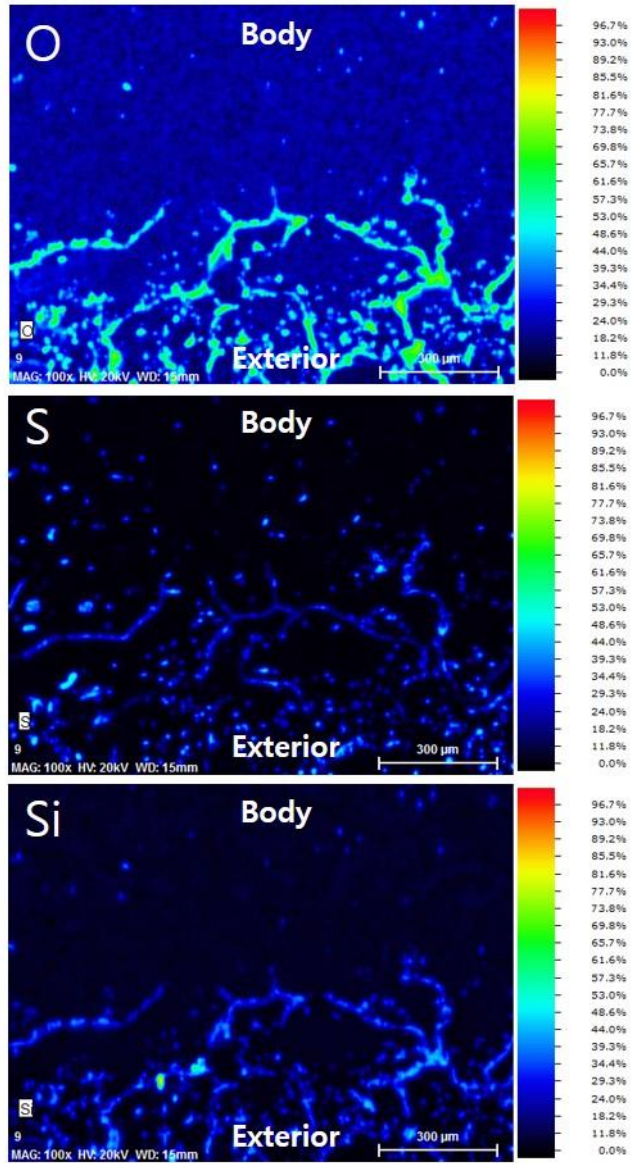


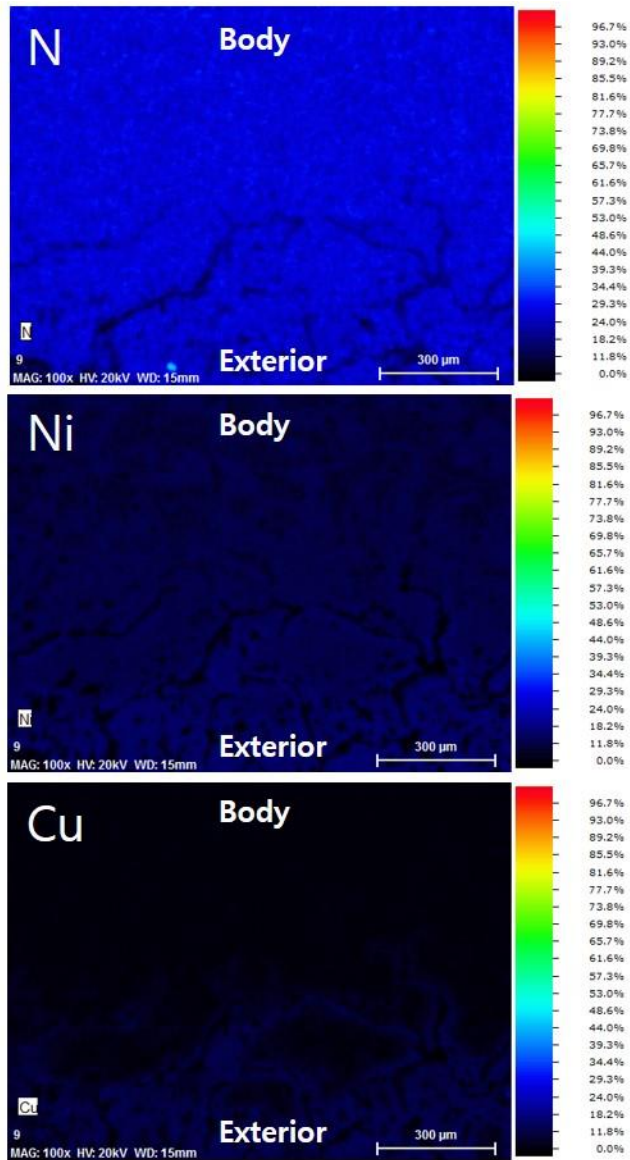
Fig. 5- 14 Images of EDS mapping. (O, N, S, P, Fe, Cr, Mn, Ni, Cu, Si)



(a) Images of quantitative mapping. Fe (upper), Cr (middle), Mn (lower).



(b) Images of quantitative mapping. O (upper), S (middle), Si (lower).



(c) Images of quantitative mapping. N (upper), Ni (middle), Cu (lower).

Fig. 5- 15 Quantitative mapping results.

Fig. 5-16 shows a SEM image near the lance interior. (Figure top is an interior surface) The surface shapes of the lance interior surface and exterior surface are nearly same.

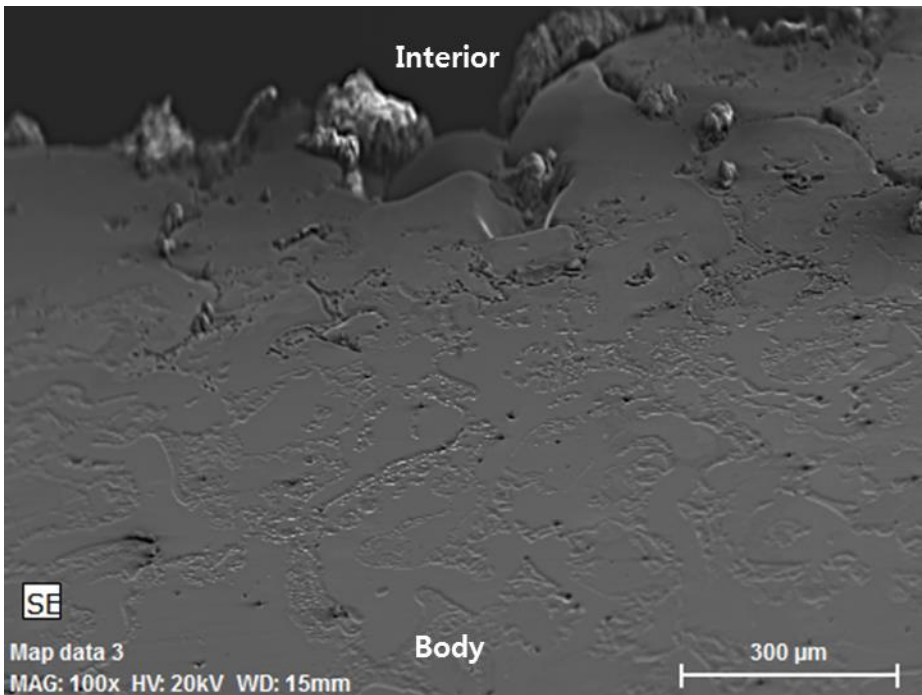
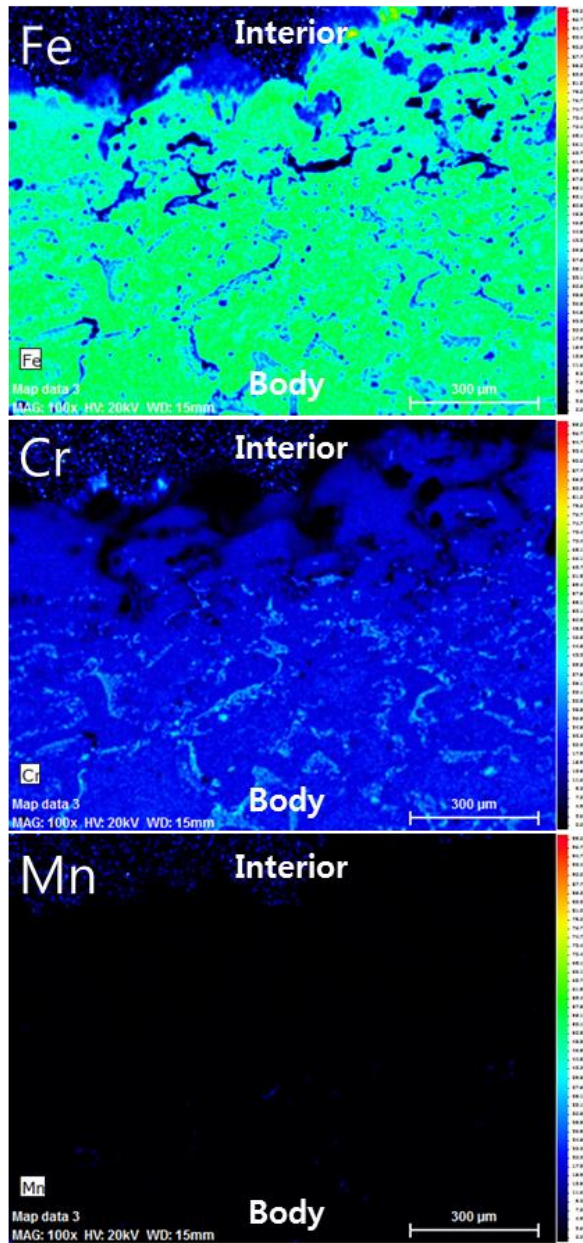


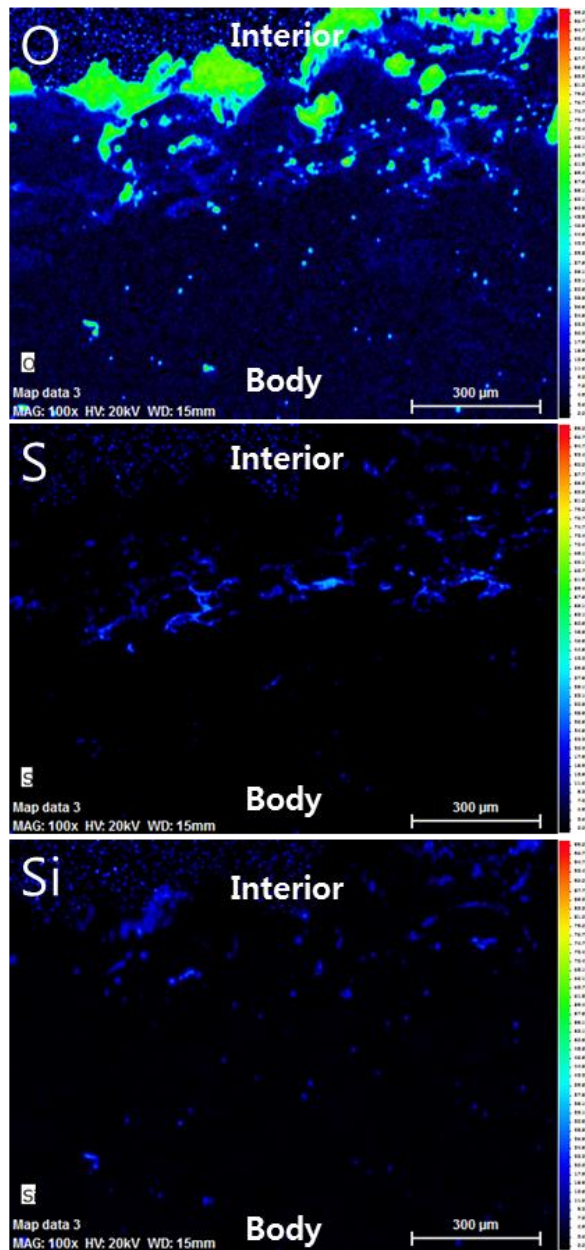
Fig. 5- 16 SEM image near the interior surface.

(Top of the image is lance interior surface)

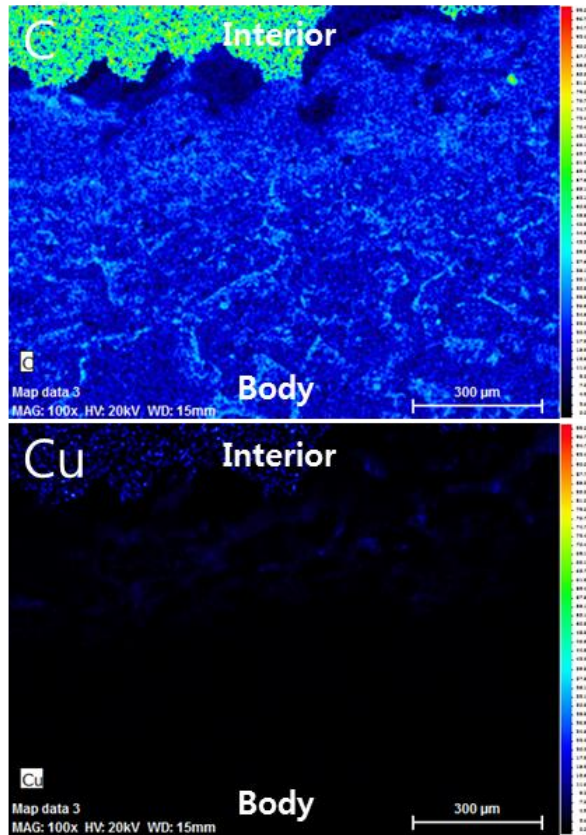
The EDS quantitative analysis mapping images of the lance interior surface are shown in Fig. 5-17. The lance exterior is exposed to the high sulfuric acid atmosphere in processing and affected by high temperature splashed matte and slag. On the other hand, the lance interior is exposed to injected ore and saturated oxygen. When the EDS mapping results of lance interior are compared with the lance interior, the Fe-based oxide was estimated to be formed in lance interior surface, especially sulfide was estimated to be formed. The lance interior and exterior were confirmed that the type of phases are different because of the different environment. On the other hand, Cr depletion phenomenon was the same.



(a) Images of quantitative mapping. Fe (upper), Cr (middle), Mn (lower).



(b) Images of quantitative mapping. O (upper), S (middle), Si (lower).



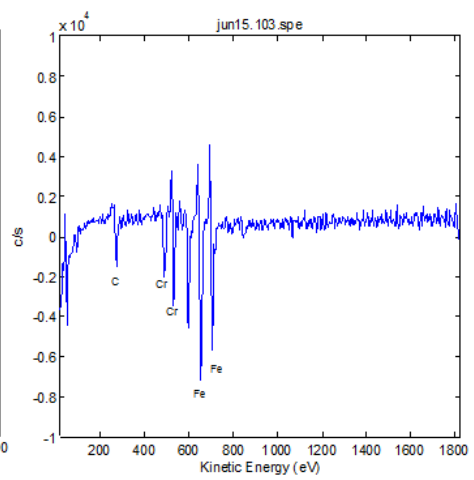
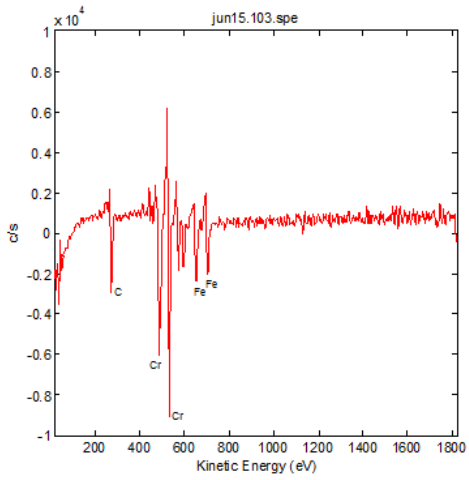
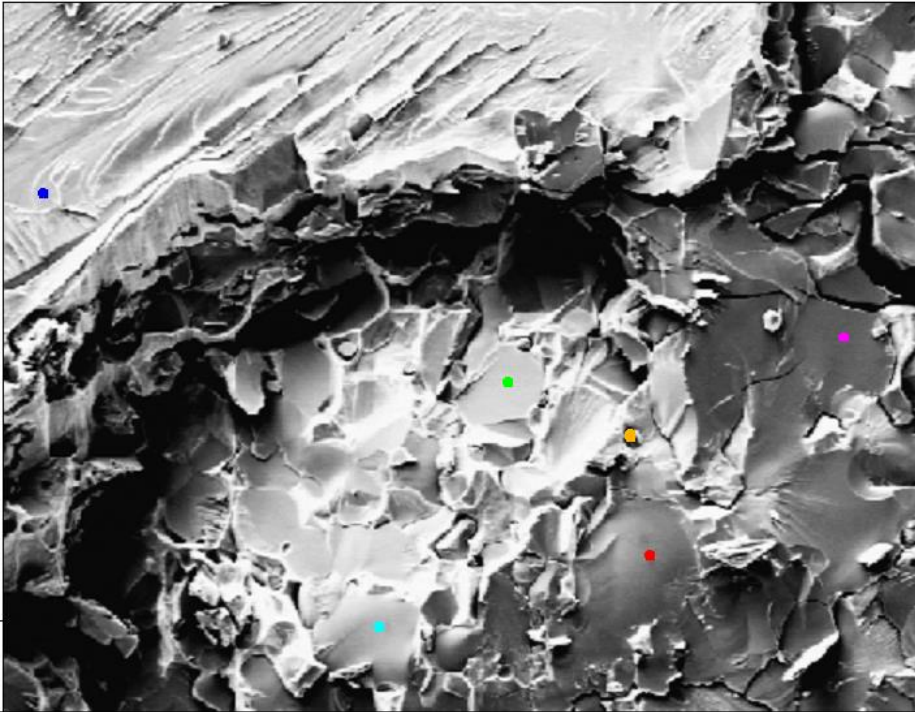
(c) Images of quantitative mapping. C (upper), Cu (lower).

Fig. 5- 17 EDS quantitative mapping results.

The evidence which can assist the above results is obtained from the AES analysis result. AES measurement sample is more close to the lance body than lance surface. The AES measurement results are show in Fig. 5-18 and Fig. 5-

19. At the fracture surface, inter-granular fracture and trans-granular fracture were mixed. So the reason of lance fracture does not figure out whether the inter-granular fracture or trans-granular fracture. When measuring the part of what is expected to grain boundary, Cr is present in most of the area on the grain boundary with Fe and C. On the other hand, S was found to be present with Mn and Cr. The Cr precipitated at the grain boundary and MnS locally present at the grain boundary are in good agreement with EDS mapping result. But the exact composition of Cr composite could not be known through these results.

x1000



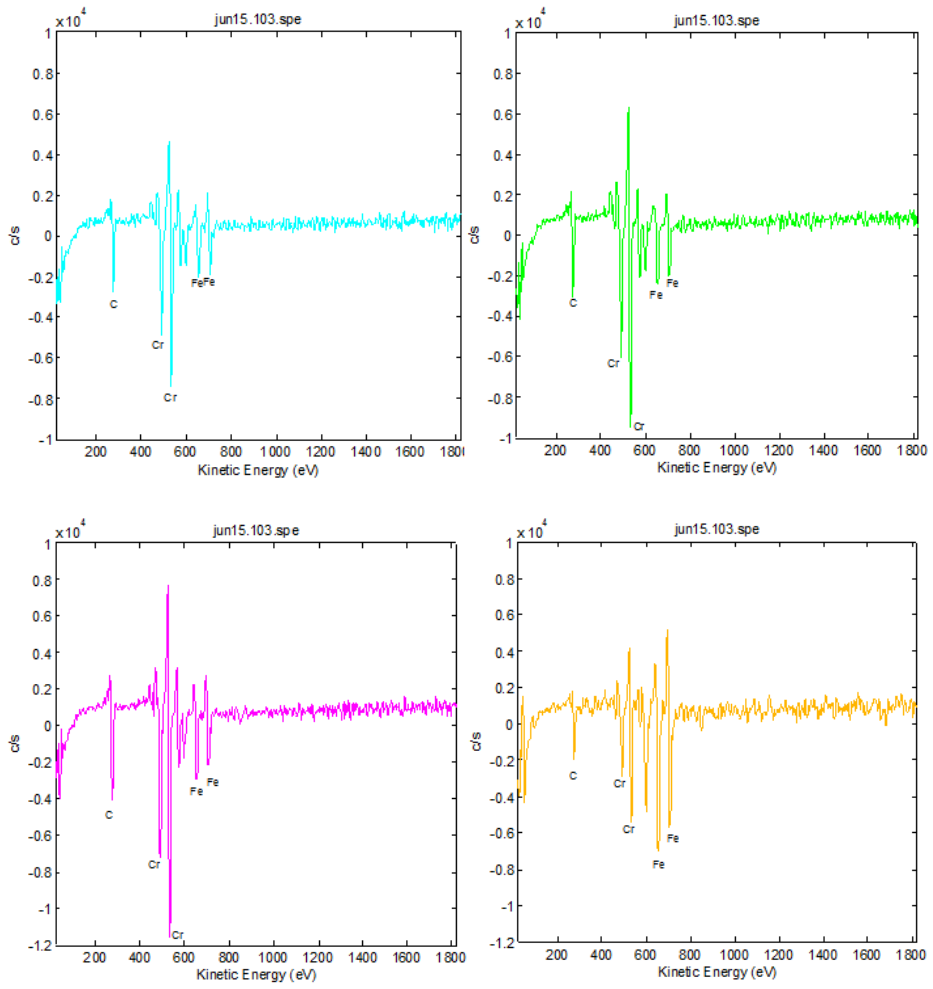
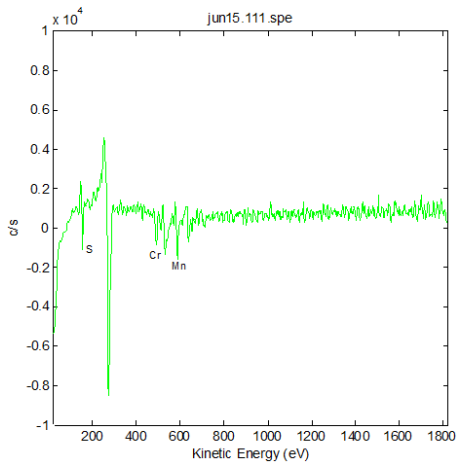
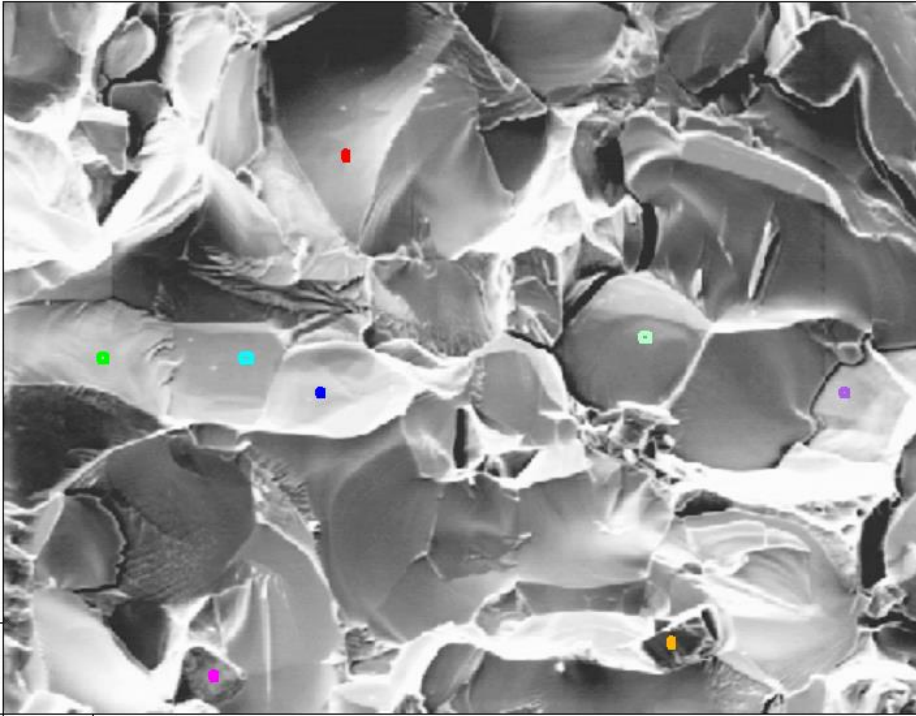


Fig. 5- 18 Cr peaks at the grain boundary in the lance body.

x2000



x2000

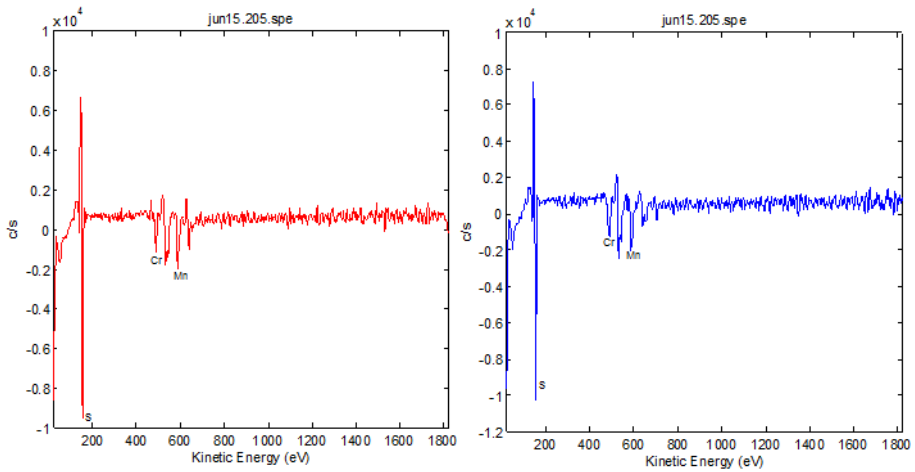
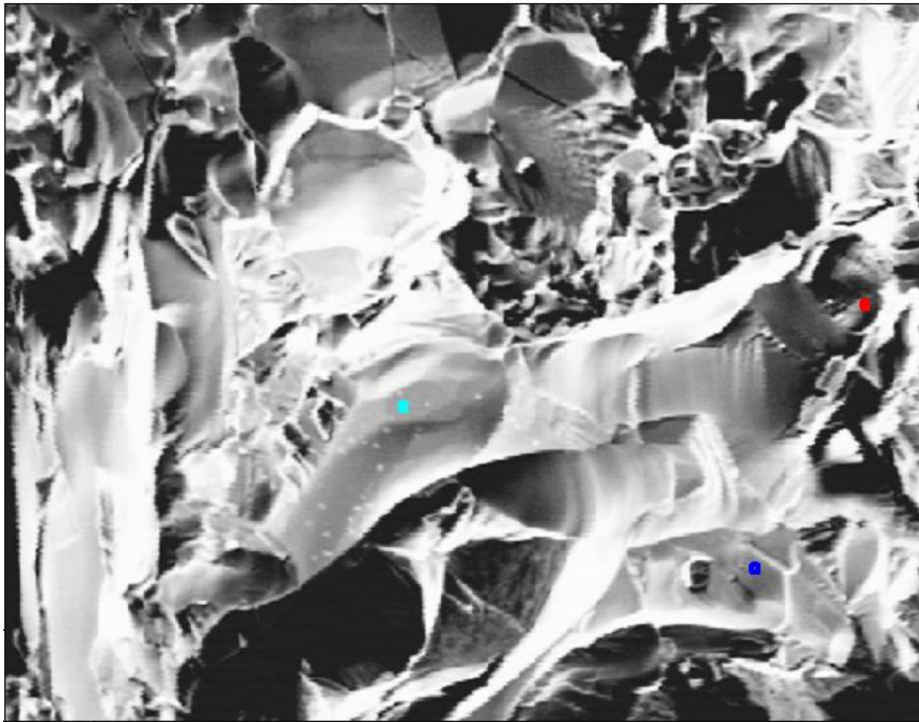


Fig. 5- 19 S peaks with Cr and Mn at the grain boundary in the lance body.

Thus, it is possible to expect the following lance fracture mechanisms through the lance microstructure analysis results. The lance is a high-Cr and a duplex stainless steel which the BCC ferrite and FCC austenite phase are mixed. The high-Cr stainless steel has a good thermal fatigue resistance, but Cr depleted at the lance surface (both interior and exterior) due to the high temperature and severe sulfuric atmosphere in the furnace which weakens the corrosion resistance of lance surface. Although the cause of Cr depletion is still unknown but matte and slag splashing may affected on Cr depletion. Also, as S, Si and O penetrated into the grain boundary and segregated, lance surface would be weakened to crack. Since the surface of the lance becomes weaker, if severe low cycle thermal fatigue is applied to the lance according to the lance temperature changing between 800°C to 1300°C occurs during the process, it can be expected that lances crack starts at the lance surface. And crack propagation takes place quickly due to continuous thermal stress of the lance, and finally lance will be fracture. In addition, other factors, splashed matte or rapid injected ore may be expect to cause a rapid lance fracture. It can be seen that the high-Cr stainless steel lance for improving thermal fatigue resistance is not good because it could not prevent the Cr depletion. Therefore, in order to prevent the lance fracture, lower the lance temperature, reduce the lance temperature change range and a more stable lance composition to Cr depletion are needed.

5. 4. Summary

In this test, the microstructure of before-using lance and fractured lance surface are analyzed using SEM, EDS, EBSD and AES.

In the EBSD and EDS results, the before-using lance is a duplex stainless steel which the BCC ferrite phase and FCC austenite phase are mixed. Also, Cr content in the austenite area around the grain boundaries is smaller than the grain interior.

In the SEM results of fractured lance, the number of the precipitates are found on the surface and grain boundaries. And the surface shapes of the lance body and lance surface are different. In the EDS results, substance consisting of S, Si and O shown comes from the lance surface along the grain boundary. A lot of Cr is distributed in the grain boundary in the lance body but there is little at the surface. From the EBSD results, the FCC austenite is in the lance exterior and the austenite and ferrite mixture is in the lance body. In addition, it is expected that austenite steel is present at the lance exterior due to the Cr depletion. And from AES results, the Cr precipitated at the grain boundary with Fe and C and MnS locally present at the grain boundary.

Therefore, Cr depleted at the lance exterior due to the high temperature and severe atmosphere, which weakens the corrosion resistance of lance surface. And S, Si and O penetrated into the grain boundary and segregated, and crack

propagation takes place quickly due to the continuous thermal stress of the lance. In addition, other factors, splashed melt or rapid injected ore may expect to cause a rapid lance fracture. It can be seen that the high-Cr stainless steel lance for improving thermal fatigue resistance is not good because the Cr depletion is not considered. Therefore, in order to prevent the lance fracture, lower the lance temperature, reduce the lance temperature change range and a more stable lance composition to Cr depletion are needed.

Chapter 6. Optimization of lance tip height & velocity

6. 1. Introduction

In the present study, lance temperature is high and lance tip undergoes high temperature change. If crack occur in the lance surface, these low cycle thermal fatigue can have a significant influence on the fracture of the lance. Therefore, we try to raise the height of the lance tip and numerical experiments were carried out. In this numerical test, I analyze changes in furnace depending on the change of lance tip height and velocity. Though raising lance tip height from the bath surface can resolve lance fracture problem, it can diminish melt mixing. Therefore selection of optimum lance height and flow velocity are the goals of this calculation.

6. 2. Calculation conditions

In Fig. 6-1, lance tip heights are set to be 700mm, 1600mm and 2400mm from the bath surface. And table 6-1 shows adjusted lance tip velocities, 50m/s, 125m/s, 200m/s, 250m/s and 300m/s. In addition, the condition of the initial set-up in 1997, 134m/s and 9 lances are also compared. As shown in Fig. 6-2, particles are injected from 30 to 45 seconds. This model does not consider the heat transfer and slag phase for computational efficiency.

I have investigated changes in the flow in the furnace include uptake outlet and lances. Difference between matte velocities, matte volume fractions, particle mass concentrations and particle residence times depending on lance tip height and velocity are shown at the planes. I also have observed matte average velocity, matte average turbulence kinetic energy, uptake outlet average matte volume fraction, depth of cavity and lance temperature difference between inner and outer surface depending on lance tip height and velocity over time. The measuring points are shown in figures 6-3, 6-4 and 6-5.

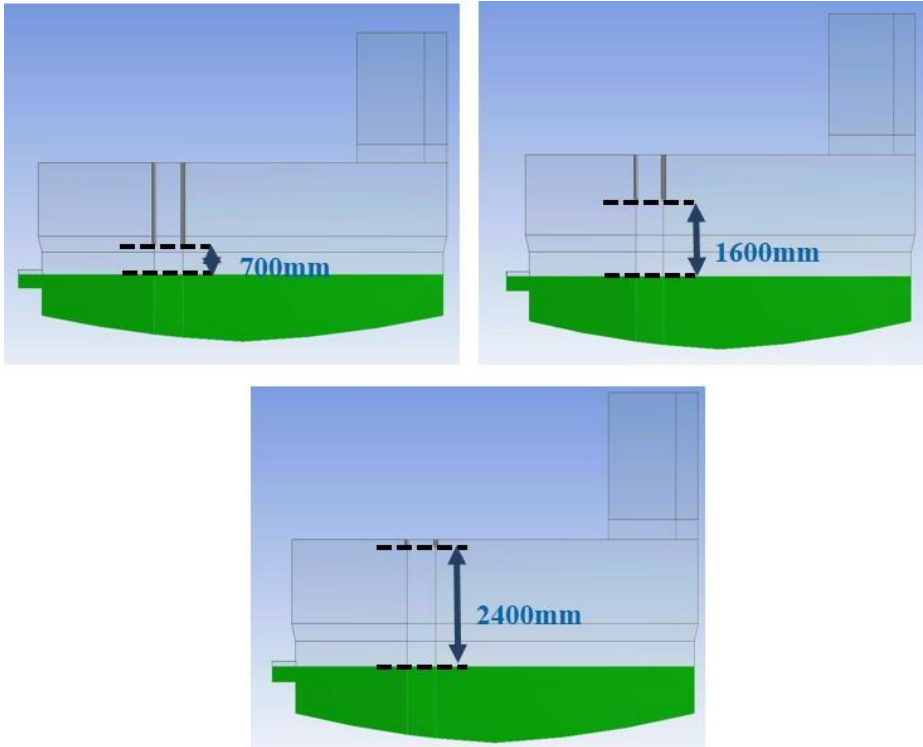


Fig. 6- 1 Three lance tip heights.

(700mm, 1600mm, 2400mm above the initial bath surface,

700mm is a present lance tip height)

Table 6- 1 Lance tip velocities.

700mm (50m/s, 125m/s, 134m/s), 1600mm (125m/s, 200m/s, 225m/s),
2400mm(125m/s, 200m/s. 300m/s).

125m/s is a present lance tip velocity and 134m/s is the lance tip velocity in
1997

Lance tip height	Tip velocity 1	Tip velocity 2	Tip velocity 3
700mm	125m/s (2015)	50m/s	134m/s (1997)
1600mm	125m/s	200m/s	225m/s
2400mm	125m/s	200m/s	300m/s

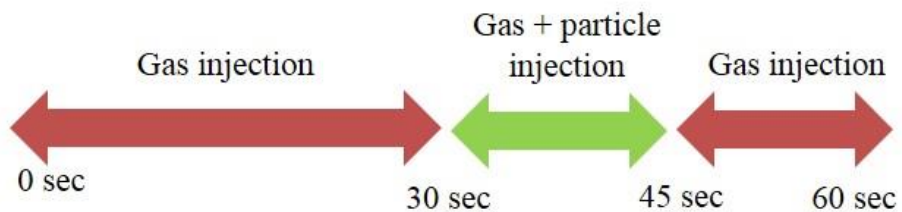


Fig. 6- 2 Gas and particle injection condition at the lance.

0-30s: gas injection / 30-45s: gas and particle injection / 45-60s: gas injection.

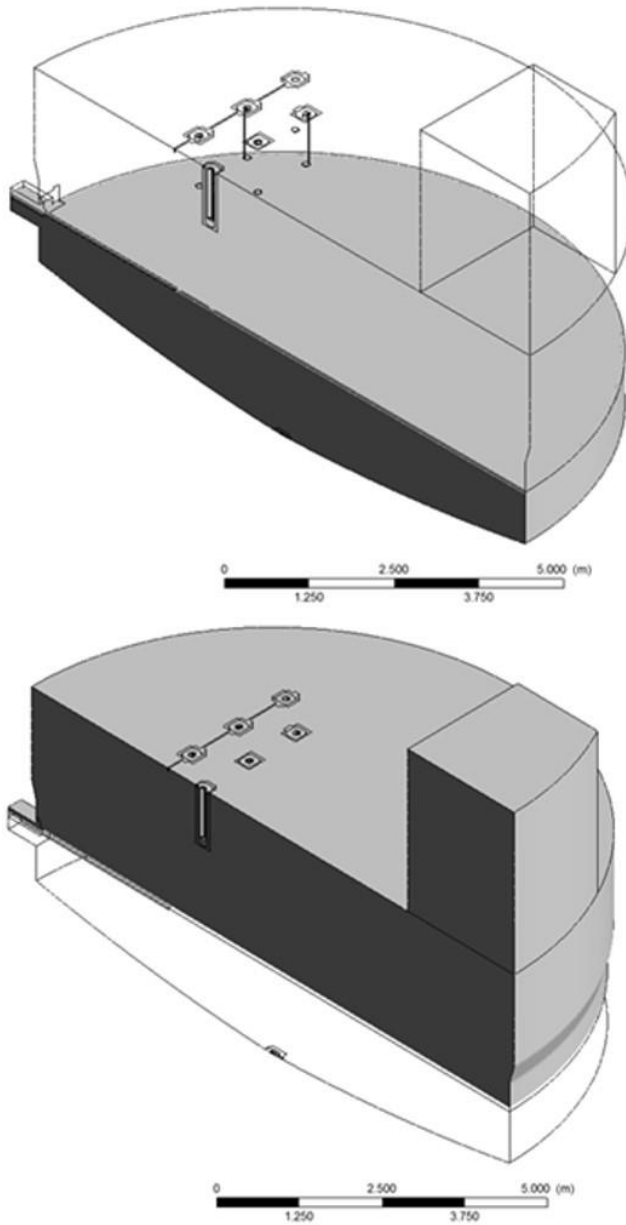


Fig. 6-3 Flow change measuring regions.

Matte (left) and gas (right).

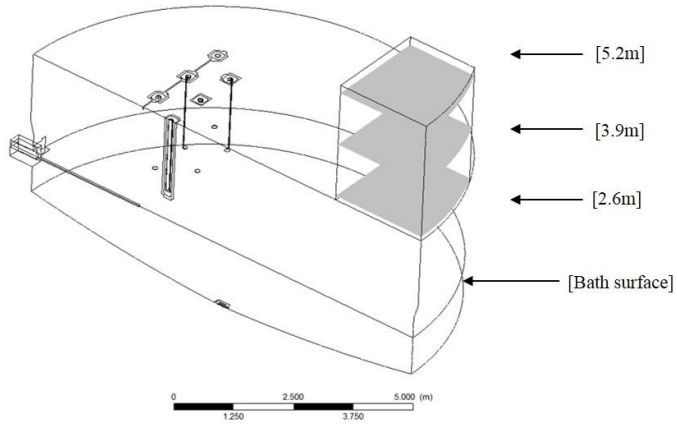


Fig. 6- 4 Outlet matte volume fraction measuring regions.

2.6m, 3.9m and 5.2m from the bath surface.

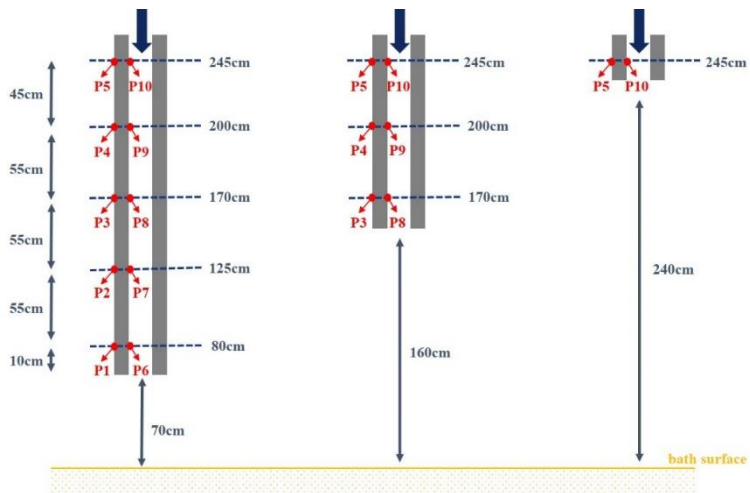


Fig. 6- 5 Lance tip matte volume fraction and lance temperature difference between inner & outer surface measuring points.

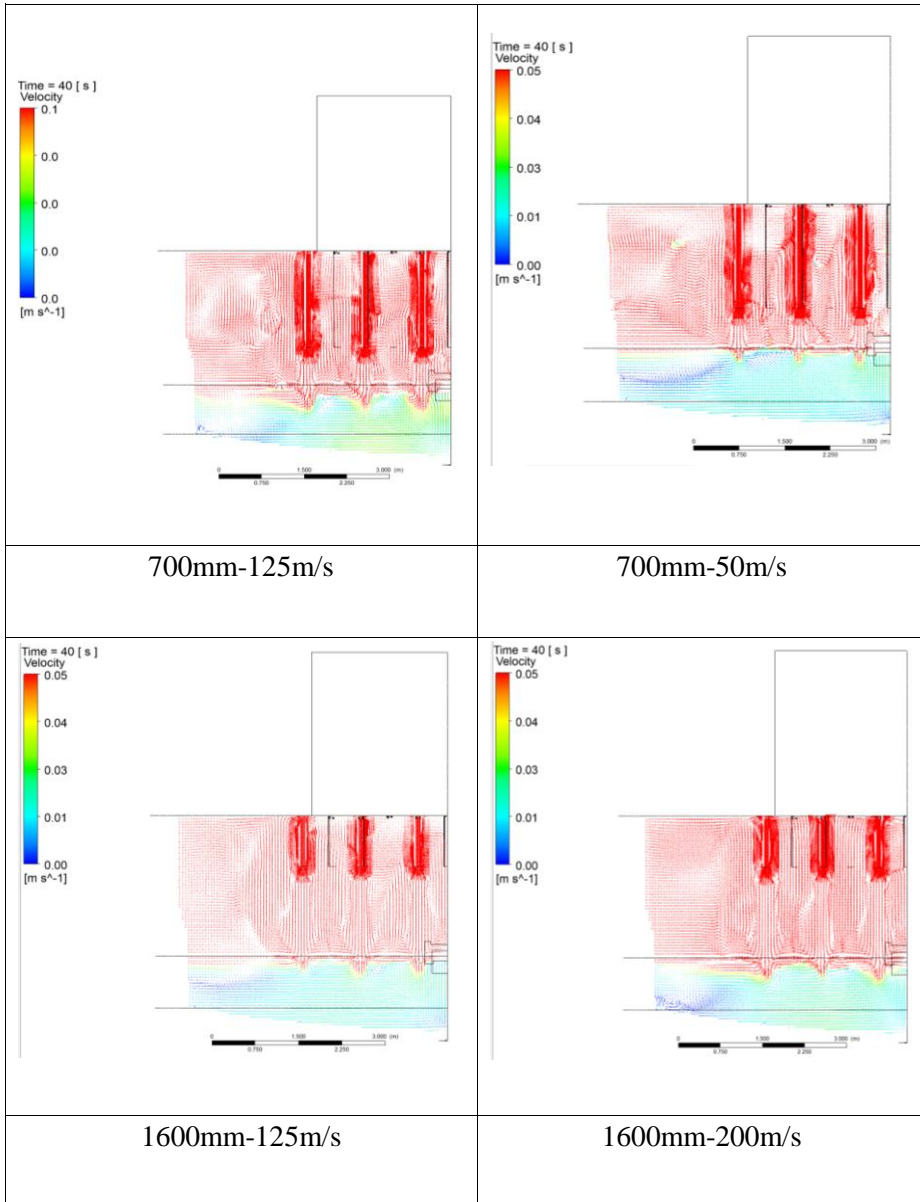
6. 3. Results and discussion

6. 3. 1. Comparison of flow change according to lance tip height and velocity

In order to observe the flow change of the furnace according to lance tip height and lance tip velocity, velocity, matte volume fraction, particle mass concentration and particle residence time at 40 seconds (gas and particle injection condition) are shown in Fig. 6-6, 6-7, 6-8 and 6-9.

In Fig. 6-6, legends are changed to emphasize the velocity of the matte. (Max. 0.05m/s) The lance tip height is low and lance tip velocity is high, the matte velocity is increased. Matte volume fractions at the vertical plane at 40 seconds are shown in Fig. 6-7. The lance tip height is low and lance tip velocity is high, the matte volume fraction is increased. Although lance tip height is close to the furnace top, if the lance tip velocity is high, matte could splashed to the lance tip. Especially, matte splashing is increased after particle injection.

Particle mass concentration at 40 seconds was compared. As Fig. 6-8 shown, the lance tip height is low and lance tip velocity is high, the particle splashing into the gas region is increased. The others conditions except for the 700mm-50m/s, particles can be splashed into the lance tip as soon as injected. (This model may differ from the actual system because this model does not considered the particle melting)



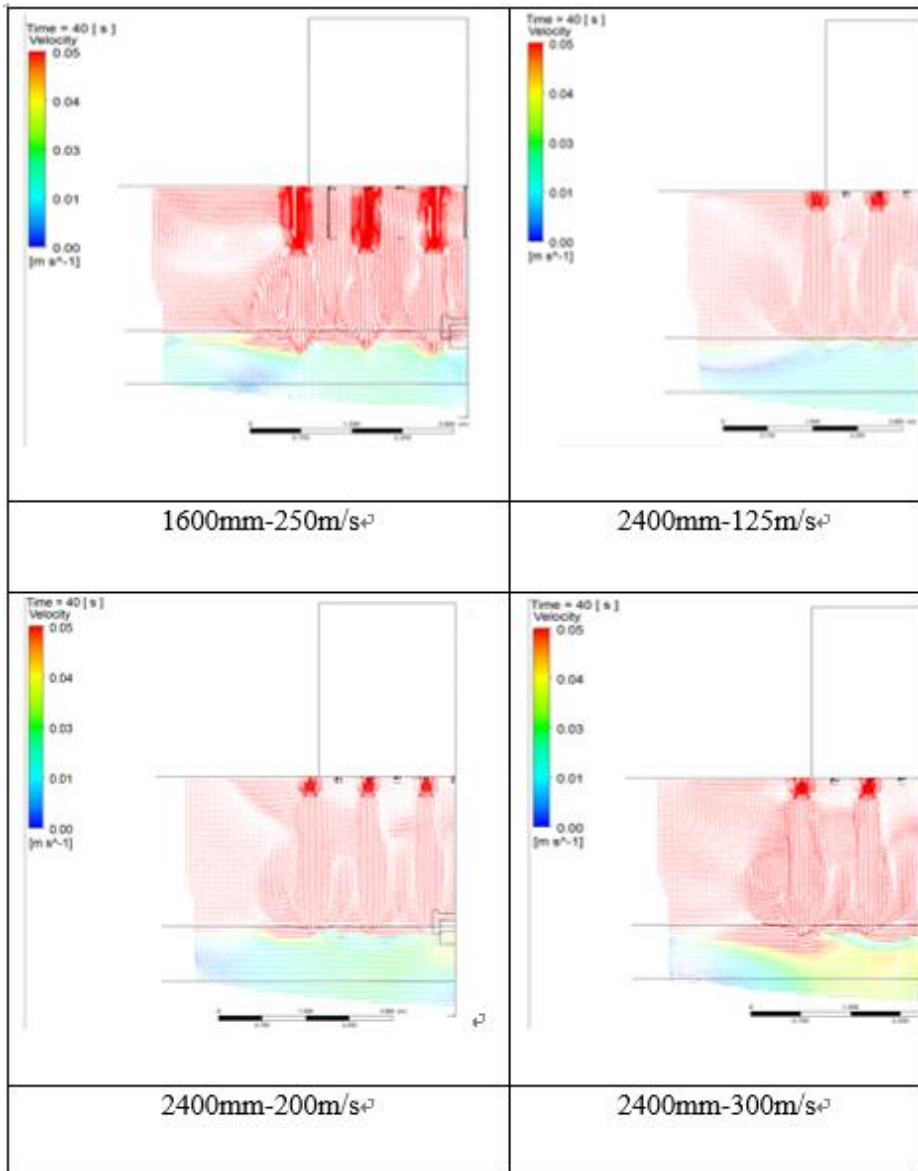
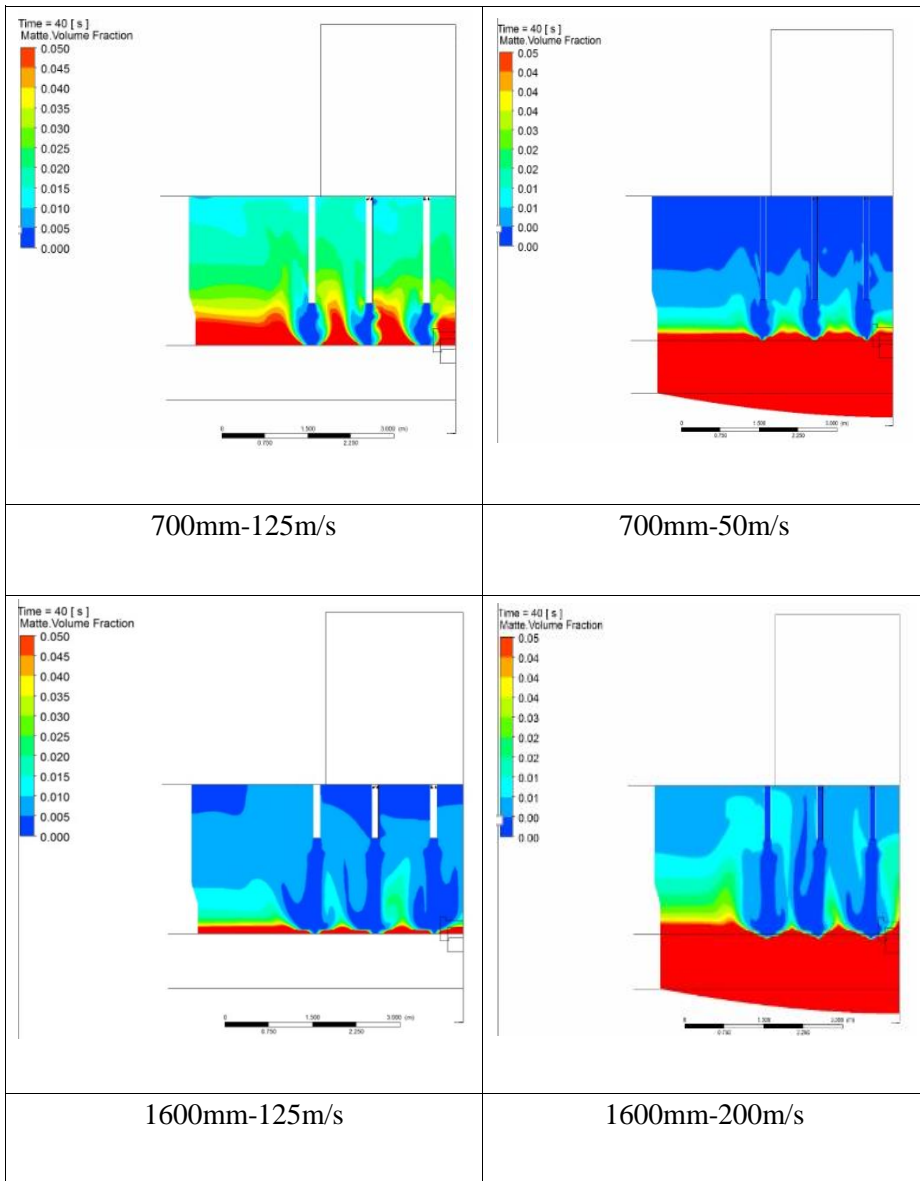


Fig. 6- 6 Velocity at the vertical plane at 40 seconds according to lance tip height and velocity.



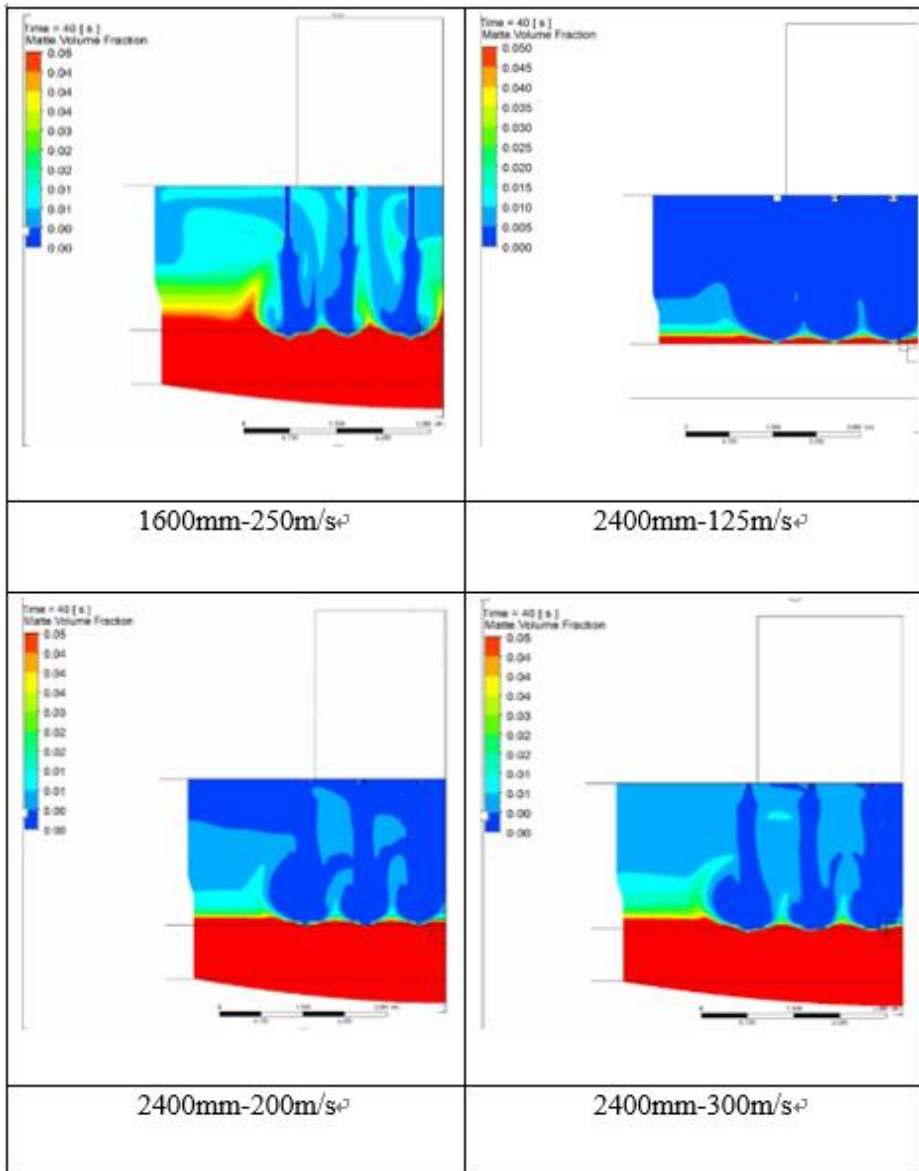
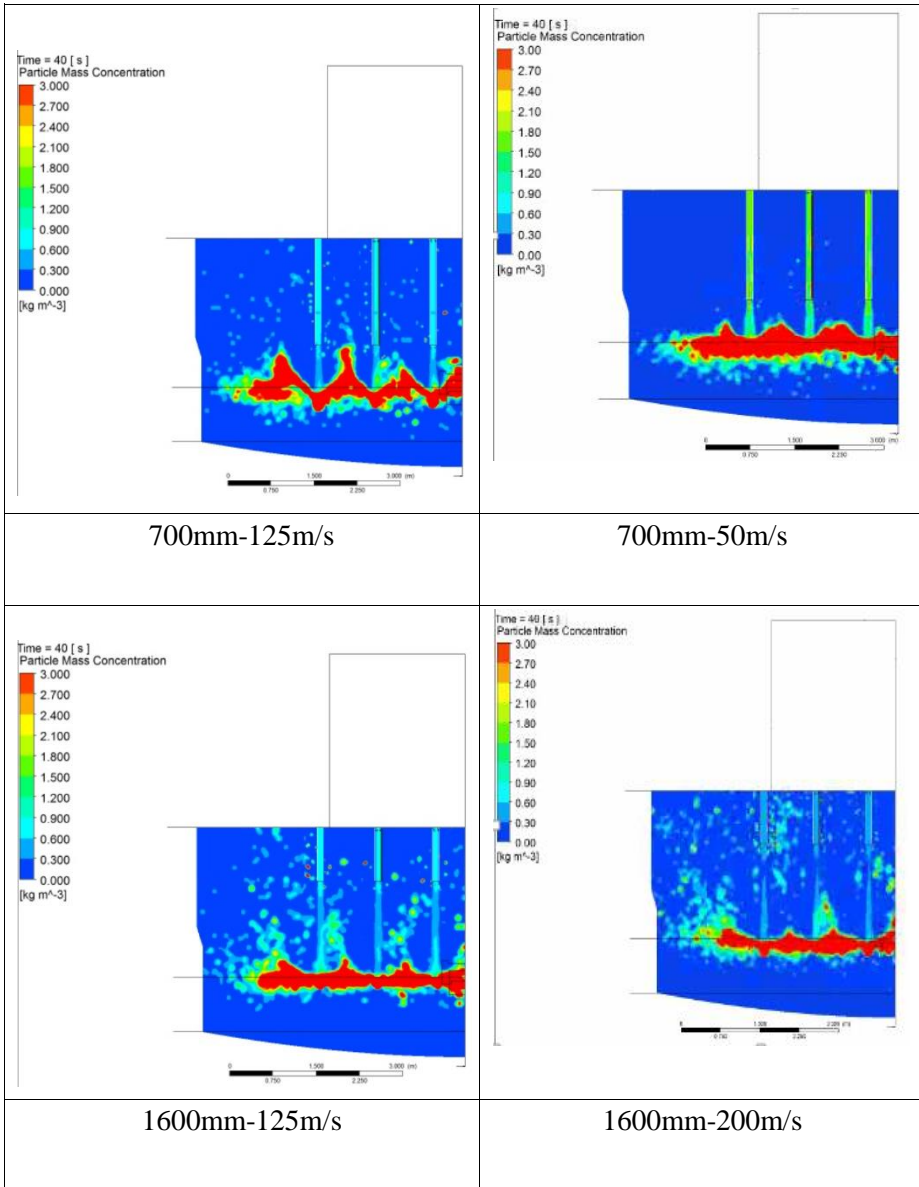


Fig. 6- 7 Matte volume fraction at the vertical plane at 40 seconds according to lance tip height and velocity.



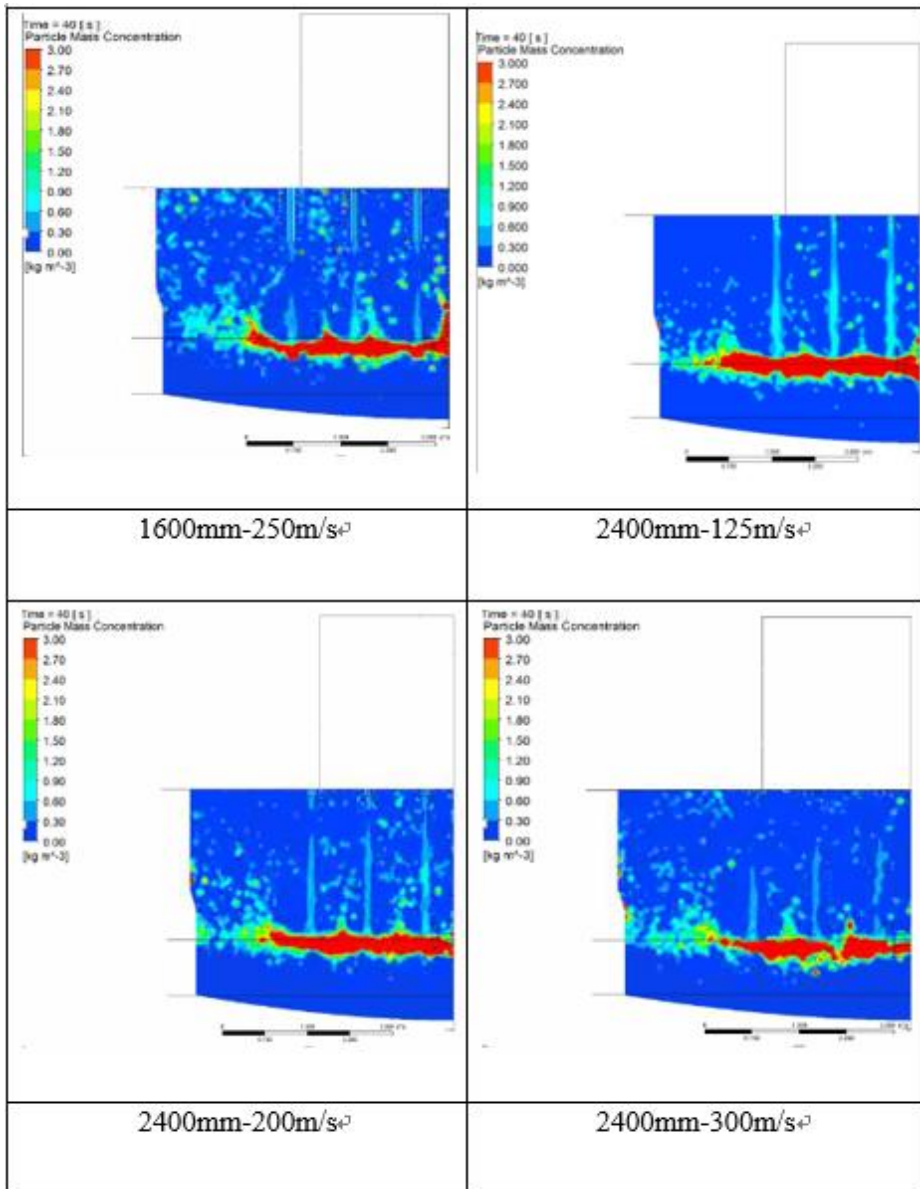
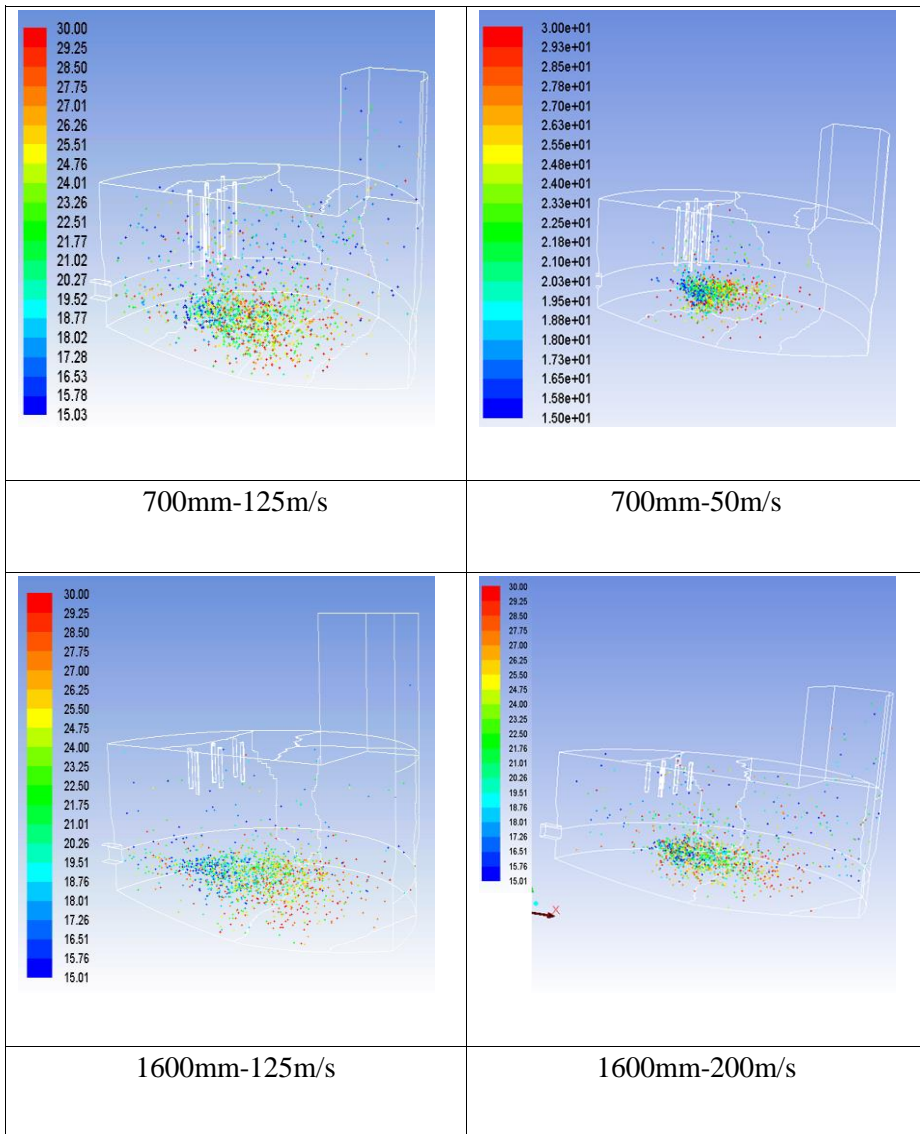


Fig. 6- 8 Particle mass concentration at the vertical plane at 40 seconds according to lance tip height and velocity.

Finally, single particle stream in the furnace was compared using particle tracking model. Like other analysis, the lance tip height is low and lance tip velocity is high, the movement of the particle is active. And the particle moves in a wider area when higher lance tip velocity is applied. On the other hand, if the lance tip velocity is high, there is a lot of matte splashing, so less particles moved to the outer area in the furnace.



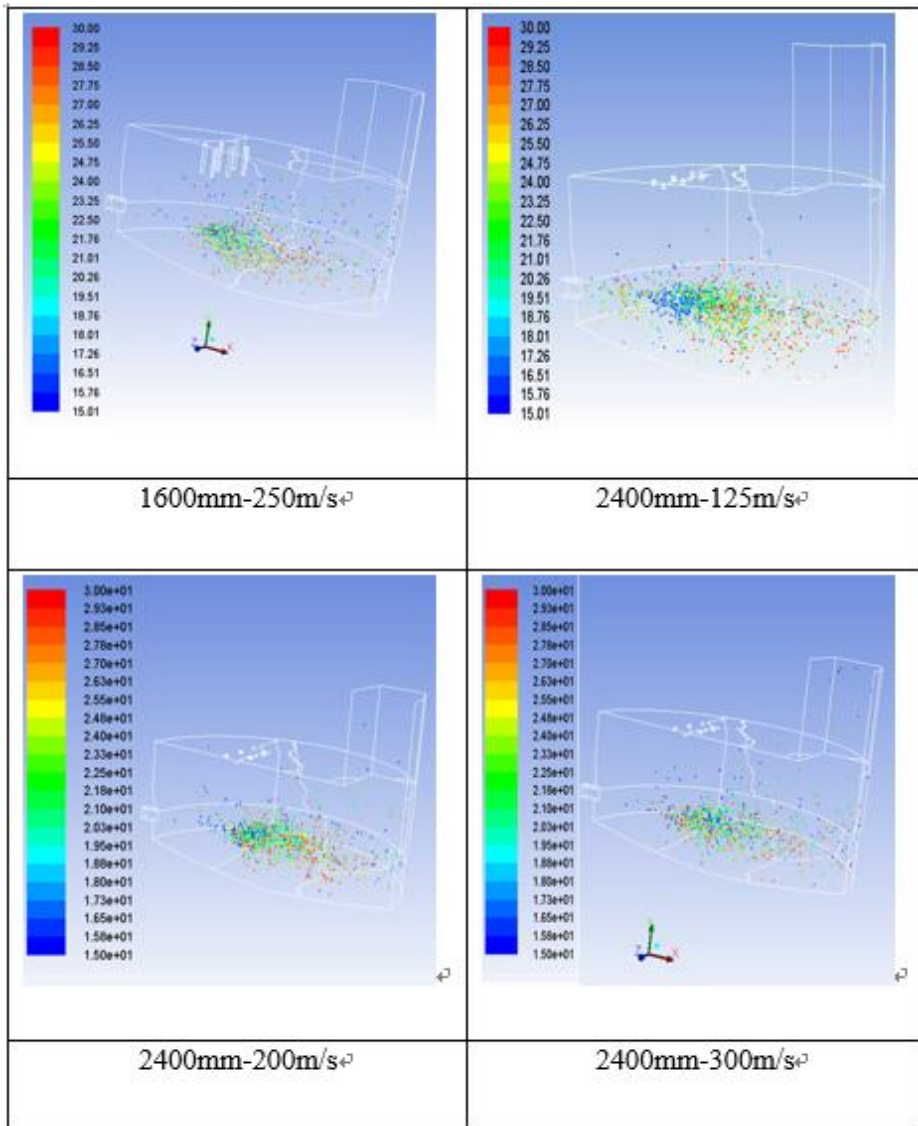


Fig. 6- 9 Single particle stream at 40 seconds according to lance tip height and velocity.

6. 2. 2. Comparison of matte mixing according to lance tip height and velocity

Matte average velocities according to lance tip height and velocity are compared. In Fig. 6-10, the horizontal axis is the lance tip height, the vertical axis is the matte average velocity. The average values of particle injection (35s-45s) and only gas injection (50s-60s) are extracted to compare by the figure according to the conditions. The Fig. 6-11 shows matte average velocity when gas and particle are injected (35s-45s) and Fig. 6-12 shows matte average velocity when gas is injected (50s-60s). As shown in both figures, the lance tip height is low and lance tip velocity is high, the matte average velocity is increased. In addition, a quantitative comparison of the input against output is not possible because this calculation has not considered the chemical reaction. So the matte average velocity of current condition (700mm-125m/s) is taken as matte mixing standard. It can be seen in these results that, to increase the mixing of the matte at the same lance tip height, lance tip velocity needs to be increased. 1600mm-225m/s and 2400mm-300m/s conditions result in matte mixing similar to present conditions.

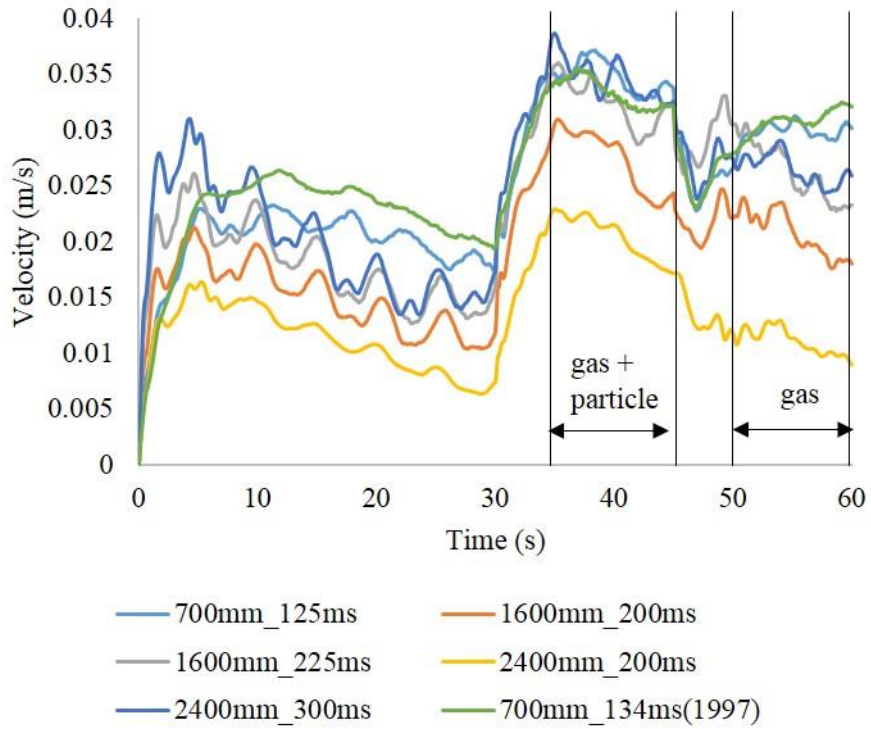


Fig. 6- 10 Matte average velocity change according to lance tip height and velocity.

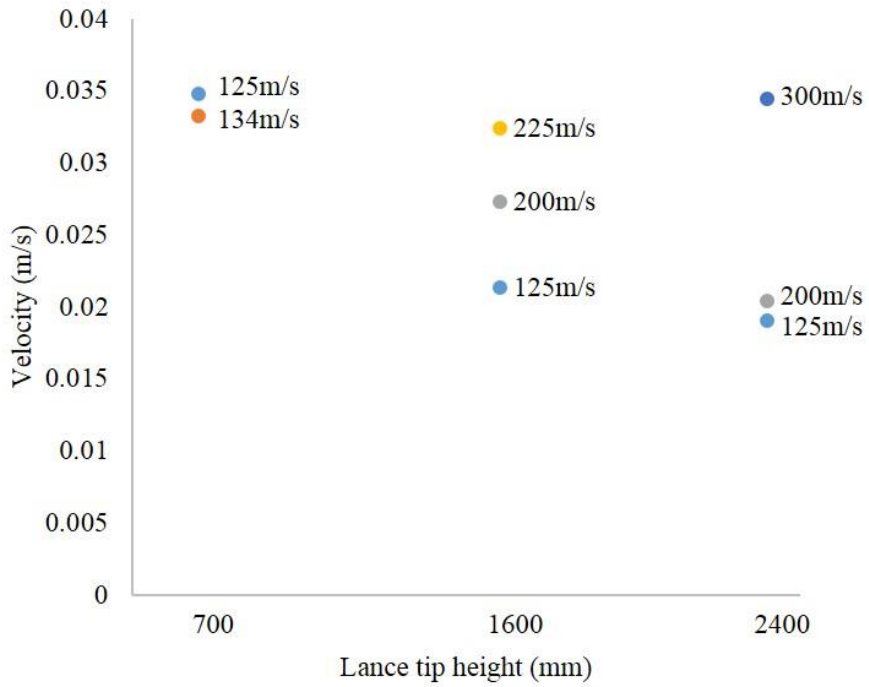


Fig. 6- 11 Matte average velocity according to lance tip height and velocity.

(Gas and particle injection, 35-45s)

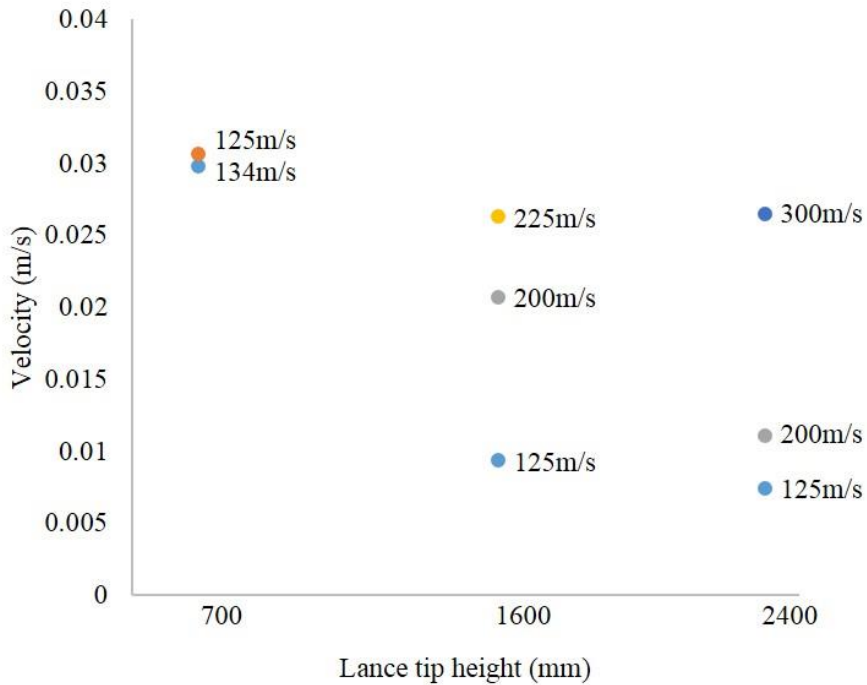


Fig. 6- 12 Matte average velocity according to lance tip height and velocity.

(Gas injection, 50-60s)

Another condition predicting the matte mixing, matte average turbulence kinetic energy is compared according to lance tip height and velocity. As Fig. 6-13 and 6-14 show, raising lance tip height can provide turbulence kinetic energy similar with present conditions if lance tip velocity is increased when gas and particle are injected. While the 1997 condition's input of the ore

is smaller than the present condition, matte average turbulence kinetic energy is smaller than the present condition when gas and particle are injected. But the 1997 condition's lance tip velocity is higher than the present condition, matte average turbulence kinetic energy is higher when gas is injected.

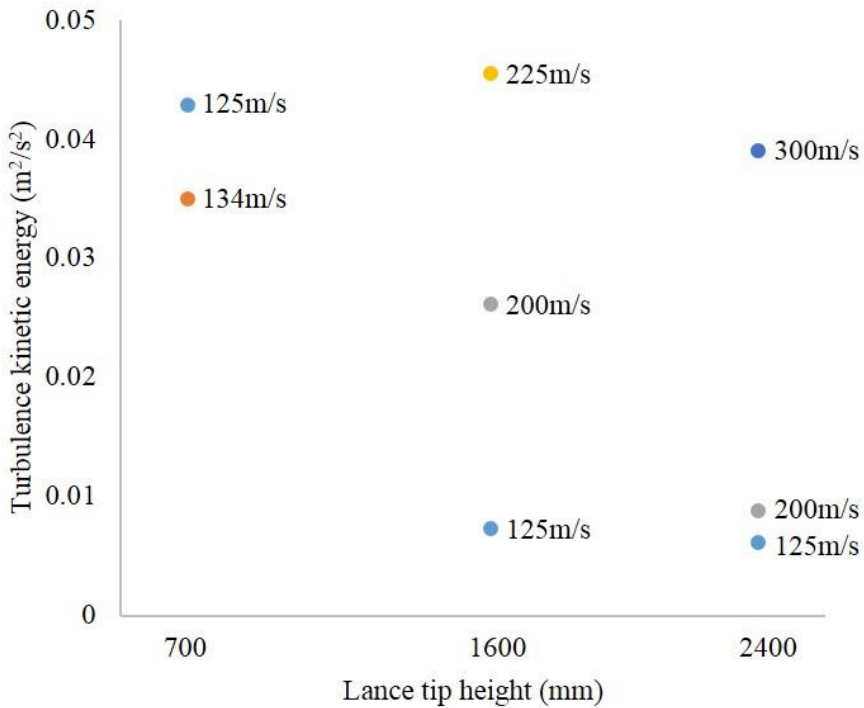


Fig. 6- 13 Matte average turbulence kinetic energy according to lance tip height and velocity.

(Gas and particle injection, 35-45s)

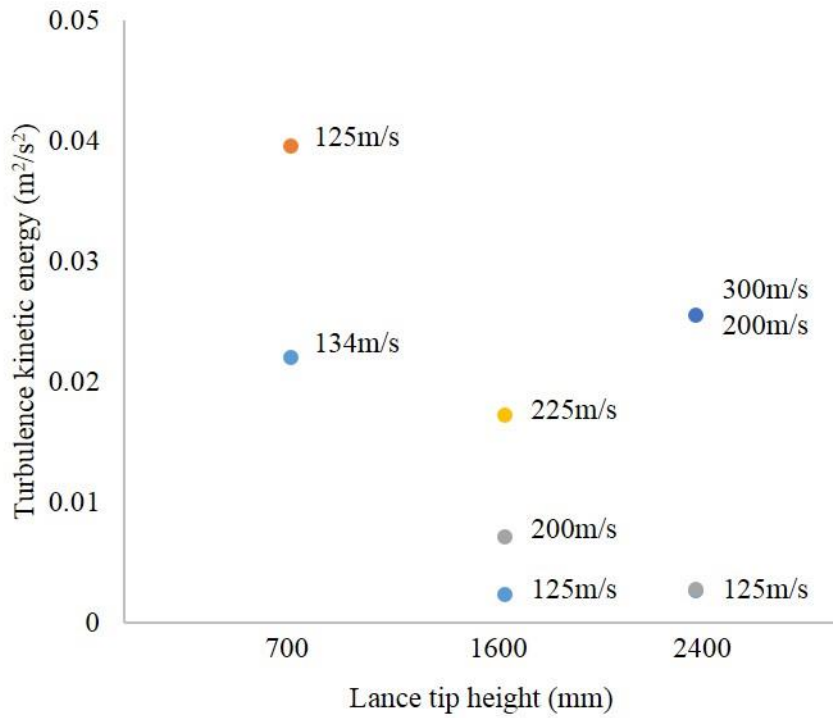


Fig. 6- 14 Matte average turbulence kinetic energy according to lance tip height and velocity.

(Gas injection, 50-60s)

6. 2. 3. Changes of other factors according to lance tip height and velocity

In the previous section, matte average velocity and matte average turbulence kinetic energy according to lance tip height and velocity are compared in the view of matte mixing. This section will evaluate the influence of other factors according to the change of the lance tip height and velocity.

First, the average matte volume fraction escaping to uptake outlet in the set area 2.6m which above the bath surface is compared according to lance tip height and velocity. As the Fig. 6-15 and 6-16 show, if the lance tip height is low and lance tip velocity is high, the matte mixing is good. But at this condition, escaping splashed matte to the uptake outlet will be increase. 1600mm-225m/s and 2400mm-300m/s conditions result in similar mixing to current conditions, and are stable due to lower degrees of matte splashing. Second, maximum depth of cavity created in the matte surface is compared according to lance tip height and velocity. As the Fig. 6-17 shows that if the lance tip height is low and lance tip velocity is high, the maximum depth of cavity is deepened. Therefore, the depth of cavity is deepened when matte mixing is high. This deep cavity has a negative effect of wearing on the bottom refractory to increase the incoming pressure and causes the refractory wearing more easily. And 1600mm-225m/s and 2400mm-300m/s conditions result in similar mixing to current conditions and are stable due to lower cavity depth.

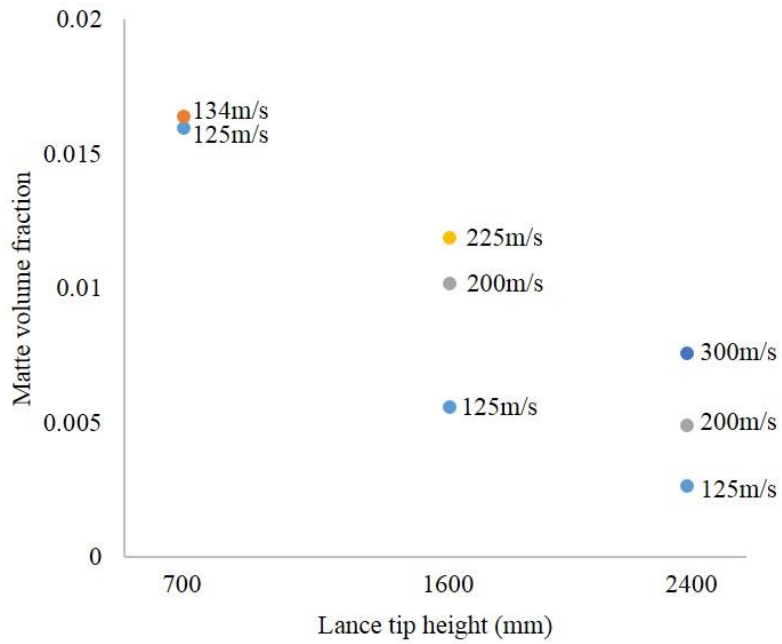


Fig. 6- 15 Uptake outlet's (2.6m from the initial bath surface) matte average volume fraction according to lance tip height and velocity.

(Gas and particle injection, 35-45s)

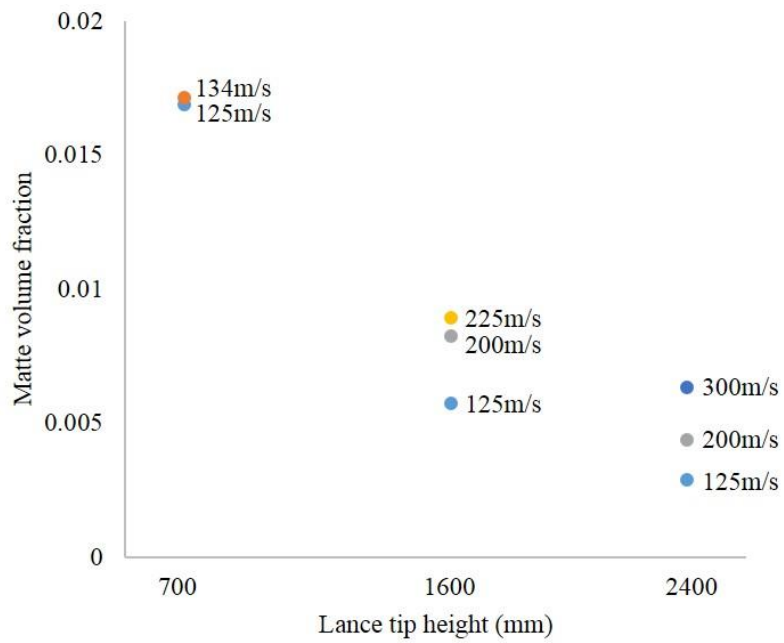


Fig. 6- 16 Uptake outlet's (2.6m from the initial bath surface) matte average volume fraction according to lance tip height and velocity.

(Gas injection, 50-60s)

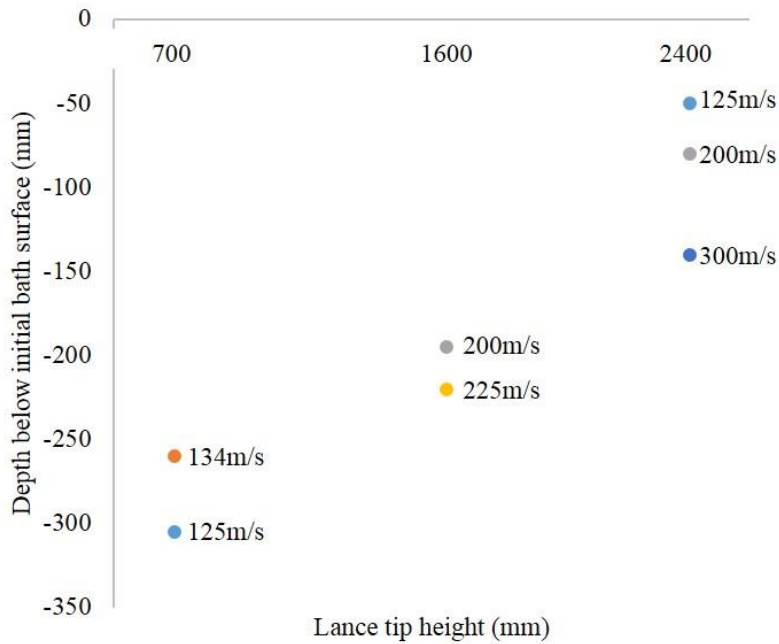


Fig. 6- 17 Maximum depth of cavity (below the initial bath surface) according to lance tip height and velocity.

Third, the average matte volume fraction at the lance tip is compared according to lance tip height and velocity. As Fig. 6-18 and 6-19 show, both injection condition's average splashed matte volume fraction at the lance tip are lower than 1997 condition. While the splashed matte of the 1997 condition is lower than present condition. Because 1997 condition has a higher tip velocity but less lance number and ore's flow rate. It can be confirmed that the flow rate of

ore has a significant effect on splashing of the matte. Finally, change of the lance temperature according to lance height and velocity is analyzed. The maximum values of the temperature difference between inner and outer surface are compared according to lance height and velocity. If lance temperature difference can be large, the lance is expected to be under bigger thermal stress. As shown in Fig. 6-20, 1600mm-225m/s and 2400mm-300m/s conditions result in similar mixing with current conditions, and are stable due to lower temperature difference between inner and outer surfaces.

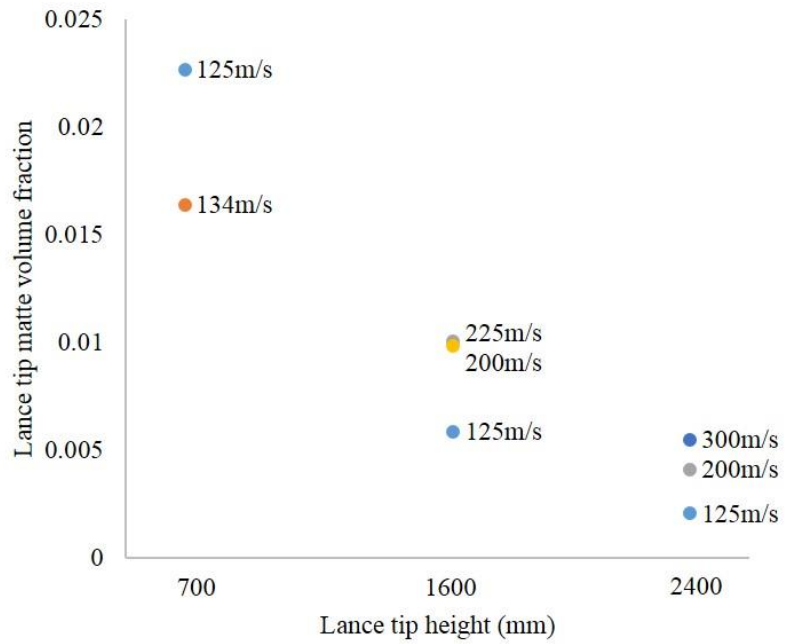


Fig. 6- 18 Lance tip matte volume fraction according to lance tip height and velocity.

(Gas + particle injection, 35-45s)

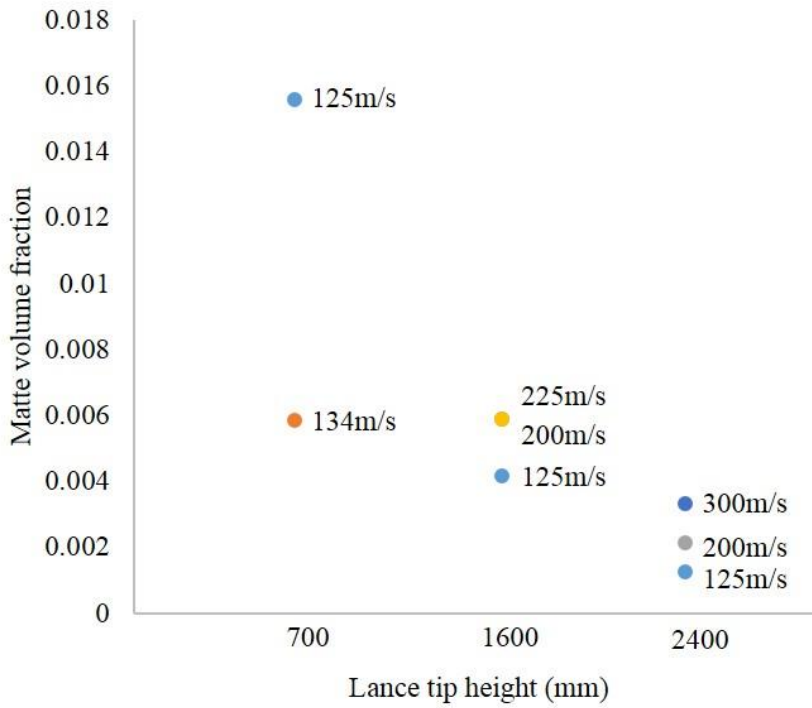


Fig. 6- 19 Lance tip matte volume fraction according to lance tip height and velocity.

(Gas injection, 50-60s)

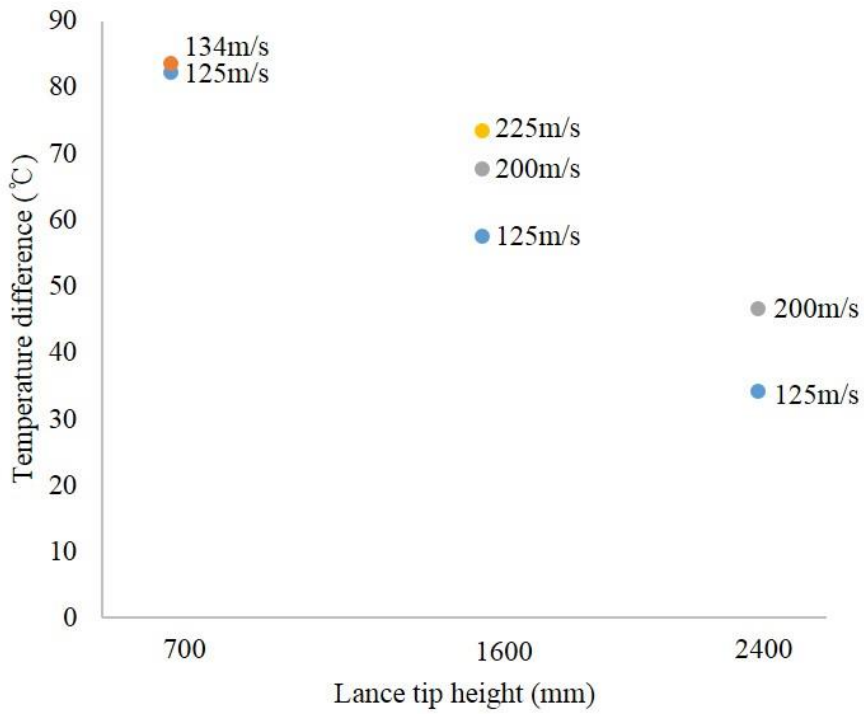


Fig. 6- 20 Lance tip temperature difference between inner and outer surface according to lance tip height and velocity.

6. 3. Additional test result and discussion

Previous lance tip height and velocity change tests have not applied heat transfer. So in this additional test, heat transfer is applied and lance tip height was changed by 1500mm from the initial bath surface. The lance tip velocity is 125m/s. Other calculation and measurement conditions are same as previous conditions.

The lance temperature variation is shown in Fig. 6-21. The lance temperature is measured in middle and high points with the height and inner, body and outer points with the thickness as the Fig. 2-3. The inner lance temperature is under 820°C and outer lance temperature is under 900°C at the middle height points. Even the outer lance temperature is under 700°C at the high height points. This temperature range is similar as the 700mm lance tip's middle and high height, shown in Fig. 4-5. The middle point of 700mm is 1500mm's lance tip. Although same heat flux is applied in this calculation, yet the lance tip temperature is lower than 1000°C. Therefore, the high temperature problems, e. g. hot shortness, (red-short or sulfur embrittlement) which occurs in above 1100°C, will not occur in the lance tip height 1500mm.

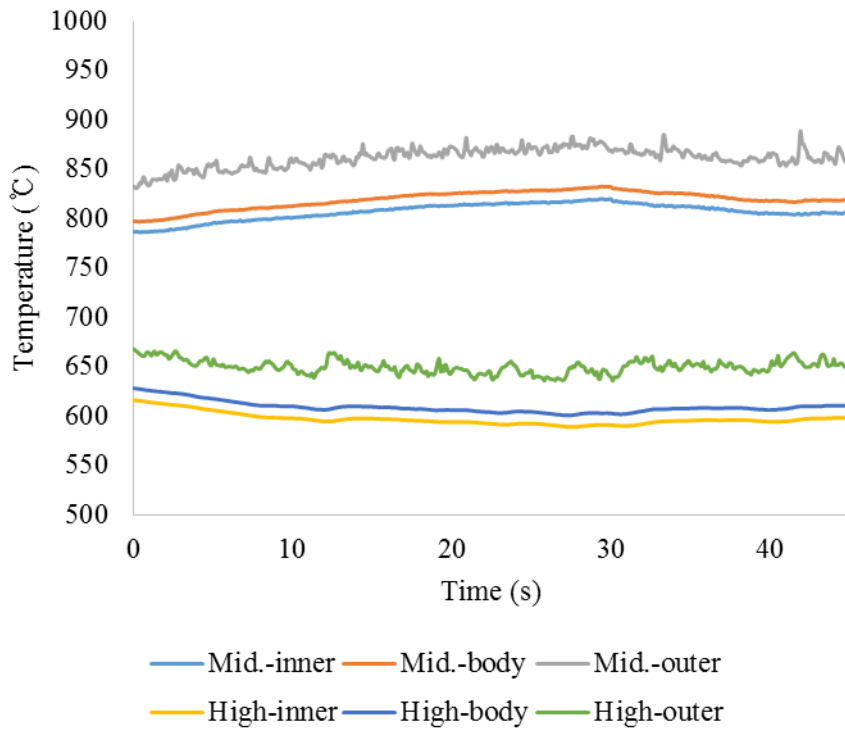


Fig. 6- 21 Lance temperature variations from 0 to 45 seconds.

(0-30s: gas injection / 30-45s: gas and particle injection)

In order to compare the thermal stress of the lance between 700mm and 1500mm, structure analysis is performed using 1-way FSI method. The lance temperature distribution at 30 seconds expected highest temperature is shown in Fig. 6-22 together with 700mm's result. The maximum and minimum temperatures occurs in outer lance, the maximum temperature is 1184.1°C which is about 150°C lower than 1131.1°C of 700mm and the minimum temperature is 506.1°C which is about 140°C lower than 645.3°C of 700mm. The maximum temperature around the lance tip is lower due to the far distance from the high temperature matte surface. And the minimum temperature around the lance top is lower too. It means that if the lance tip height is high, lance is stable for the thermal stress.

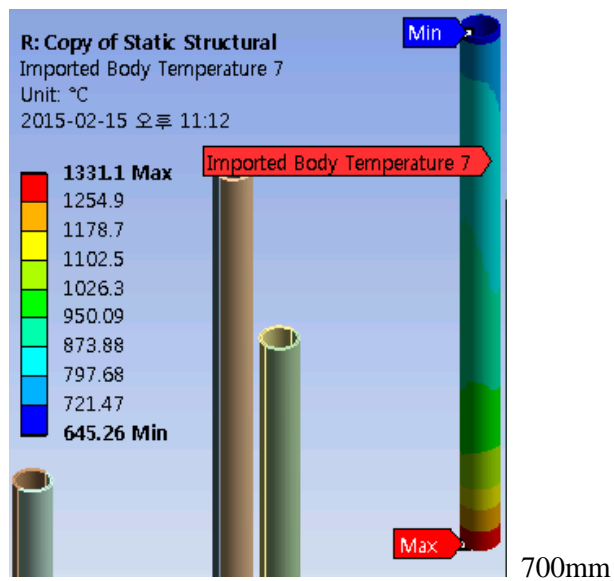
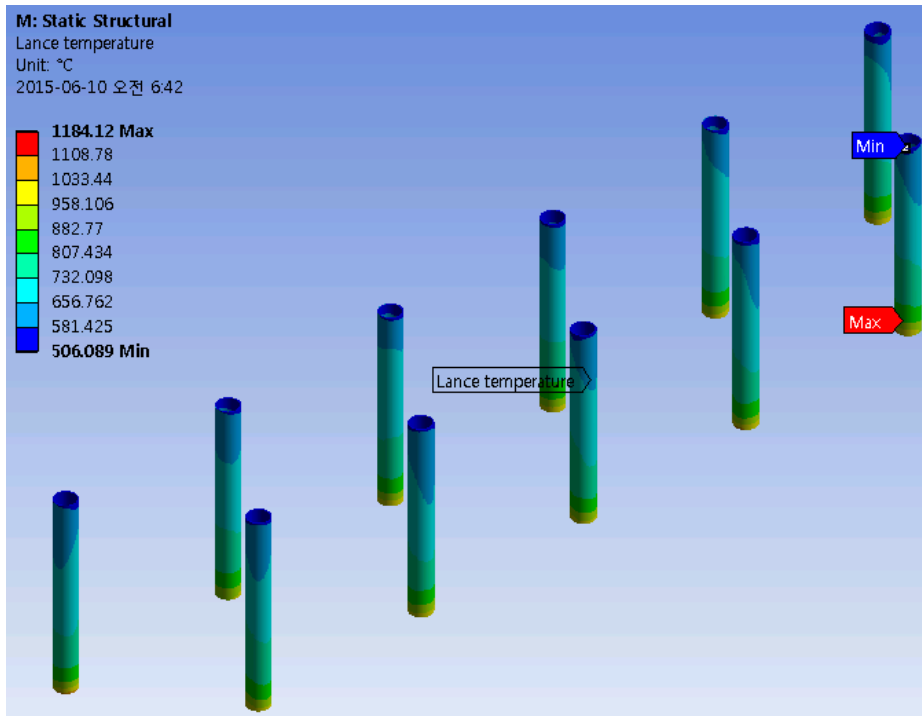


Fig. 6- 22 Lance temperature distribution. (Gas injection, 30s)

The Von Mises Stress (Equivalent stress) of the lance which has 1500mm lance tip height is shown in Fig. 6-23 and compared with 700mm's result. Whereas most regions of the lances with 700mm lance tip are higher than 96.46 MPa which is yield strength of A297HC at 760°C, values of the regions of the lances with 1500mm lance tip are lower than 100MPa. It means that lance with 1500mm lance tip undergoes less thermal stress and plastic deformation during processing than the lance with 700mm lance tip. In addition, lance material is replaced by copper and copper lance equivalent stress is shown in Fig. 6-24. From these results, copper lance has less plastic deformation than A297HC lance and is more stable at the high temperature. Because copper thermal conductivity is higher than A297HC. (Copper: 387.6W/mK, A297HC: 31.49W/mK) Although other characteristics of Cu should be checked later, Cu lance can be used in the 1500mm's processing when only melting point is considered. (Copper melting point: 1084.62°C)

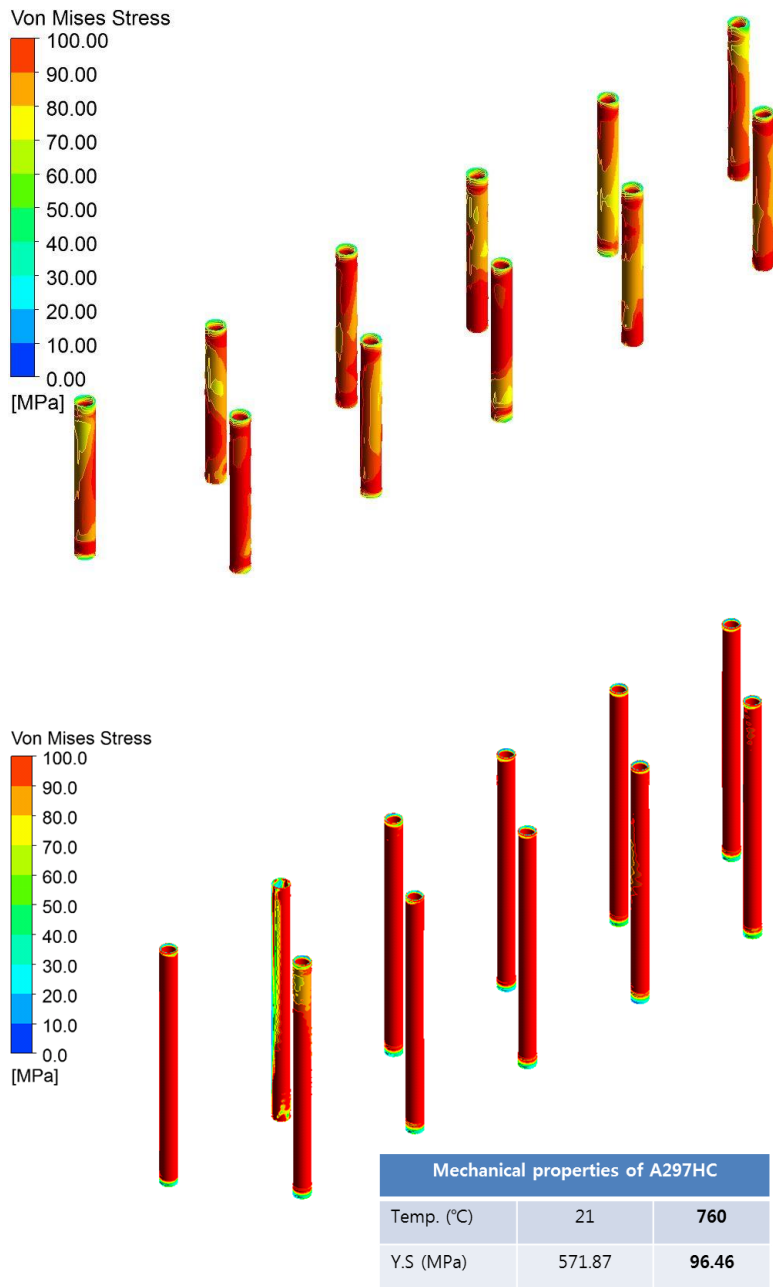


Fig. 6- 23 Comparison of calculated equivalent stress and literature yield strength (MPa). Up: 1500mm / Low: 700mm.

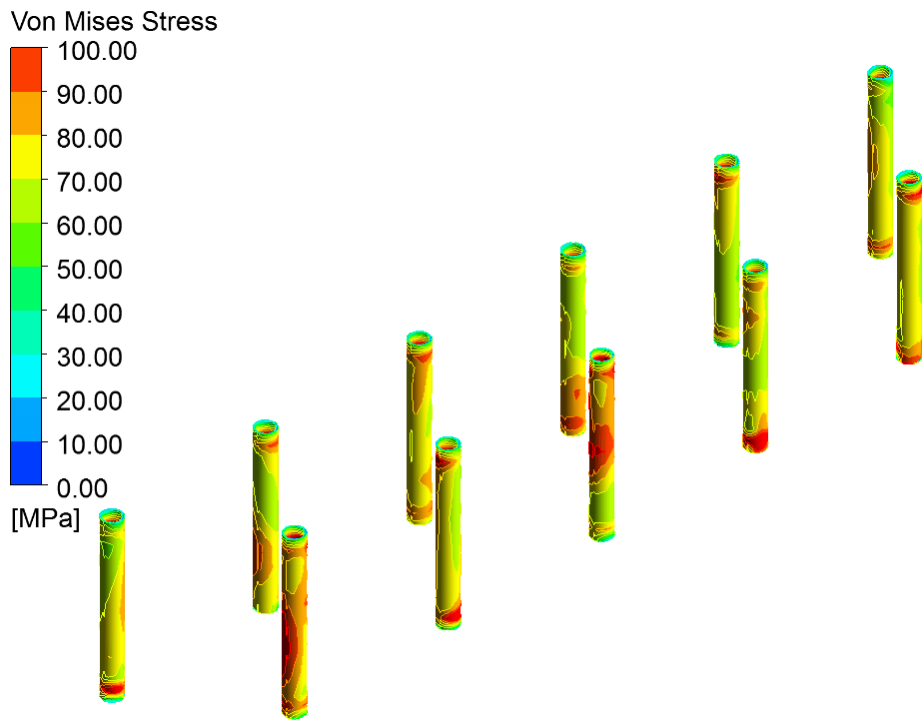


Fig. 6- 24 Equivalent stress of copper lance (MPa).

6. 4. Summary

Though raising lance tip can resolve lance fracture, it can result in diminished matte mixing. Matte average velocity and matte average turbulence kinetic energy of present condition (700mm-125m/s) are assumed in the figures that represent matte mixing. Stable conditions are acquired when lance tip height is raised and lance tip velocity is raised to levels identical to mixing by present conditions, uptake average matte volume fraction is decreased, depth of cavity is decreased, matte volume fraction of the lance tip is decreased and lance inner-outer surface temperature difference is decreased. Especially, 1600mm-225m/s and 2400mm-300m/s conditions result in degree of mixing similar with present conditions, while improving stability. Of the two conditions, 1600mm-225m/s condition is to be more stable because of lower lance tip velocity. While 1997 condition result in similar results with present conditions in terms of mixing and stability.

In the calculation of lance tip changed to 1500mm with heat transfer, lance temperature decreases and lance thermal stress decreases. Calculation is employed to adjust lance tip height and velocity, thereby optimized conditions which improve stability and prevent lance fracture.

Chapter 7. Conclusions

The present study focused on numerical simulation in the smelting process of the Mitsubishi continuous process for copper production. In order to perform this investigation, we developed a comprehensive 3-D and transient numerical analysis model of the process. And we measured the temperature change in the furnace during an operation by thermo-couple embedded into the lance to investigate the temperature behavior in the furnace and to verify the validity of numerical simulation. The numerical simulation model is coupled with VOF model for two phase, DPM model for particle tracking and P-1 model for radiation and well matched to experimental results. Using the experiment and numerical simulation the following results were found to appear in the furnace.

By injection of gas and/or particles, complex velocity field of gas and melt was generated in the furnace and velocities are constantly fluctuating. When particles are co-injected with gas, strong agitation appears in the melt, the depth of cavity increases and the amount of splashed matte and slag increases. The temperature of lance increase during gas injection and decrease during gas and particles injection. The fluctuation of melt volume fraction near the lance induce temperature fluctuation at the outer surface of lance. Lance materials are exposed very severe conditions such as wide range of temperature change and cyclic change of large temperature gradient across the thickness.

The microstructure of before-using lance and fractured lance were analyzed by SEM, EDS, EBSD and AES. The lance is a high-Cr and a duplex stainless steel. But it was confirmed that Cr depleted at the interior and exterior lance surface, while substances composed of S, Si and O penetrated the grain boundaries. This leads us to believe that Cr depletion and penetration of S, Si and O into the grain boundaries weakens the lance exterior, while low cycle thermal fatigue and external factors such as splashed melt during processing leads to quicker crack propagation and eventual fracture. Therefore, in order to prevent the lance fracture, lower the lance temperature, reduce the lance temperature change range and a more stable lance composition to Cr depletion are needed.

Raising the lance tip & velocity test results show that lower lance tip height and higher lance tip flow velocities result in less stable flow phenomena within the furnace. We also confirmed that even when the lance tip is raised, and increased flow velocity can maintain an equivalent degree of matte mixing, while stabilizing flow phenomena. In particular, it was found that raising the lance tip decreases its temperature and thermal stress, so that optimized conditions improve stability and prevent lance fracture.

Through the present study, we were able to develop a comprehensive 3-D numerical model within the S-furnace which are not easily accessible by direct experimentation. We were able to recreate lance temperature changes

through calculations taking into account heat and confirmed the thermal stresses under the lance. Through analysis of lance fracture surface, we predicted the mechanism by which lance fracture occurs, and confirmed that raising the lance tip can result in stable conditions for the furnace interior and lance stability.

References

- [1] T. Shibasaki and M. Hayashi, “Top-blown injection smelting and converting: The Mitsubishi process”, JOM September, p. 20-26. (1991)
- [2] 제련 2공정 교육자료, LS-Nikko Copper. (2010)
- [3] W. G. Davenport, M. King, M. Schlesinger, and A. K. Biswas., Extractive metallurgy of copper, 4th edition, ELSEVIER Sci. Ltd., p. 57-72. (2002)
- [4] Etsuji Kimura, “Fundamental research of lancing mechanism in Mitsubishi continuous smelting furnace”, ISIJ, **23**, p. 522-529. (1983)
- [5] M. Goto, E. Oshima, and M. Hayashi., “Control aspects of the Mitsubishi continuous process”, JOM April, p. 60-64. (1998)
- [6] M. Goto and T. Echigoya, “Effect of injection smelting jet characteristics on refractory wear in the Mitsubishi process”, J.Metals, **32** (11). (1980)
- [7] R. Sridhar, J. M. Toguri, and S. Simeonov, “Thermodynamic considerations in the pyrometallurgical production of copper”, 35th Annual conference of Metallurgist of CIM, Toronto, Canada, August. (1996)
- [8] T. Utigard, J. M. Toguri, and T. Nakamura, “Interfacial tension and flotation characteristics of liquid metal-sodium flux systems”,

- Metallurgical Transactions B, 17B, p.339-346. (1986)
- [9] M. Goto and N. Kikumoto, “Process analysis of Mitsubishi Continuous copper smelting and converting process”. (1981)
- [10] Z. Asaki, T. Taniguchi, and M. Hayashi, “Kinetics of the reactions in the smelting furnace of the Mitsubishi process”, JOM May, p. 25-27. (2001)
- [11] S. Akima, M. Hayashi, M. Nishiyama, “The Mitsubishi continuous process – Present and future”, J. Min. Mater. Process Inst. Jpn., p. 161-176. (1993)
- [12] A. W. Sundstrom, J. J. Eksteen, and G. A. Georgalli, “A review of the physical properties of base metal mattes”, SAIMM, p.431-438. (2008)
- [13] A. H. Alyaser and J. K. Brimacombe, “Oxidation kinetics of molten copper sulfide”, Metall. and Mater. Trans. B, **26B**, p. 25-40. (1995)
- [14] T. Kumagai and M. Iguchi, “Instability phenomena at bath surface injected by top lance gas injection”, ISIJ, **41**, p. S52-S55. (2001)
- [15] W. Wang, Z. Yuan, H. Matsuura, H. Zhao, C. dai, and F. Tsukihashi, “Three-dimensional compressible flow simulation of top-blown multiple jets in converter”, ISIJ, **50**, p. 491-500. (2010)
- [16] J. Wang, H. Ootabu, F. Wang, and M. Igushi., “Swirl motion in an cylindrical bath agitated by top lance gas injection”, ISIJ, **51**, p. 1080-1085. (2011)
- [17] H. -Y. Sohn, G. -W. Seo, and Y. -B. Han, “The combustion of copper

- sulfide concentrate particles in an turbulent gas jet”, J. of the Korean Ins. of Chemacal Eng., 27 (4), pp.531-547. (1989)
- [18] M. Iguchi, T. Uemura, H. Yamagushi, T. Kuranaga, and Z. I. Morita, “Fluid flow phenomena in an cylindrical bath agitated by top lance gas injection”, ISIJ Inter., 34 (12), p.973-979. (1994)
- [19] J. Solorzano-Lopez, R. Zenit, and M. A. Ramirez-Argaez, “Mathematical and physical simulation of the interaction between a gas jet and a liquid free surface”, Appied Math. Modelling, **35**, p. 4991-5005. (2011)
- [20] E. Scheepers, J. J. Eksteen, and C. Aldrich, “Optimisation of the lance injection desulphurisation of melten iron using dynamic modelling”, Minerals Eng., **19**, p.1163-1173. (2006)
- [21] M. Ersson, A. Tilliander, L. Jonsson, and P. Jonsson, “A mathematical model of an impinging air jet on an water surface”, ISIJ Inter., 48 (4), p.377-384. (2008)
- [22] N. Huda, J. Naser, G. Brooks, M. A. Reuter, and R. W. Matuszewicz, “CFD modeling of swirl and nonswirl gas injections into liquid baths using top submerged lances”, Metal. and Mater. Trans. B, 41B Feb., p.35-50. (2010)
- [23] S. -S. Park, N. Dyussekenov, and H. -Y. Sohn, “The penetration behavior of an annular gas-solid jet impinging on a liquid bath: Comparison with a conventional circular jet”., Metall. and Mater. Trans.

- B, **41B**, p. 51-62. (2010)
- [24] J. -S. Chang and H. -Y. Sohn, “The penetration behavior of an annular gas-solid jet impinging on an liquid bath: The effects of the density and size of solid particles”, Metall. and Mater. Trans. B, **43B**, p. 787-813. (2012)
- [25] Y. -B. Hahn and H. -Y. Sohn, “Mathematical modeling of sulfide flash smelting process: Part I. Model development and verification with laboratory and pilot plant measurements for Chalcopyrite concentrate smelting”, Metal. Trans. B, **21B** December, p.945-958. (1990)
- [26] M. Nagamori, W. J. Errington, P. J. Mackey, and D. Poggi, “Thermodynamic simulation model of the Isasmelt process for copper matte”, Metal. and Mater. Trans. B, **25B** December, p.839-853. (1994)
- [27] J. Vaarno, J. Jarbi, T. Ahokainen, T. Laurila, and P. Taskinen, “Development of a mathematical model of flash smelting and converting process”, CSURO Australia, p.147-154. (2003)
- [28] X. F. Li and T. Xiao, “Production enhancement and operation parameter’s optimization of the flash smelting furnace based on numerical simulation”, CSIRO Australia, p.155-160. (2003)
- [29] H. T. Abuluwefa, “Application of computer programming to model the process of continuous converting of copper matte”, EngOpt 2008.
- [30] J. -W. Nam and K. -W Seo, “A simulation of the fluid field in an flash smelting furnace”, CHERIC, 3(2), p.3033. (1997)

- [31] Loris Molino, “Gas flows and mixing in models of the Inco flash smelting furnace”. (2001)
- [32] FLUENT Theory guide, Fluent Inc., p.24-60. (2013)
- [33] FLUENT Theory guide, Fluent Inc., p.545-558. (2013)
- [34] T. -Y. Kim and B. -S. Hyun, “Analysis of low field including bodies steadily moving around the free-surface by FLUENT-VOF method”, *Journal of Navigation and Port Research*, 32 (1), p.9-14. (2008)
- [35] A. Calson, P. Kudinov, and C. Narayanan, “Prediction of two-phase flow in small tubes: A systematic comparison of state-of-the-art CMFD codes”, 5th European Thermal-Sciences Conference, The Netherlands. (2008)
- [36] Z. H. Sun and R. J. Han, “Simulation solution for micro droplet impingement on a flat dry surface”, *Chinese Physics B*, 17 (9), p.3185-3188. (2008)
- [37] Federico Montanari and Jiefu Ma, “Exploratory CFD analyses of the fluid dynamics of a water cannon”, *AIAA*, 1293, p.1-18. (2005)
- [38] FLUENT Theory guide, Fluent Inc., p.387-490. (2013)
- [39] M. Alam, J. Naser, G. Brooks, and A. Fontana, “A computational fluid dynamics model of shrouded supersonic jet impingement on a water surface”, *ISIJ Inter.*, 52 (6), p.1026-1035. (2012)
- [40] Maksim Mezhericher, “Modeling of particle pneumatic conveying using DEM and DPM methods”, *Particulate Sci. and Tech.*, 29, p.197-

208. (2011)
- [41] R. J. Robinson, P. Snyder, and M. J. Oldham, “Comparison of particle tracking algorithms in commercial CFD packages: Sedimentation and diffusion”, *Inter. Forum for Respiratory*, 19 (6-7), p.517-531. (2007)
- [42] Liming Shi and David J. Bayless, “Comparison of boundary conditions for predicting the collection efficiency of cyclones”, *Powder Tech.*, 173, p.29-37. (2007)
- [43] D. -H. Kang and Richard K. Strand, “Modeling of simultaneous heat and mass transfer within passive down-draft evaporative cooling (PDEC) towers with spray in FLUENT”, *Energy and Buildings*, 62, p.196-209. (2013)
- [44] B. R. Cornard, R. Sridhar, and J. S. Warner, “High-temperature thermodynamic properties of chalcopyrite”, *J. Chem. Thermodynamics*, 12, p.817-833. (1980)
- [45] FACTSAGE 6.4, Thermochemistry Software, Thermfact/CRCT and GTT-Tech. (2014)
- [46] FLUENT Theory guide, Fluent Inc., p.149-153. (2013)
- [47] J. J. Beazuidenhout, J. J. Eksteen, and S. M. Bradshaw, “Computational fluid dynamic modelling of an electric furnace used in the smelting of PGM containing concentrates”, *Minerals Eng.*, 22, p.995-1006. (2009)
- [48] K, -I Horai and G. Simmons, “Thermal conductivity of rock-forming minerals:”, *Earth and planetary Sci. Lett.*, 6, p.359-368. (1969)

- [49] Steel Casting Handbook, Supplement 9, High Alloy Data Sheets, Heat Series, p.5, Steel Founders' Society of America. (2004)
- [50] C. L. He, R. Zhu, K. Dong, Y. Q. Qiu, and K. M. Sun, "Modeling of an impinging oxygen jet on molten bath surface in 150 t EAF", *J. of Iron and Steel Res. Inter.*, 18(9), p.13-20. (2011)
- [51] M. Wakamatsu, H. Nei, and K. Hashiguchi, "Attenuation of temperature fluctuations in thermal striping", *J. of Nuclear Sci. and Tech.*, 32(8), p.752-762. (1995)
- [52] L.-W Hu and M. S. Kazimi, "LES benchmark study of high cycle temperature fluctuations caused by thermal striping in a mixing tee", *Inter. J. of Heat and Fluid Flow*, 27, p.54-64. (2006)
- [53] D. A. Spera, D. F. Mowbray, Thermal fatigue of materials and components, AMERICAN SOCIETY FOR TESTING AND MATERIALS. (1976)
- [54] FLUENT, User's Guide, Fluent Inc., p.114-124. (2013)
- [55] Stainless steel: Tables of Technical Properties, Materials and Applications Series, Volume 5.
- [56] <http://www.bssa.org.uk/topics.php?article=42>
- [57] A. Grodner, *Weld. Res. Counc. Bull.*, No. 31. (1956)
- [58] S. Kado et al, "High-temperature corrosion behavior of stainless steels in automobile exhaust gas", *Trans. Iron Steel Inst. Jpn.*, 18 (7), p.387. (1978)

- [59] O. D. Sherby, "Factors affecting the high temperature strength of polycrystalline solids", *Acta Metall.*, **10**, p.135. (1962)
- [60] D. H. Herring, "Sigma-phase embrittlement", *Industrial Heating*, Feb. 29. (2012)
- [61] I. Zucato, M. C. Moreira, I. F. Machado, and S. M. Giampietri Lebrao, "Microstructural characterization and the effect of phase transformations on toughness of the UNS S31803 duplex stainless steel aged treated at 850°C", *Mater. Res.*, 5 (3), p.385-389. (2002)
- [62] J. -S. Lee, I. -S. Kim, and A. kimura, "Application of small punch test to evaluate sigma-phase embrittlement of pressure vessel cladding material", *J. of Nuclear Sci. and Tech.*, 40 (9), p.664-671. (2003)
- [63] A. M. Babakr, A. Al-Ahmari, K. Al-Jumayiah, and F. Habiby, "Sigma phase formation and embrittlement of cast iron-chromium-nickel (Fe-Cr-Ni) Alloys", *JMMCE*, 7 (2), p.127-145. (2008)
- [64] https://en.wikipedia.org/wiki/Intergranular_corrosion
- [65] "Corrosion Failure-Intergranular Corrosion", R&B Inc, Report No. RB-FA-C005.
- [66] <http://www.corrosionpedia.com/definition/638/hot-shortness>
- [67] <http://terms.naver.com/entry.nhn?docId=737567&cid=42325&categoryId=42325>

- [68] [http://en.wikipedia.org/wiki/Iron\(II\)_sulfide](http://en.wikipedia.org/wiki/Iron(II)_sulfide)
- [69] D. A. Melford, "The influence of residual and trace elements on hot shortness and high temperature embrittlement", *Phil. Trans. Soc. Lond. A*, **295**, p.89-103. (1980)
- [70] S. S. Mann and L. H. Van Vlack, "FeS-MnS phase relationship in the presence of excess iron", *Metallurgical Trans. B*, **7B**, p.469-475.
- [71] K. Shibata, S. -J. Seo, M. Kaga, H. Uchino, A. Sasanuma, K. Asakura, and C. Nagasaki, "Suppression of surface hot shortness due to Cu in recycled steels", *Mater. Trans.*, **43** (3), p.292-300. (2002)
- [72] Z. Liu, Y. Kobayashi, K. Nagai, J. Yang, and M. Kuwabara, "Morphology control of copper sulfide in strip casting of low carbon steel", *ISIJ Inter.*, **46** (5), p.744-753. (2006)
- [73] http://en.wikipedia.org/wiki/Electron_backscatter_diffraction
- [74] J. -H. Kim, D. -I Kim, J. -H. Shim, and K. -W. Yi, "Investigation into the high temperature oxidation of Cu-bearing austenitic stainless steel using simultaneous electron backscatter diffraction-energy dispersive spectroscopy analysis", *Corrosion Sci.*, **77**, p.397-402. (2013)
- [75] D. -I. Kim, J. -S. Kim, and S. -H. Choi, "A study on the annealing behavior of Cu-added bake-hardenable steel using an in situ EBSD technique", *Acta Mater.*, **68**, p.9-18. (2014)
- [76] http://en.wikipedia.org/wiki/Auger_electron_spectroscopy
- [77] Chuan C. Chang, "Auger electron spectroscopy", *Surface Sci.*, **25**,

p.53-79. (1971)

- [78] M. P. Seah, “Quantitative auger electron spectroscopy and electron ranges”, *Surface Sci.*, **32**, p.703-728. (1972)
- [79] <https://www.bruker.com/kr/products/x-ray-diffraction-and-elemental-analysis/csonh-analysis/g4-icarus-cs-hf/overview.html>
- [80] P. Hidnert and R. K. Kirby, “Thermal expansion and phase transformations of low-expanding cobalt-iron-chromium alloys”, *J. of Res. of the Nat. Bureau of Standards*, 55(1), p.29-37. (1955)

초 록

동 제련 공법 중 하나인 미쯔비시 공정 중 용련로(S로)는 동 정광을 약 68%의 동을 함유한 매트로 제련하는 공정이다. S로 내부는 1300°C 가 넘는 고온 분위기와 격렬한 반응이 일어나고 있다. 현재 현재 조업에서 발생하는 문제점 중 하나는 동 광석과 포화 산소를 투입하는 랜스의 짧은 수명과 불규칙한 파괴이다. 특히 2008년 증설 후 고가의 고크롬강 재질인 랜스의 교체 비용이 증가하고 있고, 불규칙하게 파괴된 랜스의 높이를 맞추기 위한 조업 중지 작업 때문에 상당한 공정 비용 손실이 발생되고 있다.

미쯔비시 공정에 대한 선행 연구가 부족한 상황에 가혹한 내부 환경 때문에 실험적인 접근도 어렵기 때문에 S로에 대한 공정을 모사할 수 있는 수치 모델 개발이 필요하다. 따라서 본 연구에서는 다상 유동, 열 전달, 복사, 입자 추적 등과 같은 S로의 복잡한 현상들을 모사할 수 있는 종합 모델을 개발하고, 모델을 사용해 S로 내부에서 일어나는 현상들을 이해하고 이론적, 학술적으로 의미 있는 데이터를 찾아, 다양한 수치 실험을 통해 S로 내부에서 일어나는 문제들을(랜스 파괴 등) 해결하고 개선책을 제시하고자 한다.

S로 내부의 유동 현상은 가스 및 입자 투입 조건에 따라 변

화한다. 가스와 입자가 동시에 투입될 때 멜트의 유속이 더 높고, 특히 랜스 하단의 유속이 높다. 강한 투입 속도로 인해 많은 매트와 슬래그가 비산되어 랜스 및 로 내에 안 좋은 영향을 주고 있다.

공정 중 가스만 주입될 때에는 랜스 팁의 온도가 빠르게 상승하고, 가스와 광석이 동시에 주입될 때에는 랜스 팁의 온도가 느리게 하강하였다. 계산을 통해 광석의 반응열 및 복사열 때문에 온도가 상승하고, 광석의 열 흡수 때문에 온도가 하강하는 것을 확인하였다. FFT 분석을 통해 비산되는 멜트의 볼륨 비와 랜스의 온도 변동 주기가 비슷하고 따라서 멜트의 비산이 랜스의 온도 변동을 유발한다는 것을 밝혀내었다. 랜스가 겪는 내부-외부, 상단-하단 및 온도 변동 현상들은 랜스에 열 응력 및 열 피로를 야기할 수 있으며, 응력 분석 결과 대부분의 랜스가 항복강도 이상의 응력을 받고 특히 온도 변화를 많이 겪는 랜스 하단이 취약함을 확인하였다.

사용 전 랜스와 파괴된 랜스의 미세조직을 분석한 결과, 랜스 외부 표면에서 Cr 이 감소되고 S, Si 및 O 로 이루어진 물질들이 grain boundary 내부에 침투해 있는 것을 확인하였다. 이로 인해 외부 표면이 취약해지고 공정 중 랜스가 받는 저주기 열 피로 및 비산되는 매트 및 슬래그 등의 외부 요인으로 인해 crack 이 생성되고 랜스 내부로 빠르게 전파되어 랜스의 빠른 파괴가 일어나는

메커니즘을 예상할 수 있었다.

랜스의 파괴를 줄이는 방법으로 랜스 팁의 높이를 상승시켜 랜스가 받는 열 피로를 줄이는 수치 실험을 진행하였다. 랜스 팁을 올리면 멜트의 혼합에 있어 불리해질 수 있는 문제가 있기 때문에 현업 조건의 랜스 팁의 높이와 유속을 멜트 혼합의 기준점으로 설정하고, 다양한 조건들을 수치 실험을 통해 비교 분석하였다. 그 결과 랜스 팁의 높이가 낮을수록, 랜스 팁의 유속이 높을수록 로 내 유동 현상은 불안정해지며, 랜스 팁을 올리더라도 유속을 올리면 동일한 멜트의 혼합을 유지하며 로 내 유동 현상은 안정화 될 수 있음을 확인하였다. 특히, 랜스 팁을 올렸을 때 랜스의 온도가 기존보다 낮아져 1000°C 이상의 고온에서 랜스가 받는 문제점 및 열 피로 현상들을 줄일 수 있음을 확인하였고, 결론적으로 랜스의 파괴를 줄이고 안전한 로 내 조건을 구현할 수 있음을 확인하였다.

주요 단어: Mitsubishi process, smelting furnace, copper refining,
수치해석, 온도 변동

학 번: 2012-30159